MULTIFERROIC AND CORE-SHELL NANOSTRUCTURES - ADVANCES IN PREPARATIONS AND NOVEL PROPERTIES

by

I-WEI CHU

A dissertation submitted to the Graduate Faculty in Chemistry in partial fulfillment of the requirements for the degree of Doctor of Philosophy, The City University of New York

2010

This manuscript has been read and accepted for the
Graduate Faculty in Chemistry in satisfaction of the
dissertation requirement for the degree of Doctor of Philosophy.

Dr. Nan-Loh Yang

Date

Chair of Examining Committee

Dr. Mahesh K. Lakshman

Date

Executive Officer

Dr. Ronald G. Pirich

Dr. Steven A. Schwarz

Supervisory Committee

THE CITY UNIVERSITY OF NEW YORK

Abstract

MULTIFERROIC AND CORE-SHELL NANOSTRUCTURES - ADVANCES IN PREPARATIONS AND NOVEL PROPERTIES

by

I-WEI CHU

Adviser: Professor Nan-Loh Yang

This dissertation reports the research findings in two nanoscience areas: (i) facile methods for the preparation of multiferroic bismuth ferrites nanoparticles and the observation of room temperature magnetoelectric coupling and optically induced magnetic and electric orderings in $BiFeO_3$ (BFO) thin film; (ii) preparation and characterization of core-shell nanomaterials based on conducting polymer as components for shell and core. Controlled cargo release from the core as well as from the shell surface was examined for nanospheres with conjugate polymer shell. An unusual enhanced electric polarization was observed for nanospheres with high-*k* strontium titanate (STO) nanocrystals embedded in conductive polyaniline (PANI) matrix.

Multiferroics represent a class of new materials having potential applications for design and preparation of multifunctional material due to the coupling of their coexisting electric and magnetic orderings. Previously, the syntheses of thin film multiferroic materials involve multi-steps in various high temperatures or specific demanding environment. We discovered that nanocrystal thin film and powder of multiferroic BFO could be prepared using new facile procedures: spin-casting and autoclave methods. The room temperature magnetoelectric coupling in nanocrystal BFO was established using scanning probe microscopy, including magnetic force microscopy (MFM) and Kelvin probe force microscopy (KPFM). Magnetic and electrical orderings induced by irradiation 300 to 560 nm were observed. Thus, the “magnetic-electric-optic” coupling at room temperature was observed for the *first* time in BFO nanocrystal thin film.

Core-shell nanospheres of conducting polymer poly(3, 4-ethylenedioxythiophene), PEDOT, with soft template (1-butyl-3-methyimidazolium hexafluorophosphate, bmimPF$_6$) were prepared using interfacial polymerization on the shell surface of the micelle stabilized by surfactant (Triton X-100). The diameter of nanospheres was controlled by bmimPF$_6$-to-surfacnt ratio. The release of cargo from the core and shell of the spheres was trigged by pH control and observed by photometric measurement. Aspect ratio and crystallinity of PEDOT shell increases in high pH value (above 10). In addition, the interaction of electronic polarization with atomic polarization was studied for core-shell nanosphere of PANI matrix with STO nanoparticles embedded. This nanosystem represents the first encapsulated nanospheres with extensive interfacial interaction within the core due to atomic polarizable isolated nano-domains embedded in an electronic polarizable continuous matrix.

Acknowledgments

It is my pleasure to thank all people who made this thesis possible. First, I would like to thank my advisor, Dr. Nan-Loh Yang, for support and guidance in my graduate studies. With his encouragement and patience in helping me grow as a scientist. He has made available his support in a number of ways. He provided me with many opportunities to participate in conferences and work together with outstanding scientists. From those collaborations, I improve communication and interpersonal skills. I also would like to thank my co-advisor, Dr. Ronald G. Pirich, and committee member, Dr. Steven A. Schwarz for their guidance. I am grateful for the sustained support from: New York State Office of Science Technology Academic Research, through the Center for Engineered Polymeric Materials, CePM; and NSF through the MRSEC for polymers at Engineered Interfaces.

I would like to thank Dr. William L'Amoreaux and Dr. Yalin Wang, Advanced Imaging Facility at College of Staten Island, CUNY, for technical guidance in AFM and TEM experiments, Dr. Xueyan Zhang, Dr. Jeong Seop Shim and the Material Characterization Laboratories at New Jersey Institute of Technology for the use of the electron microscope and X-ray diffraction facilities, and Dr. Huixin He at Chemistry department of Rutgers-Newark, for the use of UV-Vis-IR spectrometry.

Special thanks to Dr. Kai Su for his helpful discussions. He introduced me to the exciting fields of multiferroic and conducting polymer and advised me with the riches of his analytical knowledge. His devotion to science always inspires me during my research work. I will always remember his creative guidance and constructive criticism. I also appreciate all Dr. Yang's lab group members, current and past for working together in everyday lab activities.

I wish to thank my parents for supporting me throughout my life and encouraging me to pursue my dreams and aspirations. I would like to thank my husband, Wen-Chun, for his love and support especially when I felt overwhelmed and frustrated in my studies. I also like to thank my daughter, Katie. She enriches my life and makes me happy every day.

Table of Contents

List of Tables

List of Figures

List of Schemes

Chapter 1 Introduction

The development of nanoscience in the past decades has led to a revolution in our understanding of fundamentals as well as potential applications based on materials in nanoscale.[1] The widespread interest in nanomaterials mainly originates from their unusual properties in areas including optical, electrical, mechanical and chemical performance. Currently, these materials include many formations such as nanospheres, nanotube/fiber, nanocomposite, and core-shell nanostructure; their classifications include metal, inorganic, organic/inorganic hybrid, semiconductor, biomaterial, and polymer. Two types of nanomaterials, inorganic and polymer, were investigated in this dissertation work. Inorganic multiferroic nanomaterials show both magnetic and electric ordering in same phase, serving as fundamental elements for novel devices. Polymers provide a various advantages including their tunable functionalities. Among a wide range of polymers, conducting polymers can provide electronic conductive building blocks adaptable to a wide spectrum of applications. Multiferroics[2-5] have properties of both electric and magnetic orderings. The understanding of fundamental physics of electric polarization by electric field has led to advancement in applications such as transducers, actuator, capacitors, and high density data storage. In recent years, nanomagnets have contributed to the dramatic increase in data storage density. A limited number of multiferroics systems can show magnetoelectric coupling, the control of magnetic ordering by electric field and vice verse. This coupling of the two fundamental fields could lead to new generations of memory devices involving processes such as electric encodings for magnetic reading, i.e. multiple state memory elements with four possible states from combination of magnetic and electric polarizations, ***M*** and ***P*** (Figure 1.1).[6] Recent articles reported that decrease in size to nanoscale may give rise to higher magnetization.[7-9] Among the multiferroics, bismuth ferrites, $BiFeO_3$ is the only materials shown to possess both magnetic and electric orderings. In Chapter 2, we report our discovery: the ***room temperature*** magnetoelectric coupling in BFO nanocrystal thin film. New facile approaches for the preparation of bismuth ferrite are also described.

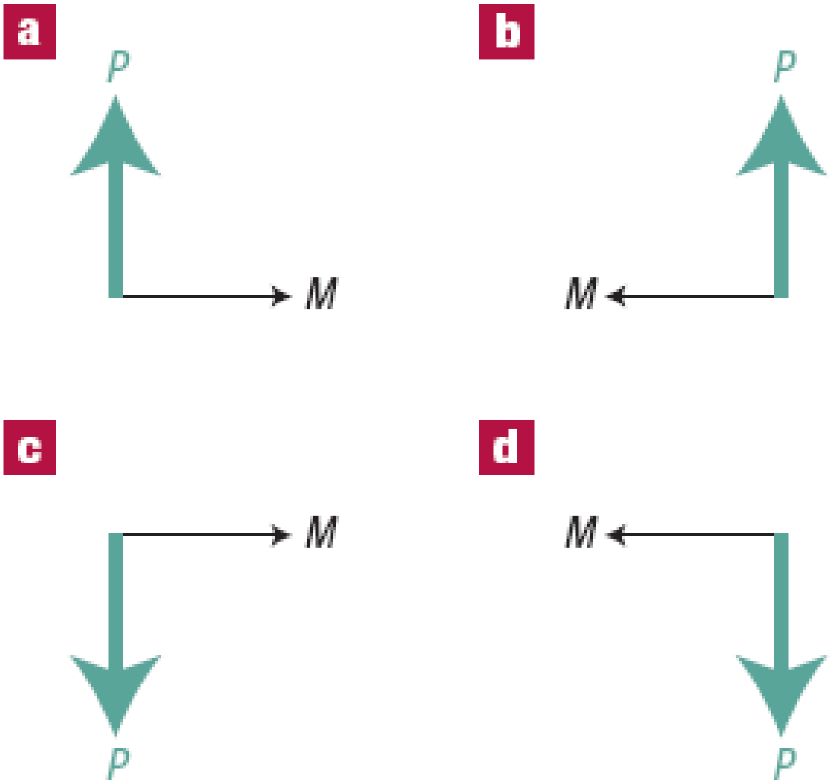

Figure 1.1 **The four possible states formed by electric polarization *P* and magnetization *M* of multiferroic order.** (a) (+*P*, +*M*), (b) (+*P*, –*M*), (c) (–*P*, +*M*), and (d) (–*P*, –*M*). (From Ref. 6)

In addition to inorganic nanocrystsals, we investigated nanostructures based on conducting polymer. The electronic conductivity in polyacetylene was first discovered in 1977.[10] Since 2000 Nobel Prize in Chemistry awarded for discovery of organic conducting polymers, momentous progress has been made over 25 years in this field.[11] Recently, nanostructures[12] (i.e. nano-spheres, -rods, -tubes, -wires, and -fibers) of conducting polymers have gained growing interest, because the combination of characteristic of conducting polymer with nanoscale size creates many potentially breakthrough in applications, including sensors, data storage, supercapacitor, electrochromic device, and field mission display.[13] Core-shell composites represent a significant family of nanostructures. The characteristics of the material of the shell generally diverge from that of the core. The shell can enhance thermal and chemical stability of nanoparticles, improve solubility, render them less cytotoxic, and allow attachment of conjugates. The conducting polymer shell can be biological compatible and serve to control the features of the nanosphere. Two types of core-shell nanospheres from conducting polymers are reported in Chapter 3. First, a nanosphere with conducting polymer (poly(3, 4-ethylenedioxythiophene) as the shell and a room-temperature ionic liquid (RTIL, bmimPF$_6$) as the core was prepared. This core-shell sphere was demonstrated to serve as an efficient vehicle for controlled release. The RTIL core is nonvolatile, thermally stable and with tunable solvation properties and PEDOT shell controls the volume change leading to cargo release either from the core or from the shell surface. The second type of core-shell nanospheres consists of doped polyaniline (PANI) insulating shell with core of high-*k* material strontium titanate embedded in conducting PANI matrix. This novel structure combines atomic and electronic polarizations in one element of nanometer scale and exhibits synergistic electronic properties.

Chapter 2 Advancement in Methods for the Preparation of Multiferroic, Bismuth Ferrites, Nanoparticles and the Observation of $BiFeO_3$ Room Temperature Magnetoelectric Coupling

2.1 Introduction

Multiferroic[1-3] materials have recently gained considerable importance both technologically and scientifically[4-7] because of the existence of two or more of the properties of ferroelectric, ferromagnetic (or antiferromagnetic) and ferroelastic orderings in the same sample phase, with possible couplings of their order parameters (spin and charge) (in Figure 2.1).[4-7] Multiferroics are promising materials for design and synthesis of multifunctional material due to the potential applications of magnetic and electric switching. Incorporating the observed optical responses[8-12] multiferroics can lead to device applications exploiting all three of electric, magnetic, and optic responses.[13-16] As a consequence, multiferroics has been the subject of recent extensive investigation.[17-19] However, there are indeed few existing multiferroic materials (Figure 2.2).[4]

Optical properties of multiferroics have been known for many years.[20-22] Optical magnetoelectric effect[21, 23-28] is among the most important properties. It is defined as the phenomenon of the change of refractive index or absorption coefficient upon the reversal of light propagation direction relative to magnetic field, electric field applied or pre-exiting.[10] Few reports on optical properties for multiferroic have been published, although they are expected to manifest themselves due to the inherent magnetic and electric nature of light.[9, 11, 20, 24, 26, 29-33] However, the interaction among optic and magnetic and electric orderings is still not well-developed. A recent article showed the possible novel optical application of $BiFeO_3$ (BFO) films.[29] This article showed that the visible-light photovoltaic effect on BFO diode led to the understanding of charge conduction mechanisms in leaky ferroelectrics and the advance in the design of switchable devices combining all three functionalities. Among the many multiferroics, BFO has attracted considerable attention. It is known to be the only material that displays multiferroism at room temperature (Table 2.1)[34-37] with its ferroelectric Curie temperature T_c of 1103 K and antiferromagnetic Néel temperature T_N of 643 K.

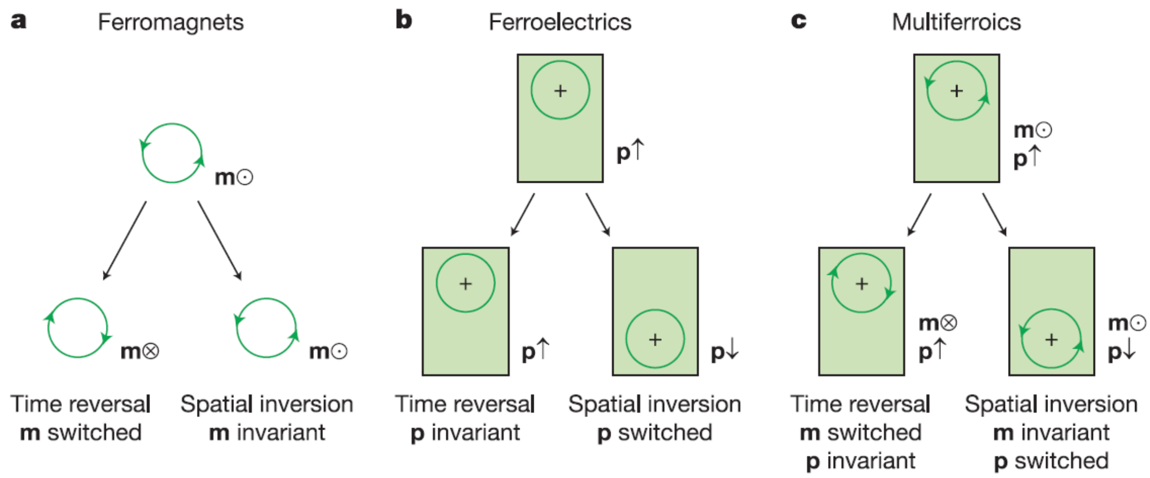

Figure 2.1 **Time-reversal and spatial-inversion symmetry in ferroics.** (a) Ferromagnets. The local magnetic moment **m** may be represented classically by a charge that dynamically traces an orbit, as indicated by the arrowheads. A spatial inversion produces no change, but time reversal switches the orbit and thus **m**. (b) Ferroelectrics. The local dipole moment **p** may be represented by a positive point charge that lies asymmetrically within a crystallographic unit cell that has no net charge. There is no net time dependence, but spatial inversion reverses **P**. (c) Multiferroics that are both ferromagnetic and ferroelectric possess either symmetry. (From Ref. 4)

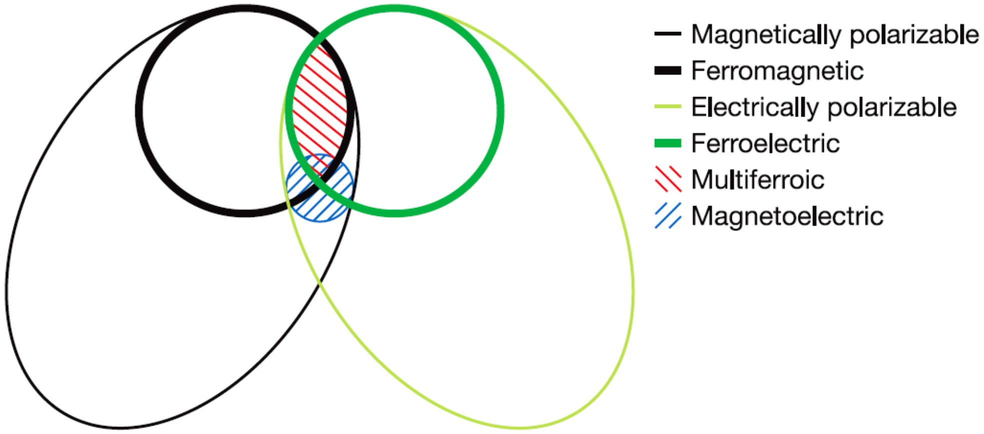

Figure 2.2 **The relationship between multiferroic and magnetoelectric materials.** The intersection (red hatching) represents materials that are multiferroic. Magnetoelectric coupling (blue hatching) is an independent phenomenon that can, but need not, arise in any of the materials that are both magnetically and electrically polarizable. (From Ref. 4)

Table 2.1 List of The Neel (T_N) temperature and Curie temperature (T_C) for well-known multiferroics. $BiFeO_3$ is only material that displays multiferroism at room temperature. [34-38]

Multiferroics	T_N	T_C
$BiFeO_3$[34]	**~643 K**	**~1103 K**
$Bi_2Fe_4O_9$[38]	**~260 K**	**P-E loop ~ 250 K**
$RMnO_3$[34] (R=Ho-Lu, Y)	~100 K	~1000 K
$DyMnO_3$[35]	~40 K	17.5 K
$Ni_3V_2O_8$[36]	~9.8 K	4.28
$RMnO_3$[37] (R=Tb, La)	~41 K	~28 K

The structure of BFO is characterized by distorted perovskite structure connected along their body diagonal along one of the pseudocubic (111) axes (Figure 2.3a). The ferroelectric state is a large displacement of the Bi ions relative to the FeO_6 octahedral. The ferroelectric polarization in BFO, therefore, can have eight possible directions corresponding to positive and negative orientation along the four cube diagonals (111), changed by ferroelectric 180º (Figure 2.3b) and ferroelastic switchings 71º and 109º (Figure 2.3c, d). The Fe magnetic moments are aligned ferromagnetically within pseudocubic (111) planes and antiferromagnetically between adjacent (111) planes. The preferred orientation of the antiferromagnetically aligned spins is in the (111) plane perpendicular to the ferroelectric polarization direction. The antiferromagnetism is coupled to the ferroelectric polarization.[39, 40] In fact BFO shows, at room temperature, a weak ferromagnetism due to the residual moment from canted spin structure.[41, 42] Thus, BFO is currently considered to be the one of the most promising candidate for new breakthrough in device applications based on the coupling between ferroelectric and ferromagnetic orders at ambient conditions.

Most of multiferroics have been prepared in bulk form (such as crystal, ceramic or powder) and thin film. However, for BFO bulk samples, single perovskite phase is hard to obtain and their leakage problems lead to low resistivity, presumably due to defect and nonstoichiometry related issues, leading to difficulty in the observation of intrinsic saturated ferroelectric hysteresis loop.[43-46] Recently, high-quality thin film growth techniques have opened the door to the possibility of devices based on magnetoelectric coupling.[47] Thin film growth has been achieved through processes involving multi-steps at various high temperatures, specific environment and sophisticated instrument. These previously established methods[3] include: pulsed laser deposition (PLD),[48] liquid-phase epitaxy,[39, 49] sol-gel methodology,[45, 50] and chemical solution deposition.[51, 52] Our methodology involved much less demanding procedure (see below).

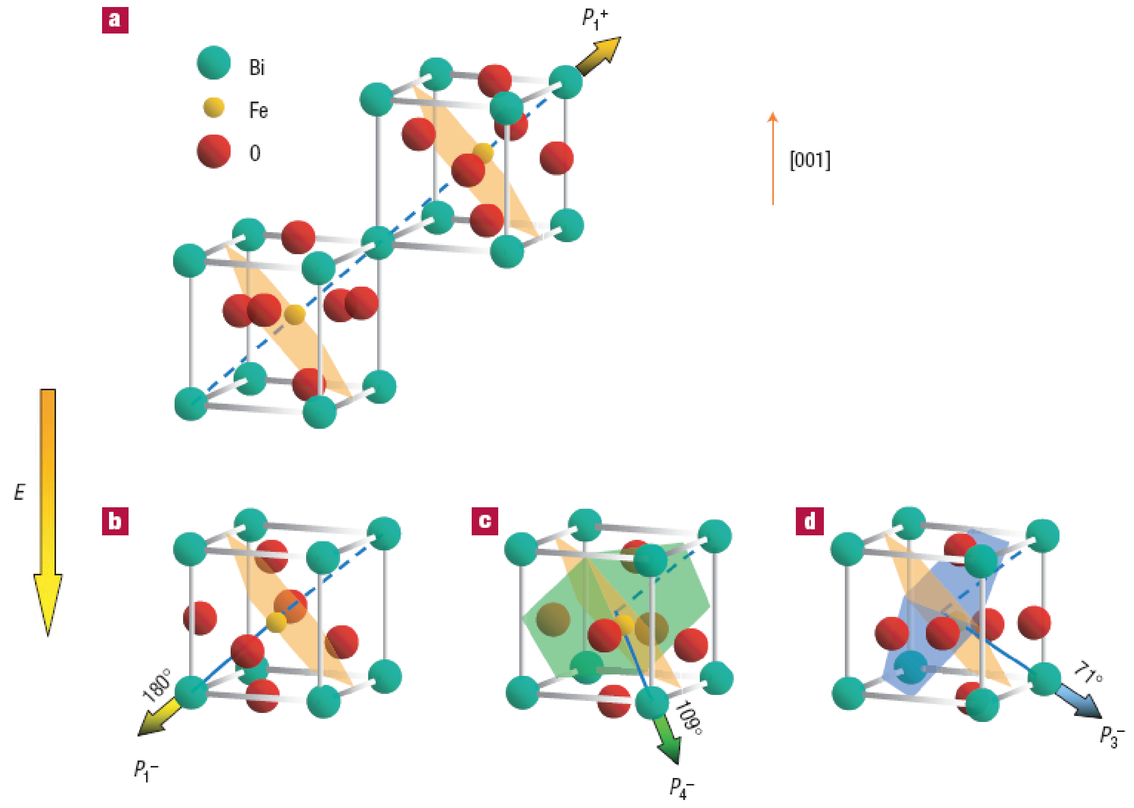

Figure 2.3 Schematic diagram of (001)-oriented $BiFeO_3$ crystal structure and the ferroelectric polarization (bold arrows) and antiferromagnetic plane (shaded planes). (a) Polarization with an up out-of-plane component before electrical poling. (b) 180° polarization switching mechanism with the out-of-plane component switched down by an external electrical field. The antiferromagnetic plane does not change with the 180◦ ferroelectric polarization switching. 109° (**c**) and 71° (**d**) polarization switching mechanisms, with the out-of-plane component switched down by an external electrical field. The antiferromagnetic plane changes from the orange plane to the green and blue planes on 109°and 71° polarization switching respectively. (From Ref. 40)

Furthermore, the size of material plays an important role in physical property control.[46, 50] The Néel temperature T_N of BFO has been shown to decrease with decreasing particle size.[46, 53] The magnetic properties of BFO have also been reported to enhance in small particle due to surface-induced magnetization.[46, 50, 54] The synthetic technique and process are critical to nanostructures. In addition, some other bismuth ferrites are also important functional material, such as $Bi_2Fe_4O_9$, a good catalyst for ammonia oxidation to NO. A recent article indicated that ferroelectric property could be observed at nanosize $Bi_2Fe_4O_9$ near room temperature.[38]

In this thesis work, three approaches for the synthesis of bismuth ferrite nanometer-sized single particles were investigated. Well-define BFO nanoparticles thin film was obtained by spin casting followed by heating at 600 ºC. Autoclave method yielded nanocrystal powders of different ferrites at two temperatures only 20 ºC apart: BFO (185 ºC) and $Bi_2Fe_4O_9$ (165 ºC). Bismuth ferrite non-crystalline powder was obtained by microemulsion method. Structure and elemental composition (Bi/Fe) of nanocrystals were performed by X-ray diffraction (XRD), and X-ray electron dispersive spectroscopy (EDS). The magnetic force microscope (MFM) and Kelvin probe force microscopy (KPFM) were applied to characterize magnetic and electric orderings. The morphology studies were performed using scanning electron microscopy (SEM) for crystal BFO thin film and transmission electron microscopy (TEM) for powders of BFO and $Bi_2Fe_4O_9$. Not only electric and magnetic orderings of thin film BFO but also their coupling was observed at room temperature using MFM and KPFM. In addition, the two AFM methods established our discovery of optical induced magnetic and electric orderings in BFO.

2.2 Experimentals

2.2.1 Spin-casting synthesis

All reagents for synthesis were purchased from Sigma-Aldrich and used without further purification. Bismuth(III) nitrate pentahydrate (11.26 mmol) and iron(III) nitrate nonahydrate (11.26 mmol) were dissolved in ethylene glycol (1.614 mol) at room temperature to form the precursor solution and a drop of the solution (0.125 M in Bi and Fe) was spin casted on clean silicon wafers of similar area size at spin rates of 300 rpm, 500 rpm, 1000 rpm, 2000 rpm, and 3000 rpm. The wafer was washed three times with pure methanol before use. The thin film was then allowed to stand in a clean environment for an hour and then heated at 600 °C in a tube furnace for 1 hour, followed by two cycles of washing with HCl (0.1 M) and distilled water to remove impurity. The thin films made at 2000 rpm were of the best quality and was heated in various temperatures from 600 °C to 800 °C by a step of 50 °C for XRD observation. The precursor solution was also casted on Au surface deposited on silicon wafer as well as quartz plate with Au contacts (0.5×0.5 square), followed by sintering at 600 °C for the observation of electric, magnetic and optical effects.

2.2.2 Autoclave synthesis

Sodium hydroxide (1.088 g) and hydrogen peroxide (0.1 g) was dissolved in 6.16 g water (pH>13) as aqueous solution. The aqueous solution was then added in 60 g precursor solution (as made in spin-casting synthesis) with 2 g surfactant (triton x-100, Tx-100). The mixture solution was transferred to an autoclave for reaction at either 165 or 185 °C for 24 hours. After reaction, the product was purified using three cycles of centrifugation and re-suspension followed by drying in an oven at 70 °C.

2.2.3 Microemulsion synthesis

Sodium hydroxide (0.45 g) and hydrogen peroxide (0.1 g) was dissolved in 5 g water (pH>13) as aqueous phase, and then the aqueous solution was added in 10 g oil solution (5g cyclohexane and 5 g n-butanol) with 5g Tx-100 as “emulsion I”. “Emulsion II” was made by adding 20 g precursor solution in 100 g oil solution (50 g cyclohexane and 50 g n-butanol) with 50g Tx-100. Then, “emulsion I” reacting with “emulsion II” at 80 °C for 3 hours gave bismuth ferrite. The product was purified using centrifuge re-suspended three times followed by drying in oven at 70 °C.

2.2.4 Characterizations by TEM, SEM/EDS, X-ray diffraction, dielectric dispersion, AFM, MFM, KPFM, optic-MFM and -KPFM

Samples for scanning electron microscopy and X-ray energy dispersive spectroscopy (SEM and EDS, LEO 982) were prepared by spin casting on clean silicon wafers using a spinner (photo-resist spinner, EC101DT-R485, Headway Research Inc.). Silicon wafers as substrate for microscopy observation were washed several times with pure methanol before use. The precursor film was allowed to settle for a few hours before heating to form BFO film. For transmission electron microscopy (TEM) samples, a drop of the BFO suspension was dried on carbon-coated copper grids at room temperature. A JEOL 1200 EX microscopy at an acceleration voltage of 80 kV was employed. X-ray Diffraction (XRD) studies were conducted on a Philips PW3040 X-Ray diffractometer with CuKa radiation (k = 1.5406 Å) operated at 40 kV and 60 mA in the 2θ range of 20–70° with a step size of 0.03°. The dielectric constant was obtained on a dielectric spectrometer (Novocontrol BDS 80 high-resolution broadband) at frequencies from 1μHz to 10 MHz, bias voltage of 1 V DC at room temperature. Sample cell size is 2.06 mm height with 18.05 mm diameter. Atomic force microscope (AFM), magnetic force microscope (MFM) and Kelvin probe force microscopy (KPFM) studies were conducted on a MFP-3D microscopy (Asylum Research). For mapping MFM images, noncontact-mode silicon cantilevers MFMR-10 from NanoSensors/Asylum Research were used. Because the orientation of magnetization of the Co coated tip of cantilever is random, before starting the MFM measurement we conducted re-magnetization using a permanent magnet brought close to the tip for 10 seconds at a few mm distance. For studying KPFM, tapping-mode silicon cantilevers fitted with a Pt coated tip (AC240TM-10 from Olympus) having a spring constant ~2 N/m and resonance frequency ~70 kHz was used. DC bias was applied on the gold surface to induce polarization during surface potential mapping. For optic-MFM and -KPFM, a beam from a light source (BlueWave 200 UV, DYMAX) was focused on the BFO film from the under of the sample stage, delivering irradiation with a range of wavelength of 300 to 560 nm (Figure 2.4, cyan spectrum).

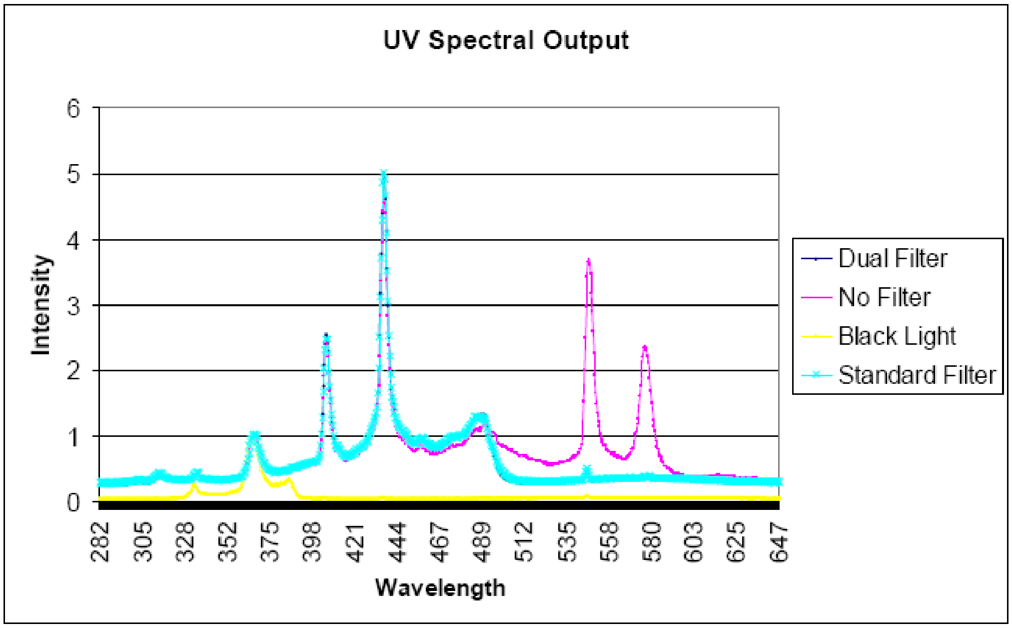

Figure 2.4 **Output spectrum of light source.** (From operations manual, BlueWave 200 UV, DYMAX).

In our AFM studies, tapping mode was employed. There are three primary mode of operation for an AFM, contact, non-contact, and tapping modes. In contact mode, or repulsive mode, the tip drags across the surface of sample and the image is obtained from the deflection of cantilever. However, the attractive forces is quite strong between tip and surface of the sample, causing the tip and sample damage. In non-contact mode, the tip is not in contact of the surface of sample. The cantilever is oscillated at resonance frequency, or harmonics due to van der Waals Force. Because the force between tip and sample in this mode is very weak, the measurement is more difficult than in the contact mode. In addition, the cantilever for non-contact mode must be stiffer because soft cantilever could be pulled into contact with the surface of sample. Both factors, small force and stiff cantilever, make the non-contact AFM signal weak. Thus, tapping mode AFM was developed decades ago to overcome the major problems from non-contact mode.[55] Tapping mode keeps the probe tip close enough to sample for short-range forces (van der Waals force) to render the signal detectable. Therefore, the tapping mode AFM was selected in this work to observe morphology of nanomaterials.

Magnetic and electric orderings were observed using MFM and KPFM. MFM can be used to establish the magnetic field gradient distribution over the surface and KPFM, the electric surface potential.[56] These two technique have been developed to reach subnano-scale resolution[57] for long range interaction involving magnetic forces[58] and electric force.[59, 60] The MFM and KPFM were performed with dynamic mode. In this mode, the first trace is a standard AFM trace that maps the topography of sample by gently tapping the tip along the surface, and the second scan retraces the topographic feature at constant height above the surface where a long range force is measured. By using this technique, the image mapping the long range force could be generated in conjunction with topography.

The MFM was used to image the magnetic orderings of the multiferroic materials with high resolution and sensitivity. For the observation of the nanometer scale magnetic property of the bismuth ferrite, the MFM measurements with a magnetic tip were performed using the dynamic mode to give a phase image. The sample was scanned and the changes in the magnetic interaction of the tip with the sample affect the resonance frequency shifts of the cantilever, leading to a contrast in the phase detection. In this experiment, a repulsive interaction between tip and sample is represented by bright contrast and an attractive interaction by dark contrast in the resulting image.

Kelvin probe force microscopy (KPFM)[45, 61-63] has been used to map electric polarization of nanosystems. In this dissertation, KPFM was employed as a tool to demonstrate the polarization in multiferroics and core-shell conducting polymer nanospheres. KPFM is a scanning probe technique, capable of mapping the local surface potential with spatial resolution in nanometer range. An AC bias applied to the tip creates a potential difference between the tip and the sample, leading to an electric force on the cantilever. The cantilever begins to vibrate if there is a potential difference between the AC voltage on the cantilever and the DC field on the surface (surface potential, SP, or work function). The system then adjusts the AC feedback voltage to minimize tip vibration, and the potential at the tip represents the local surface potential of the sample. The SP image is collected as the AC voltage applied to the scanning tip is recorded.

2.3 Discussions and Results

2.3.1 Spin-casting synthesis

2.3.1.a Crystallographic structure and Morphology studies

$Bi(NO_3)_3 \cdot 5H_2O$ and $Fe(NO_3)_3 \cdot 9H_2O$ in a 1:1 molar ratio dissolved in ethylene glycol serves as the precursor solution. The thin film of nanometer-sized $BiFeO_3$ (BFO) was obtained by spin-casting (2000 rpm) of precursor solution followed by heating at 600 °C to 800 °C by a step of 50 °C to ascertain the influence of temperature. XRD diffraction patterns of BFO thin film from heating at 600 °C and washed by HCl (Figure 2.5a) shows a crystal structure of rhombohedrally distorted perovskite (JCPDS No. 86-1518). Secondary phases bismuth ferrites were observed (Figure 2.5b) for the BFO thin film from 600 °C without purification. Further increase in the heat treatment temperature above 650 °C leads to the appearance of nonperovskite phases as $Bi_2Fe_4O_9$ (Figure 2.5c-f), an iron rich phase. This phase is especially prominent in the films heated at high temperature, suggesting loss of bismuth from the samples.[51] The XRD results suggest that pure crystal BFO formation is favored when thin film is heated at 600 °C, and show 0.1 M HCl as an efficient agent to remove the secondary phases. Elemental analysis using X-ray Energy Dispersive spectroscopy (Figure 2.6 and Table 2.2) shows an equal elemental ratio of Bi-to-Fe, supporting the XRD result. Furthermore, morphology, physical properties, and room temperature magnetoeletric coupling in this multiferroic thin film were demonstrated through SEM, AFM, MFM, and KPFM investigation.

The morphologies of the BFO thin films with different spinning rates were monitored using SEM (Figure 2.7 and 2.8). The SEM images results show that the morphology of thin film samples strongly depends on the spinning speed. The image of

BFO film from 300 rpm shows bubbles and rough surface (Figure 2.7a). This is due to slow solvent evaporation of low spinning rate. For the thin film formed from 500 rpm, the image (Figure 2.7b) shows surface cracking. Bubbles evaporate from the thin film and remain visible on the surface of 1000 rpm thin film (Figure 2.7c). Particles with 200 nm average diameter, and uniform and smooth thin film (2000 rpm) were obtained (Figure 2.8). When the spinning rate is increased to 3000 rpm, the surface becomes rougher as seen in SEM (Figure 2.7d). We, also observed precursor solution spun out of silicon wafer during spin casting in 3000 rpm. Thus, SEM images establish a spinning rate of 2000 rpm (Figure 2.8) as the optimum condition. According to SEM results, the sample of BFO multiferroic thin film from 2000 rpm was used as typical sample for characterization of magnetic, electric, and coupling induced by electric, magnetic field and irradiation

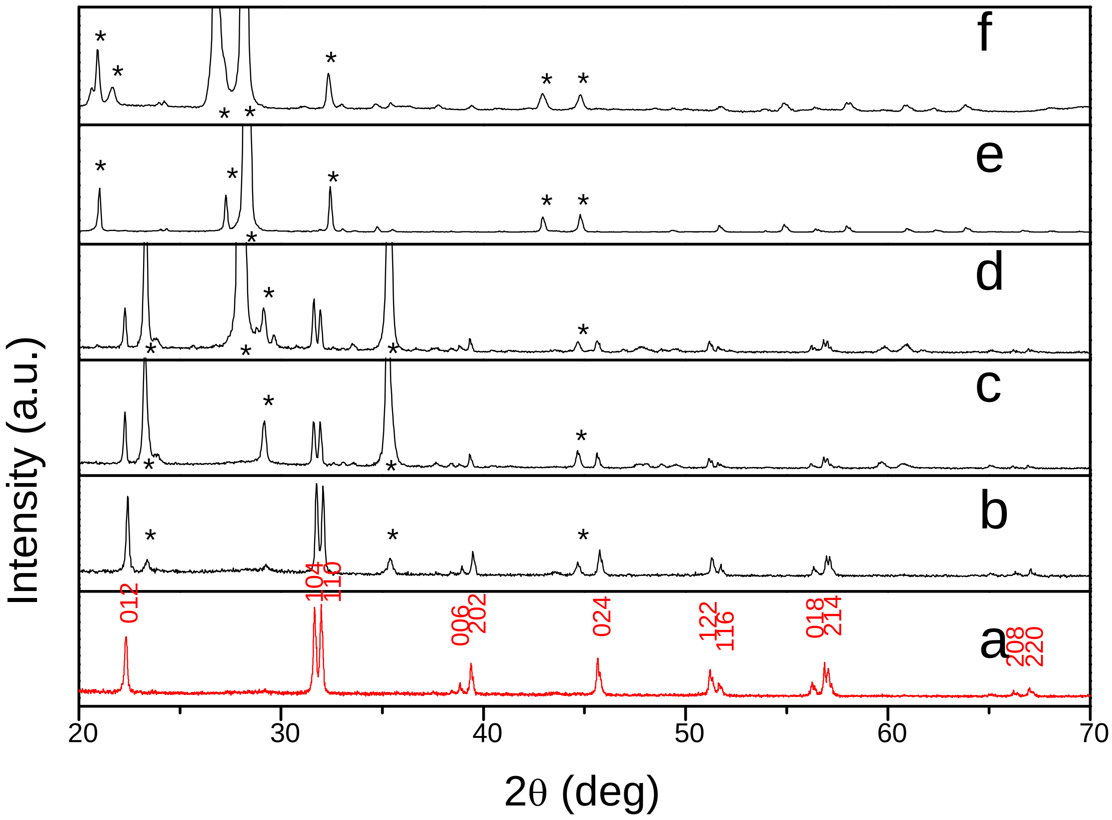

Figure 2.5 **Effect of heating temperature on crystals.** X-ray diffraction patterns of $BiFeO_3$ nanocrystal thin film prepared by spin-casting (2000rpm) of a precursor solution ($Bi(NO_3)_3 \cdot 5H_2O/Fe(NO_3)_3 \cdot 9H_2O/2(C_2H_2(OH)_2)$) followed by heating at different temperatures. (a) Heating at 600 °C washing by HCl (0.1M); (b) heating at 600 °C; (c) heating at 650 °C; (d) heating at 700 °C; (e) heating at 750 °C; (f) heating at 800 °C. (*-bismuth ferrites other than BFO)

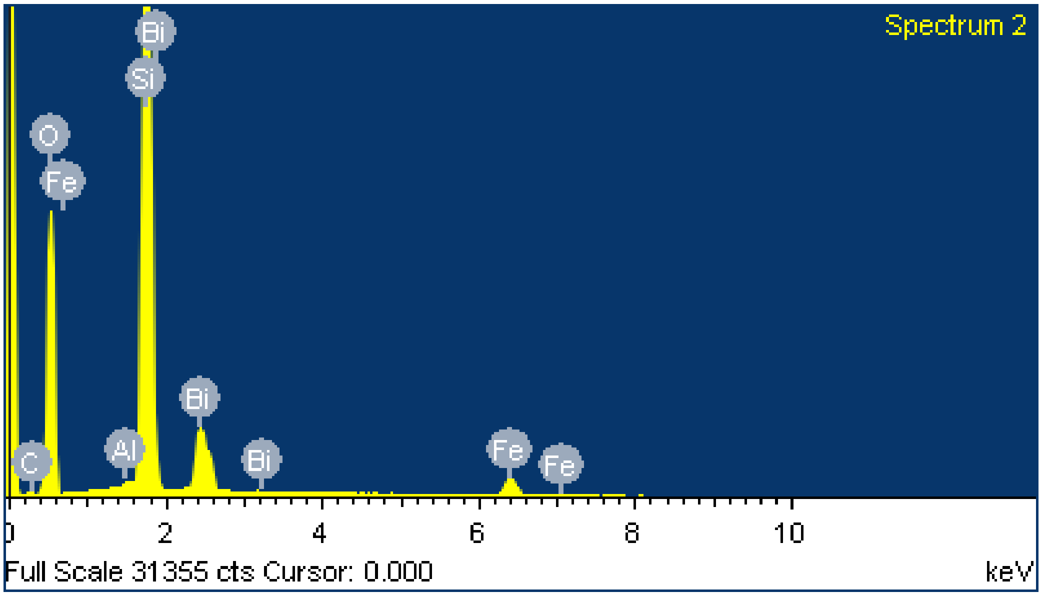

Figure 2.6 **X-ray Energy Dispersive spectroscopy (EDS) spectrum for BiFeO3 thin film made by spin-casting (2000 rpm) heating at 600 °C and washing by HCl.** The quantitative result shows a Bi/Fe ratio of 1, supporting the theoretical atomic ratio of 1.

Table 2.2 EDS quantitative results show a Bi/Fe ratio of 1 of spin-casting thin film (2000 rpm) in agreement wiht theoretical atomic ratio.

Element	Weight%	Atomic%
C	1.70	3.19
O	46.72	65.64
Al	0.07	0.06
Si	35.48	28.40
Fe	3.37	1.36
Bi	12.66	1.36
Totals	100.00	

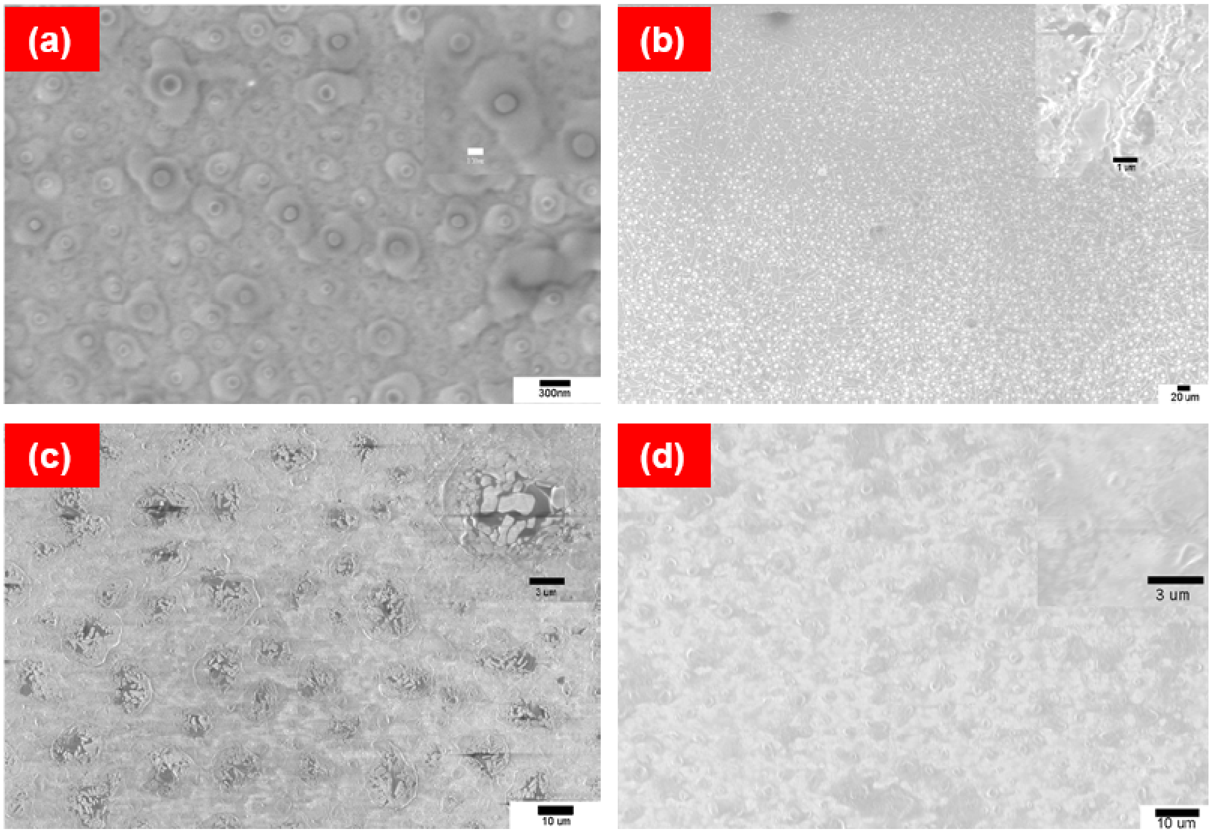

***Figure 2.7* SEM images of BFO thin film of nanocrystal in different spin-casting rate.** (a) 300 rpm; (b) 500 rpm; (c) 1000 rpm; (d) 3000 rpm.

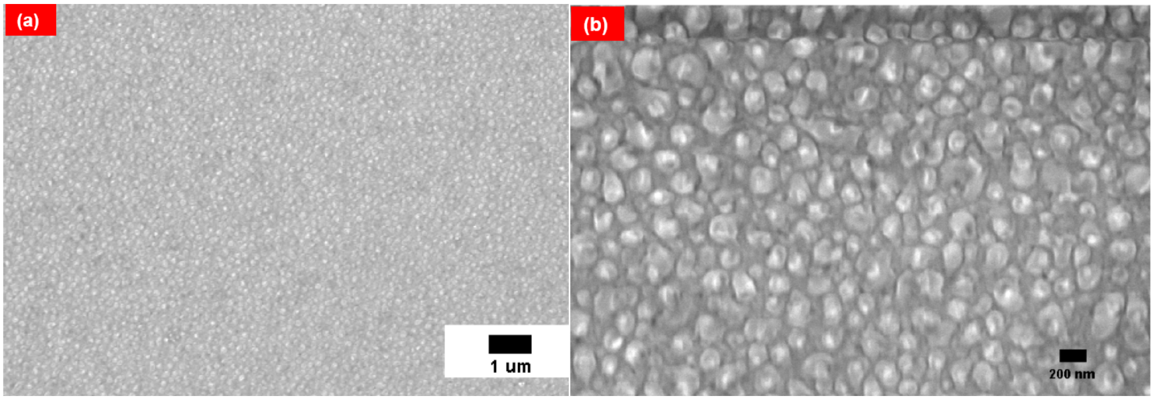

***Figure 2.8* SEM image of BFO thin film of nanocrystal**. (a) with scale bar 1 μm. (b) magnified image of (a) with scale bar 200 nm. The images show the particles average diameter of 200 nm.

2.3.1.b Magnetic ordering induced by magnetic field

The morphology of the BFO thin film from 2000 rpm was also established using AFM (Figure 2.9a). Both SEM (Figure 2.8) and AFM (Figure 2.9a) results show film with dense uniform nanoparticles (average 200 nm diameter and 45 nm height). For magnetic properties, MFM was used to image the magnetic orderings of the BFO thin film. The MFM image of BFO film (Figure 2.9b) is depicted by a bright and dark contrast over the surface at a constant tip height of 82 nm (ΔZ=82 nm). The MFM tip (300 Oe) was magnetized to the Z direction (perpendicular to the plane of the sample) prior to the measurement. The phase image (Fig. 2.9b), clearly indicates magnetic ordering with significant number of magnetic domains showing both magnetic polarities on the plane, i.e. white and dark regions (see insert). The featureless electrostatic force microscopy (EFM) image (Figure 2.10) from the BFO thin film was obtained with a metallic tip replacing the magnetic tip operating with a delta height of 50 nm. Tip for MFM without initial magnetization also resulted in featureless MFM image. These images indicate that electrostatic modulation and van der Waals force did not play a significant role in the MFM measurement.

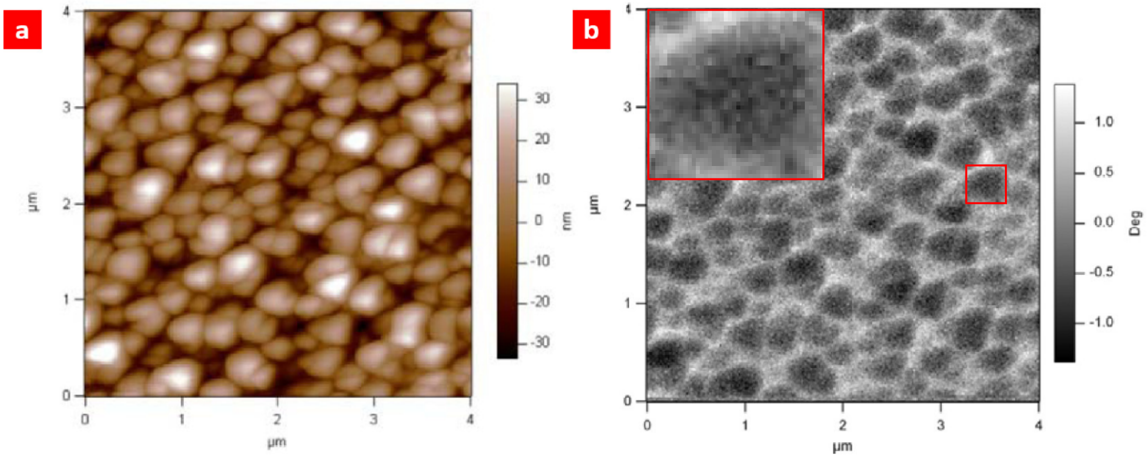

Figure 2.9 **AFM (a) MFM (b) image of BFO thin film as prepared. (**a) Topological AFM images of bismuth ferrite nanostructures with average height 45 nm. Scan area: 4 × 4 μm. (b) MFM image (4 × 4 μm) of the ***same*** region as in (b). The insert image is the marked particle enlarged 4 times.

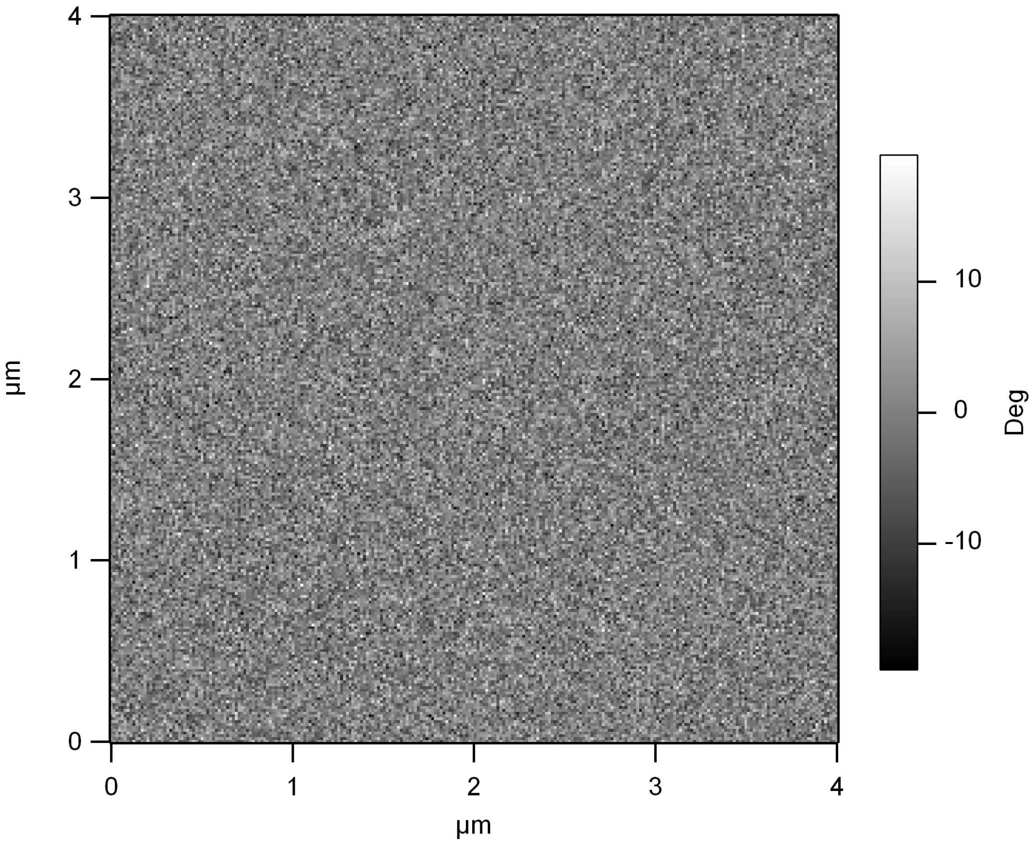

Figure 2.10 **EFM image of the BFO thin film without bias voltage and using a delta height of 50 nm.**

2.3.1.c Electric ordering induced by electric field

The KPFM was performed to observe polarization switching properties of the BFO film with a delta height ΔZ=50 nm (the distance between the tip and the sample surface). The polarization was induced and recorded by KPFM to verify the electric orderings of BFO thin film. Figure 2.11 shows in (a) topographical surface of BFO film having an average height of 45 nm whereas (b, c, d) are the same area imaged by applying various DC bias (-1V, +1V, and +2V) on the surface to induce electric polarization and show potential features corresponding to particles with induced dipole. In order to remove the already existing surface charge and to observe the polarization, an AFM scan with zero bias was performed on the same region using a contact mode with a grounded tip.[64] We, then, applied DC bias at different levels, -1, +1 and +2 V, from the substrate to induce the polarization. The surface potential image (Figure 2.11b) at -1 V DC bias shows clearly that negative (~ -10 mV) and positive (~ 10 mV) polarization on the surface of BFO thin film. After changing the DC bias from -1 V to the opposite direction of +1 V on the surface of BFO thin film, the polarization of BFO thin film diminished to about 0 (Figure 2.11c). When a higher positive bias of +2V DC was applied, a nearly inverted image was observed (Figure 2.11d vs. Figure 2.11b), indicating clearly that the polarization direction of the ferroelectric domains was reversed by the external electrical field. It was also observed that the electric polarization maintained for at least 19 hours with only a moderate decrease after the electrical field was withdrawn.

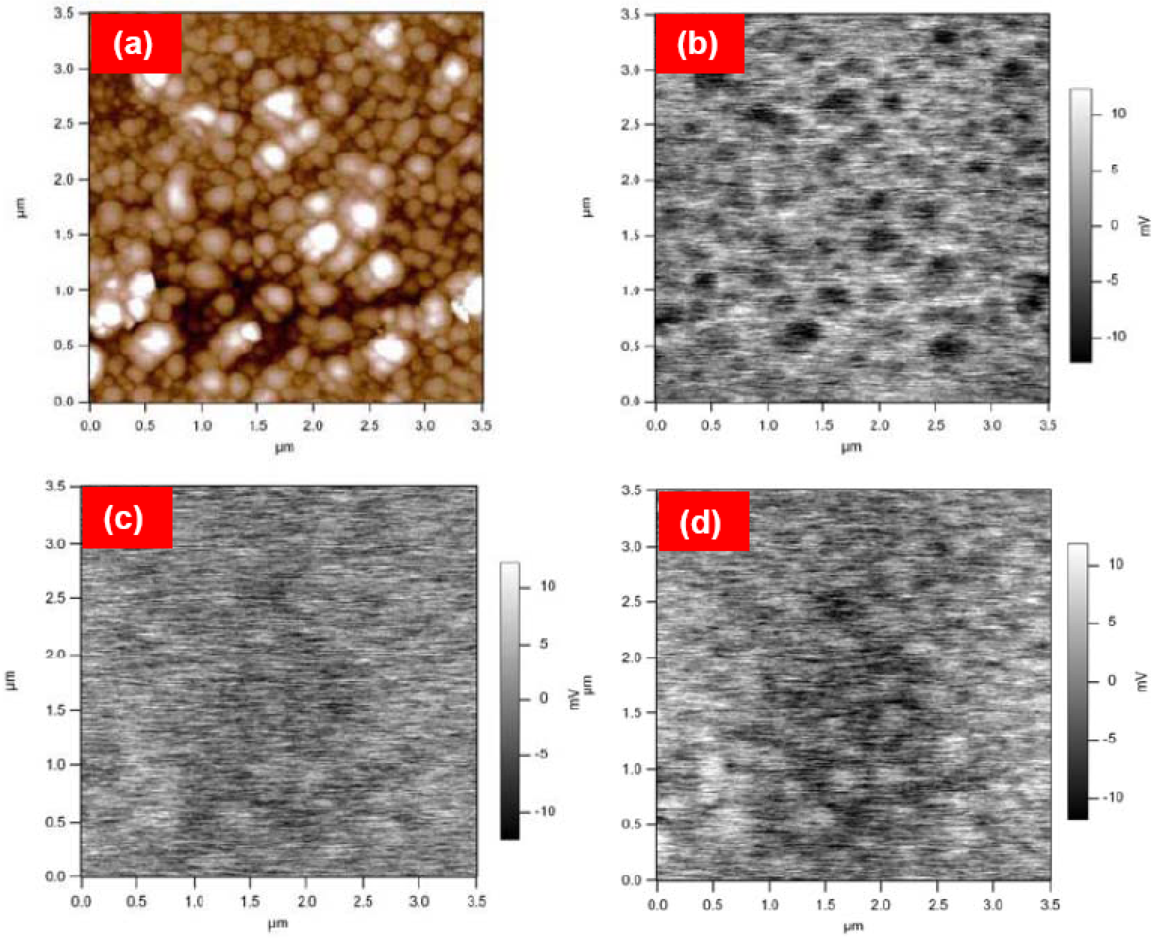

Figure 2.11 **Surface potential (SP) KPFM maps of BFO thin film.** AFM topography (brown) and surface potential (SP) maps (gray). Scan area: 3.5 × 3.5 µm. These maps are from continual scanning in the same area with 10 min required for each scan. (a) Topological AFM image of BFO thin film particles with average height 35 nm. (b) SP images for the same area of BFO thin film with (b) -1V DC bias, (c) +1V DC bias and (d) +2V DC bias. Delta height ΔZ=50 nm.

2.3.1.d Magnetoeletric coupling

2.3.1.d2 Magnetic ordering induced by electric field

To demonstrate the electric field induced magnetic ordering of the BFO thin film, an external electrical field was applied first to the sample when MFM experiments were performed to image and manipulate magnetism of BFO film. The magnetic tip was lifted further from 82 nm used for MFM experiment to 100 nm (ΔZ=100 nm) to negate the influence from the previously existing sample magnetic field. At ΔZ=100 nm, the MFM phase image (Figure 2.12b) does not show significantly magnetic interaction between the tip and the surface, indicating the influence on the magnetic tip was reduced to a negligible level. By applying various levels of DC bias to induce magnetism of BFO film surface, the magnetism images were observed by MFM. Figures 2.12a and 2.12b show topography and magnetic images without applying bias. Electric field was then applied on the Au substrate, the induced magnetic ordering of BFO film was recorded (Figures 2.12c-g in varying bias levels). To monitor the levels of influence of electric field on magnetism of BFO film, ±2 V and ±4 V DC bias were applied from the Au surface for separate sets of scan (Figure 2.12c-f). It was established that higher bias field led to stronger magnetic ordering. The time scale of the response was demonstrated by a single 10-minute scan with bias stepped in the sequence of -4 V, -2 V, zero, +2 V, and +4 V (Figure 2.12g). These cycles can be repeated many times. The magnetic ordering can be controlled with bias voltage and removed in less than one minute by simply retracting the applied field (0 V) (Figure 2.12g). The featureless EFM image (Figure 2.13) of the BFO thin film, conditions same as MFM, was obtained with a lower delta height of 50 nm and +3V bias from Au surface. This EFM control experiment established our MFM contrast was of magnetic origin.

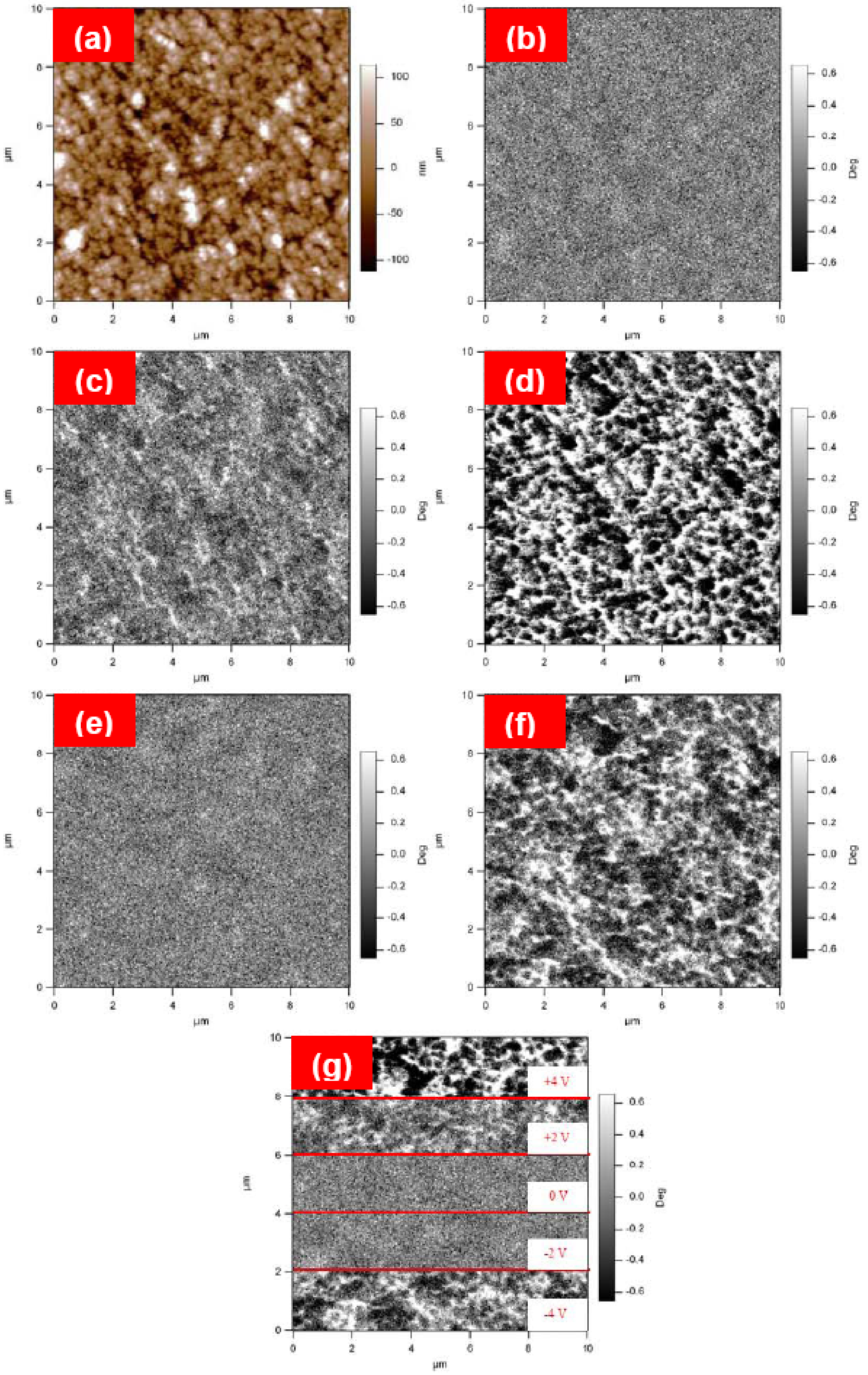

Figure 2.12 **Magnetic ordering induced by electrical field.** AFM topography (brown); magnetism induced by electric filed (gray). Scan area: 10 × 10 µm. (a) Topological AFM images of bismuth ferrite nanostructues without applying DC bias. (b) Magnetic images (after AFM) of the **same region** as in (a) with delta height ΔZ=100 nm, no bias. (c) +2V DC bias was applied on the substrate. (d) +4V DC bias was applied. (e) -2V. (f) -4V. (g) DC bias was continuous applied in steps of -4V, -2V, 0V, +2V, to +4V during in one scan over a period of 10 min.

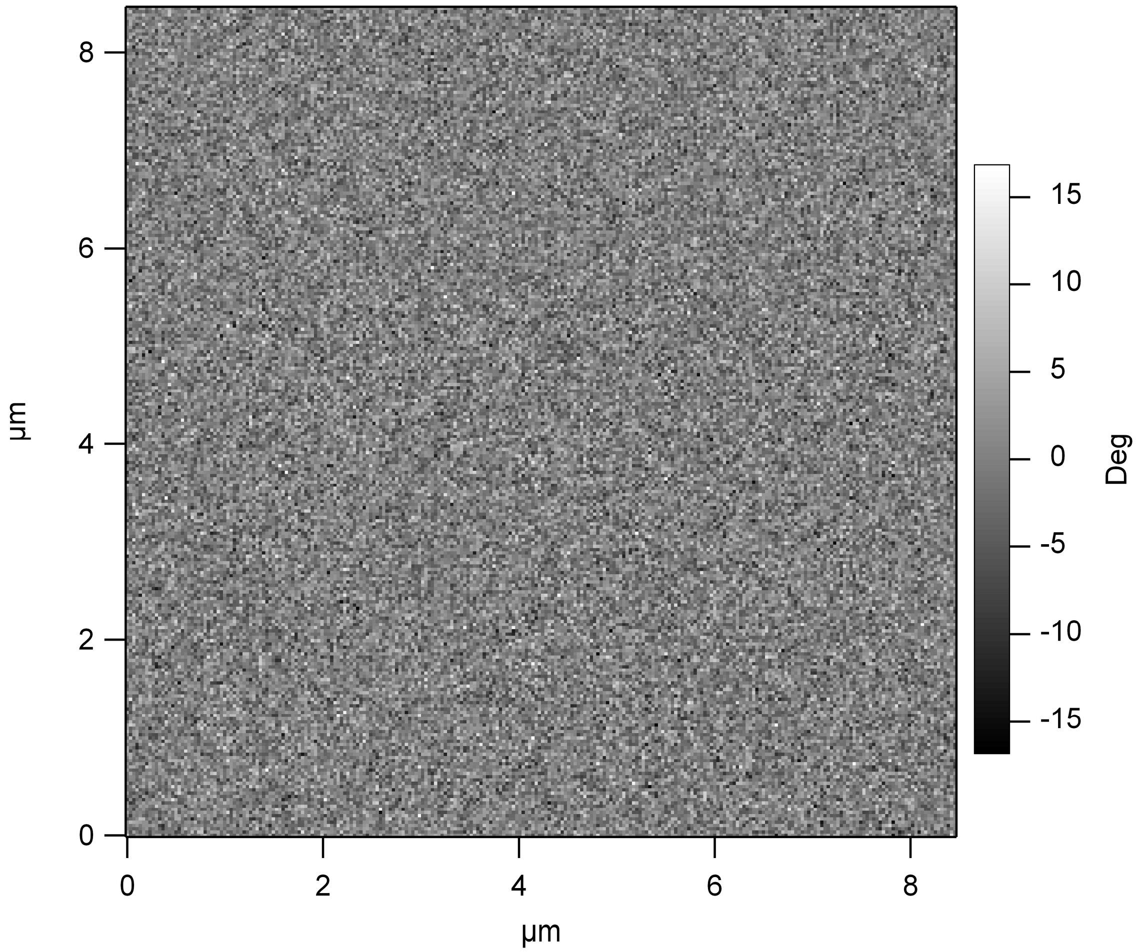

Figure 2.13 **EFM image of BFO with +3V bias voltage from the Au surface and using a delta height of 50 nm.**

2.3.1.d2 Electric ordering induced by magnetic filed

To study the electric ordering induced by magnetic field, the sample was placed in an external magnetic field before KPFM measurement. The imaging experiments are similar to normal KPFM, except there was no DC bias applied on the surface of BFO film. AFM topography (Figure 2.14a, 2.14c and 2.14e) was carried out first followed by KPFM study. The SP image was recorded with ΔZ=50 nm. Results from experiments on the same sample area with and without external magnetic field, were compared (Figure 2.14a vs. 2.14b; 2.14c vs. 2.14c and 2.14e vs. 2.14f). In the first experiment, the SP image of BFO film was mapped without neither electrical field nor magnetic field (Figure 2.14b), showing no significant SP on the surface of BFO film. After this first scan, BFO film was positioned between two poles of a magnet with a pole gap of ½ inch and a field strength of 10,500 Oe for 30 minutes and 17 hours. After 30 minutes and 17 hours of magnetization, the SP images were obtained and recorded (Figure 2.14d and 2.14f). As shown in Figure 2.14d, the image starts to show SP on the surface of BFO film after 30 minutes magnetization. After 17 hours of magnetization, SP image (Figure 2.14f) shows strong ferroelectric ordering. This is the *first* time magnetic field induced polarization was observed at room temperature. The induced electric ordering by magnetic field is not as efficient as magnetic ordering by electrical field (MFM images Figure 2.12b-g and SP images Figure 2.14d and 2.14f). For different external magnetization experiments, it is difficult to relocate exactly same area of observation (5 μm by 5 μm) for the sample.

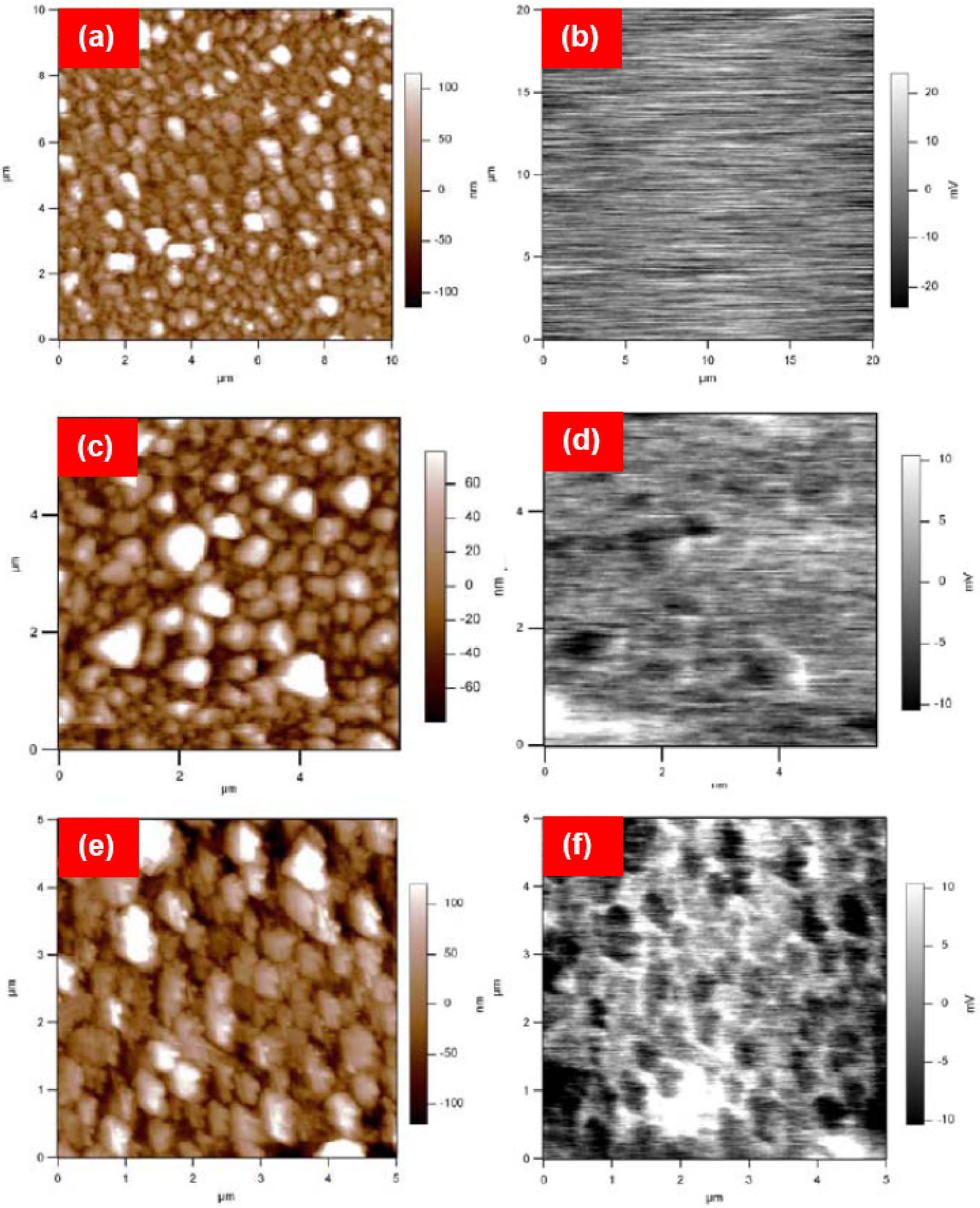

Figure 2.14 **Surface potential (SP) maps of electrical ordering induced by magnetic field.** AFM topography in brown; electric polarization induced by magnetic filed in gray. (a, b) Topography and SP images without applied magnetic field. BFO thin film positioned between two magnet poles (10500 Oe) with 0.5 inch pole gap for 30 mins (c, d) and 15 hours (e, f) before observation.

2.3.1.e Optically induced magnetic and electric orderings

In addition to the effect of electric and magnetic fields, a third applied field, optical irradiation was found to induce magnetic and electric orderings in BFO thin film. The multiferroic thin film formed on quartz substrate was fixed to a glass slide with a double-side adhesive tape and positioned on the stage. An external light beam from under the stage was focused on the sample during the MFM and KPFM observation. For optic-MFM, the delta height was at 50 nm. Optical absorption spectrum (Figure 2.15a) indicates that the glass slide and double-side adhesive absorbed about 20% light from wavelength of 300 to 600 nm, and BFO sample absorbs most of light between wavelength of 300 to 450 nm. The topography (Figure 2.15b) and MFM phase image (Figure 2.15c) with weak magnetic ordering were observed before irradiation. Then, various levels of light intensity from 6, 12, to 26 mW/cm^2 were applied and monitored by a Dymax ACCU-CAL™ radiometer. The light beam followed the path of glass slide/tape/quartz to BFO film. Figures 2.15c-f show magnetic orderings increases as the total light intensity increases

To examine the effect of wavelength, a set of experiment was carried out with an additional filter placed between the light source and glass slide. The filter cut off light with wavelength higher than 450 nm. The total intensity of UV light was further increased from 26, 237 to 560 mW/cm^2. The added filter transmitted 60% of the incoming light in the region of 350 to 450 nm with a long wavelength cut off at 450 nm (Figure 2.16a), resulting in higher ***total*** light energy for inducing magnetic orderings (Figure 2.16d-f). The topography (Figure 2.16b) and MFM images (Figure 2.16c) before incident light were observed. The MFM images show very weak magnetic orderings, even though the total light intensity was increased around 10 times (Figure 2.16e vs. 2.15f). Until light intensity increasing to 560 mW/cm^2 (around 21 times), the magnetic orderings were just observed (Figure 2.16f). It is clear that the efficient action light has wavelength longer than 450 nm. The same wavelength region was reported to be effective in generating photovoltaic effect BFO.[29]

To demonstrate electric ordering induced by light, the KPFM was employed to map surface potential of BFO thin film while being irradiated. Figure 2.17a, b indicate no polarization on BFO thin film in the absence of light. With applying various levels of intensity of light from 106, 263 to 315 mW/cm^2, SP images (Figure 2.17c-h) indicate a slight induced electric orderings. The SP images appear to correspond to topographies. The induced electric ordering by light is not as efficient as magnetic ordering as indicated by a comparison of SP images (Figure 2.17d, f, h) with MFM images (Figure 2.15d-f). Under our experimental conditions, less than 15% of the incoming light from under the stage can arrive at the sample side close to the scanning tip. At this present, it is not possible to arrange irradiating from above due to blockage by the cantilever.

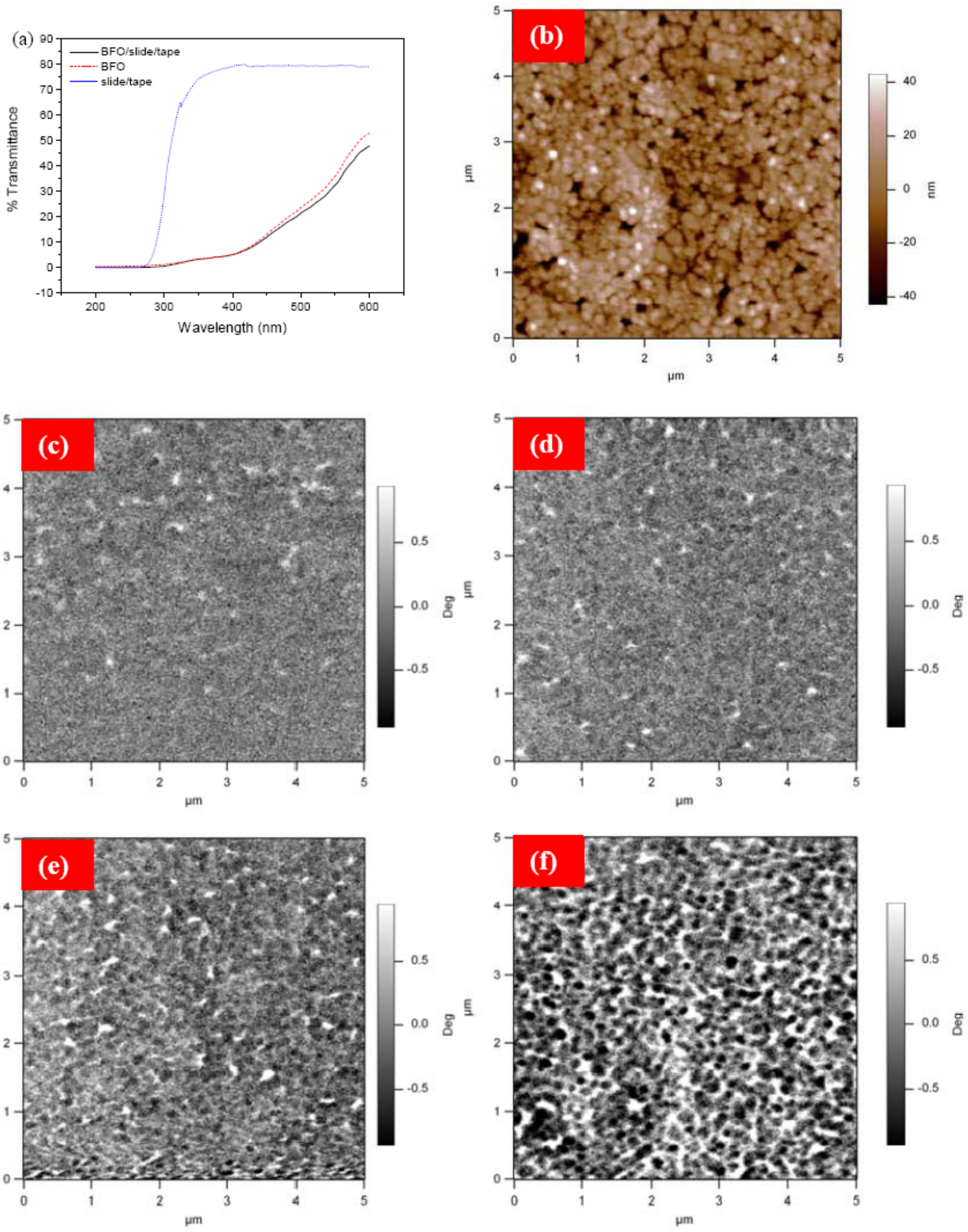

Figure 2.15 **Magnetic ordering induced by light.** Delta height ΔZ=50 nm. Scan area: 5 × 5 µm. (a) UV/vis spectrum of BFO thin film, tape and glass slide. (b) Topography of BFO thin film. (c) Magnetic image of BFO thin film without applying light. Magnetic images with applying light. (d) 6 mW/cm^2, (e) 12 mW/cm^2, (f) 26 mW/cm^2.

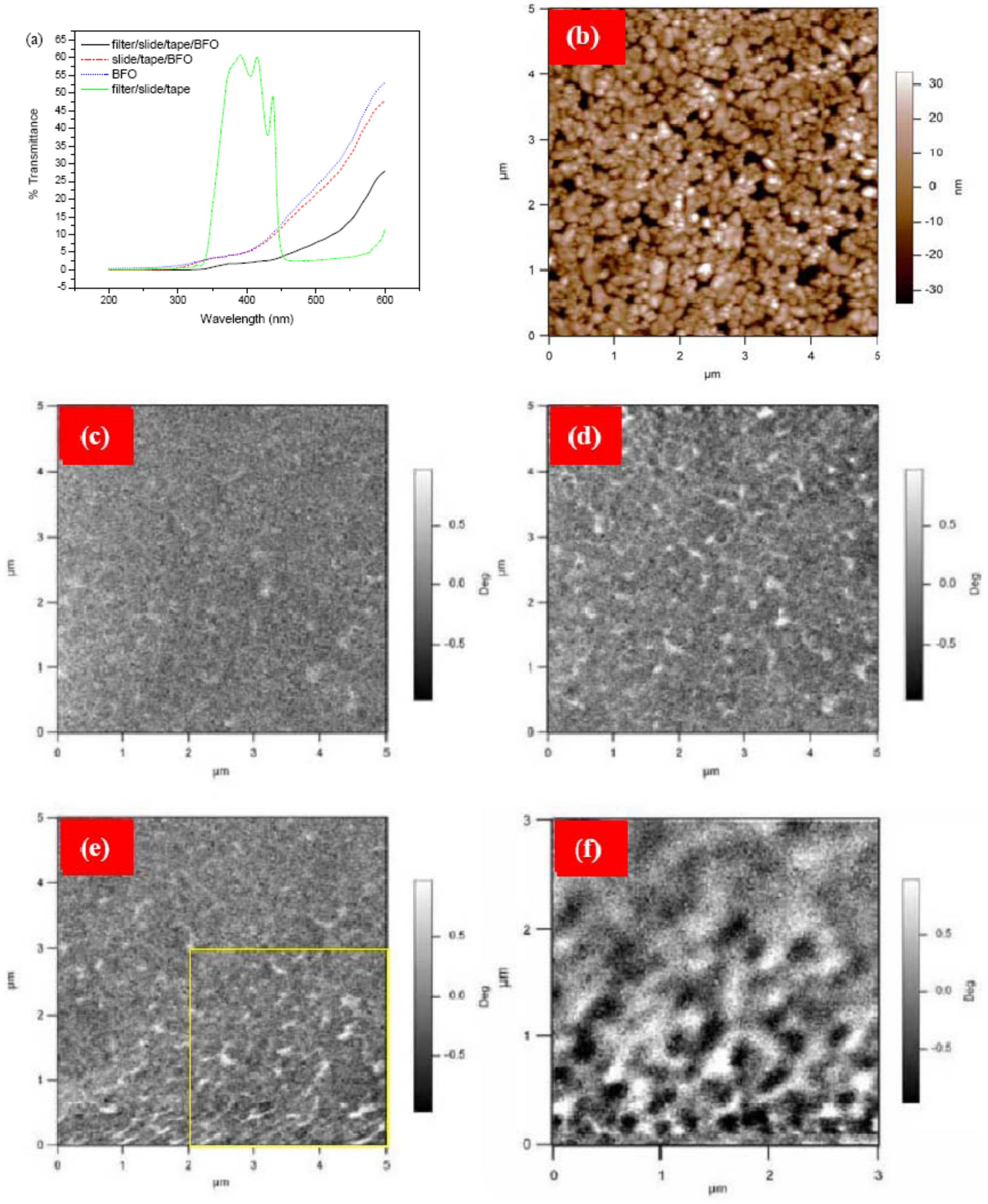

Figure 2.16 **Magnetic orderings induced by light with band a filter.** Delta height ΔZ=50 nm. Scan area: 5 × 5 μm. (a) UV/vis spectrum of filter and filter/BFO thin film. (b) Topography of BFO thin film. (c) Magnetic image without applying light. (d-f) Magnetic images with applying light through filter. (d) 26 mW/cm^2, (e) 237 mW/cm^2, (f) 560 mW/cm^2.

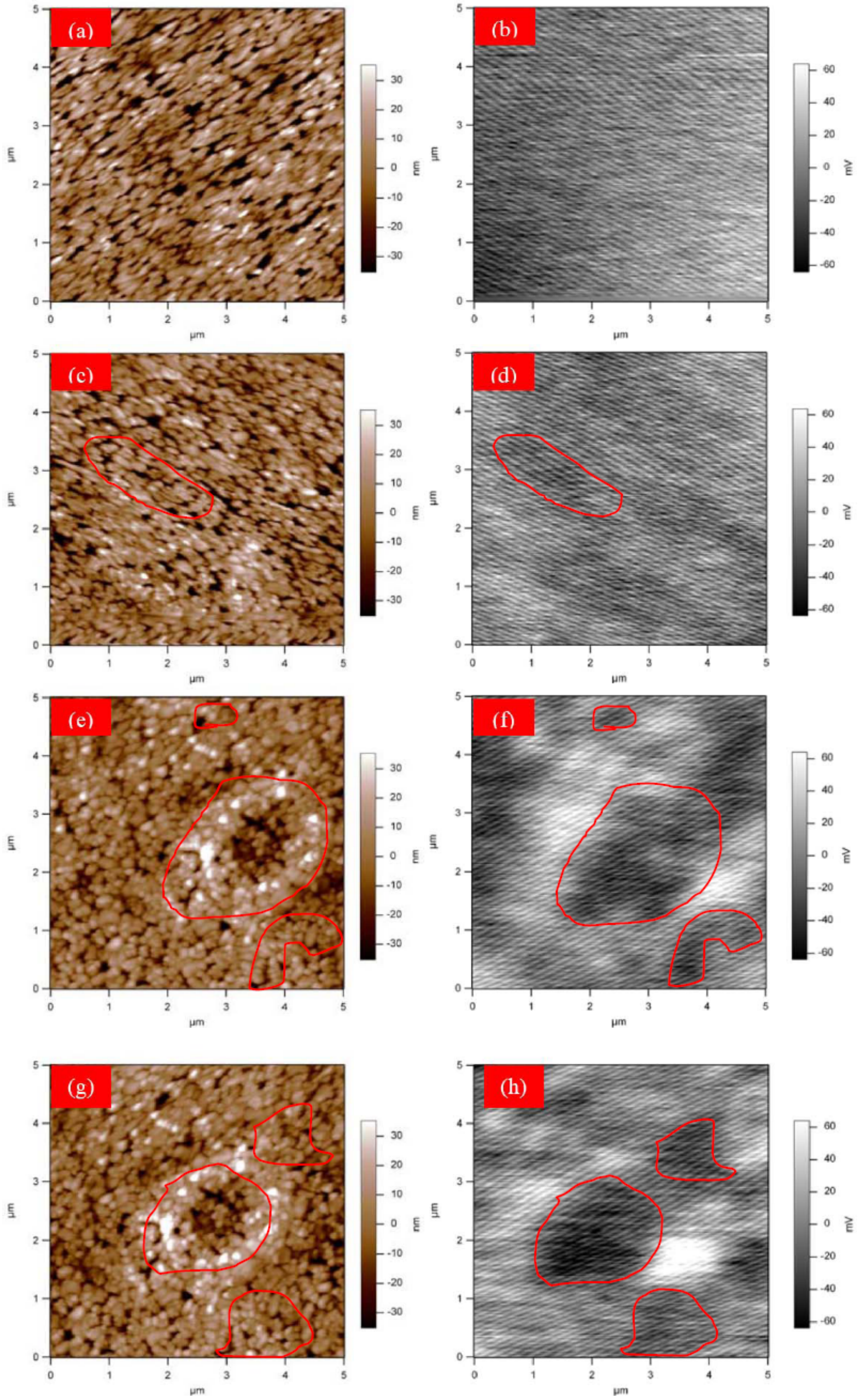

Figure 2.17 **Electric orderings induced by light.** Delta height ΔZ=50 nm. Scan area: 5 × 5 μm. AFM topography (brown) and surface potential (SP) maps (gray). (a, b) Surface potential (SP) images without applying light. (c-h) SP images with applying light. (c, d) 106 mW/cm^2, (e, f) 263 mW/cm2, (g, h) 315 mW/cm^2.

2.3.2 Autoclave synthesis

The autoclave method gave nanocrystal powders of one of the ferrites depending on heating temperatures. Nanocrystal powders of $Bi_2Fe_4O_9$ and BFO were obtained from the same precursor solution reacting for 24 hours at 165 and 185 °C. The XRD patterns of crystal nanoparticle clearly show an orthorhombic structure of $Bi_2Fe_4O_9$ (Figure 2.18a) with space group *Pbam* (JCPDS No. 25-0090) and $BiFeO_3$, a rhombohedrally distorted perovskite (Figure 2.18b, powder; Figure 2.5a, nanocrystal thin film) with space group *R3c* (JCPDS No. 86-1518). In addition, EDS spectrum confirms that the elemental composition ratio of Bi/Fe is 1/2 for $Bi_2Fe_4O_9$ (Figure 2.19 and Table 2.3) and 1/1 for BFO (Figure 2.20 and Table 2.4), supporting the XRD results. The morphologies of $Bi_2Fe_4O_9$ and BFO nanocrystals were examined by TEM. The TEM images show the average diameter of $Bi_2Fe_4O_9$ particles is about 250 nm (Figure 2.21) and BFO particles, about 100 nm (Figure 2.22). The magnetic and ferroelectric orderings of BFO autoclave nanocrystals were, then, established by MFM and KPFM.

For magnetic ordering study, the MFM phase image shows the magnetic properties of BFO particles from autoclave method. Topography image of BFO with an average height of particles of 100 nm was obtained (Figure 2.23a). In the second scanning with delta height of 50 nm, the phase image (Figure 2.23b) shows dark particle contrast on the surface of BFO sample, corresponding to particles in the topography image.

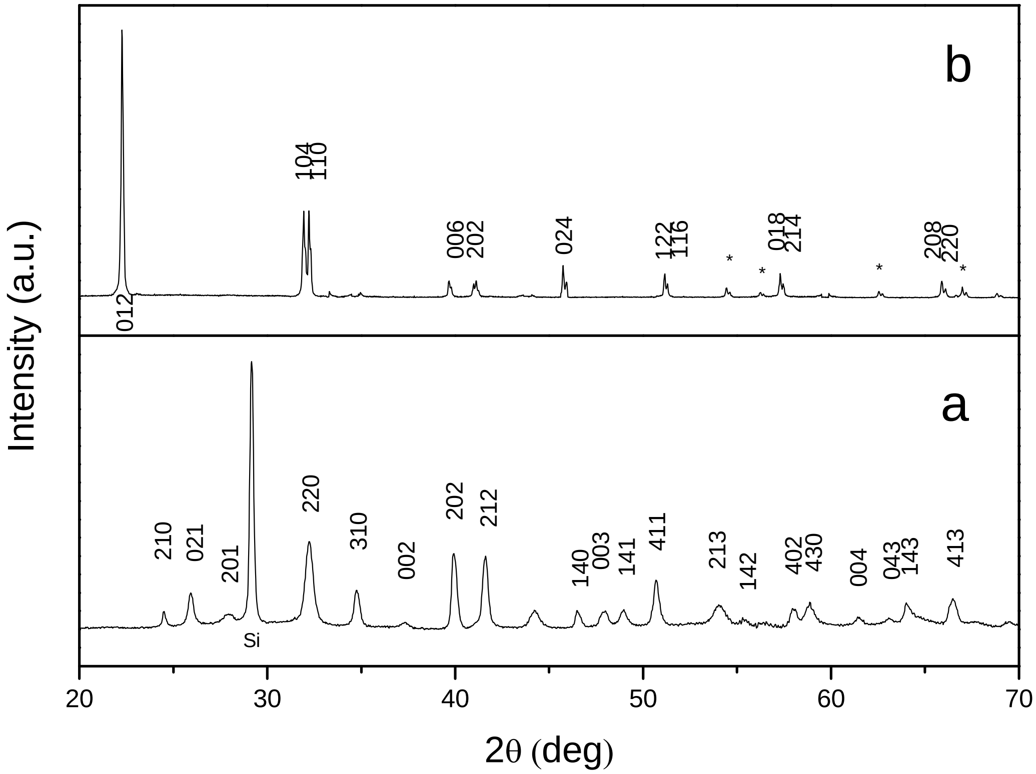

Figure 2.18 **X-ray diffraction patterns of autoclave samples.** (a) $Bi_2Fe_4O_9$ nanocrystal powder 165 °C; (b) BiFeO3 nanocrystal powder prepared by at 185 °C. (*-$Bi_2Fe_4O_9$)

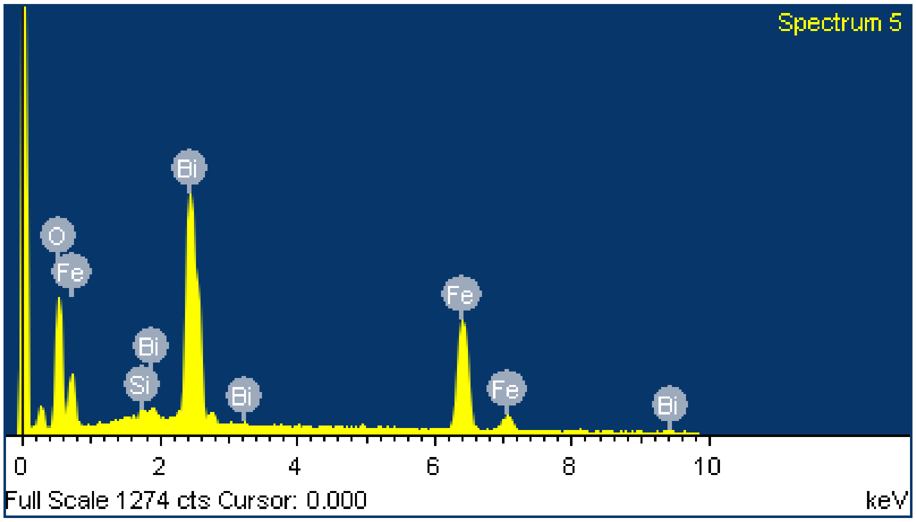

Figure 2.19 **X-ray Energy Dispersive spectroscopy (EDS) spectrum for $Bi_2Fe_4O_9$ nanocrystal powder made by autoclave at 165 °C.** The quantitative result shows a Bi/Fe ratio of 0.5, supporting the theoretical atomic ratio of 0.5.

Table 2.3 EDS quantitative results for $Bi_2Fe_4O_9$ show a Bi/Fe ratio of 0.5 for autoclave sample from 165 °C in agreement with theoretical atomic ratio.

Element	Weight%	Atomic%
O	28.10	71.90
Si	0.63	0.92
Fe	24.62	18.04
Bi	46.65	9.14
Totals	100.00	

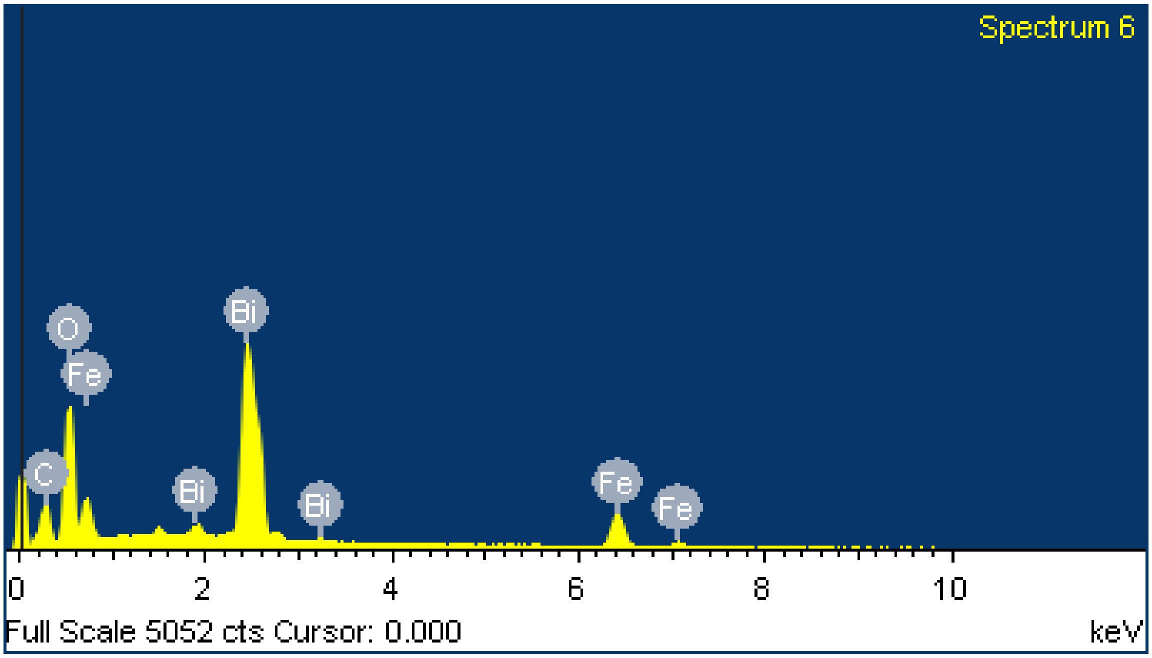

***Figure 2.20* X-ray Energy Dispersive spectroscopy (EDS) spectrum for BFO nanocrystal powder made by autoclave at 185 °C.** The quantitative result shows a Bi/Fe ratio of 1, supporting the theoretical atomic ratio of 1.

Table 2.4 EDS quantitative results for BFO show a Bi/Fe ratio of 1 for autoclave sample from 185 °C in agreement with theoretical atomic ratio.

Element	Weight%	Atomic%
C K	8.49	24.38
O K	27.33	58.91
Fe K	13.52	8.35
Bi M	50.65	8.36
Totals	100.00	

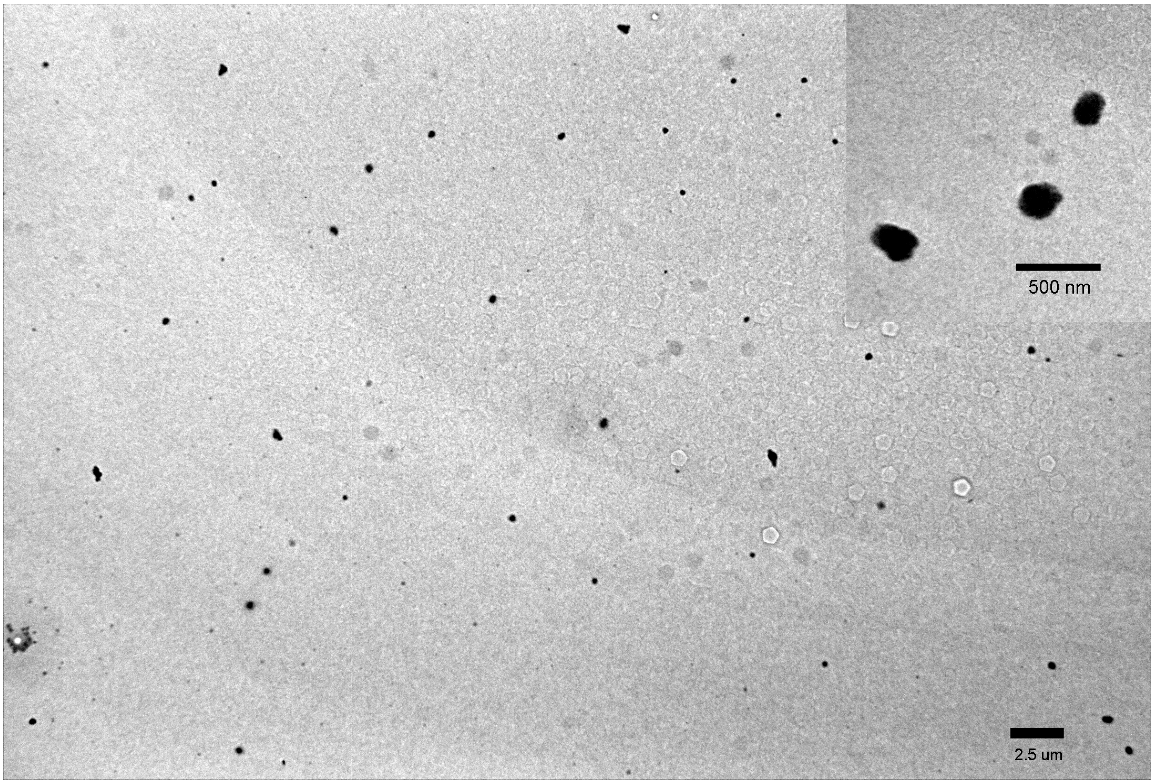

Figure 2.21 **TEM images of $Bi_2Fe_4O_9$ autoclave nanocrystal** (250 nm average diameter).

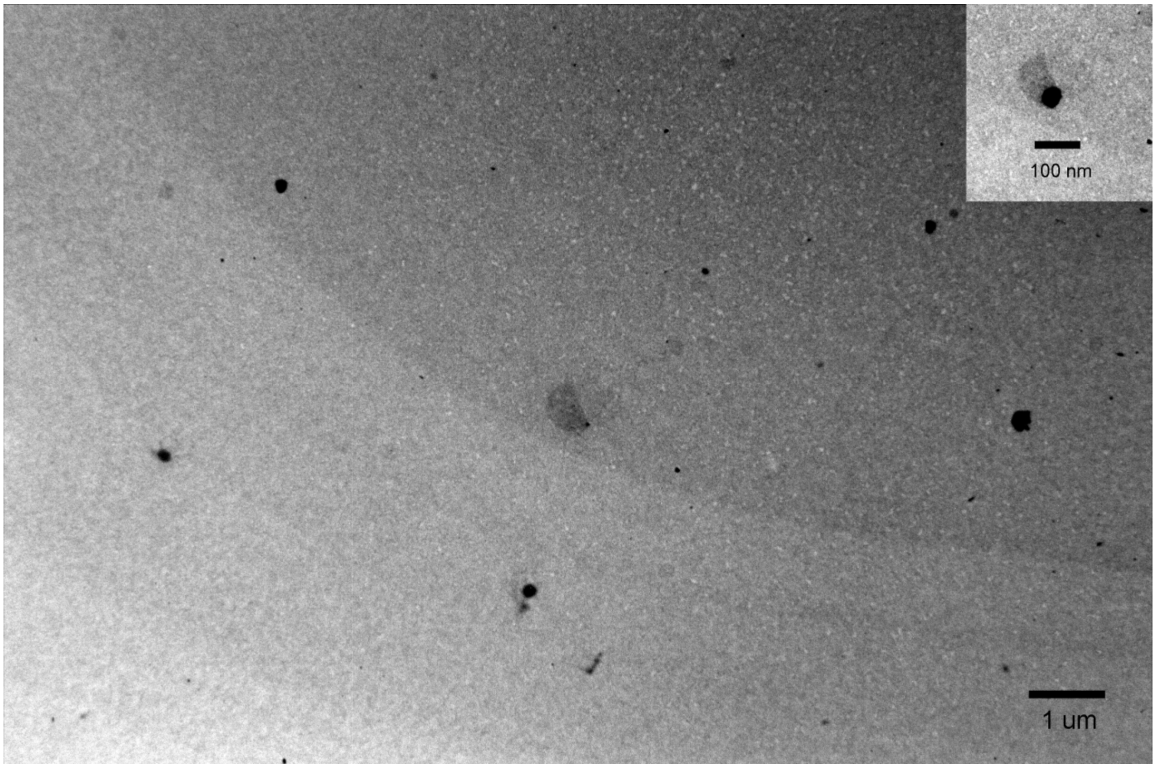

Figure 2.22 **TEM images of $BiFeO_3$ autoclave nanocrystal** (100 nm average diameter).

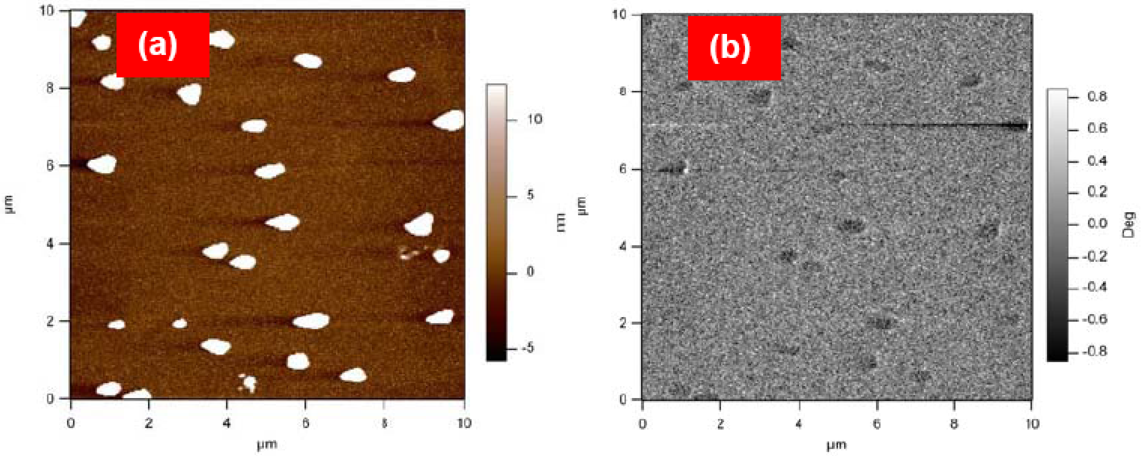

Figure 2.23 **AFM (a) MFM (b) image of BFO autoclave nanocrystals as prepared. (**a) Topological AFM images of bismuth ferrite nanostructures with average height 80 nm. Scan area: 10 × 10 μm. (b) MFM image (10 × 10 μm) of the ***same*** region as in (b). Delta height ΔZ=50 nm.

Electric polarization of the BFO crystal powder was examined using KPFM and dielectric spectrometer. Figure 2.24b and 24d-f show surface potential (SP) images (delta height of 50 nm). Figure 2.24 shows topography (a) of BFO autoclave nanocrystal particles (average height ~100 nm) and SP (b) image without DC bias. To improve the observation of the switching behavior of electric ordering, the scanning area was reduced from 10×10 µm to 5×5 µm. Two levels of DC bias (±1V DC), were applied on the substrate of BFO sample. The topography (Figure 2.24c) and same area SP images (Figure 2.24d-f) of BFO were recorded by KPFM. Figure 2.24b shows the original polarization with positive surface potential before applying bias. A DC bias of +1V was applied (Figure 1.24d) and a 10 min scanned was conducted from lower region to upper region. The polarization of SP image evolved from positive to negative, (white to dark) during the scan in 5 min of application of bias voltage, the particles lost their positive (+15 mV) polarization and finally switched to negative (-15 mV). The scanning was continued with +1 V, but in the reversed direction from top to bottom region resulting in "negative polarization" for the entire frame (Figure 2.24e). Then a new scan with a "-1 V" bias was conducted, a fast switching ~1 min, to "positive polarization" was demonstrated (Figure 2.24f). Thus, KPFM measurement gave evidence for electric ordering and its switching behavior in the autoclave BFO sample. The dielectric constant of BFO and $Bi_2Fe_4O_9$ autoclave crystal samples were performed on a dielectric spectometer with frequencies from 1 µHz to 10 MHz (Figure 2.25 and Figure 2.26) and 1 V DC bias. For BFO autoclave sample, dielectric constant (106) and loss tangent (2.47) were obtained at 0.01 Hz (Figure 2.25); for $Bi_2Fe_4O_9$, 586 and 7.56 (Figure 2.26). For autoclave, $Bi_2Fe_4O_9$ has higher dielectric constant and loss tangent than BFO. Ferroelectric property of $Bi_2Fe_4O_9$ nanocrystal was reported before.[38]

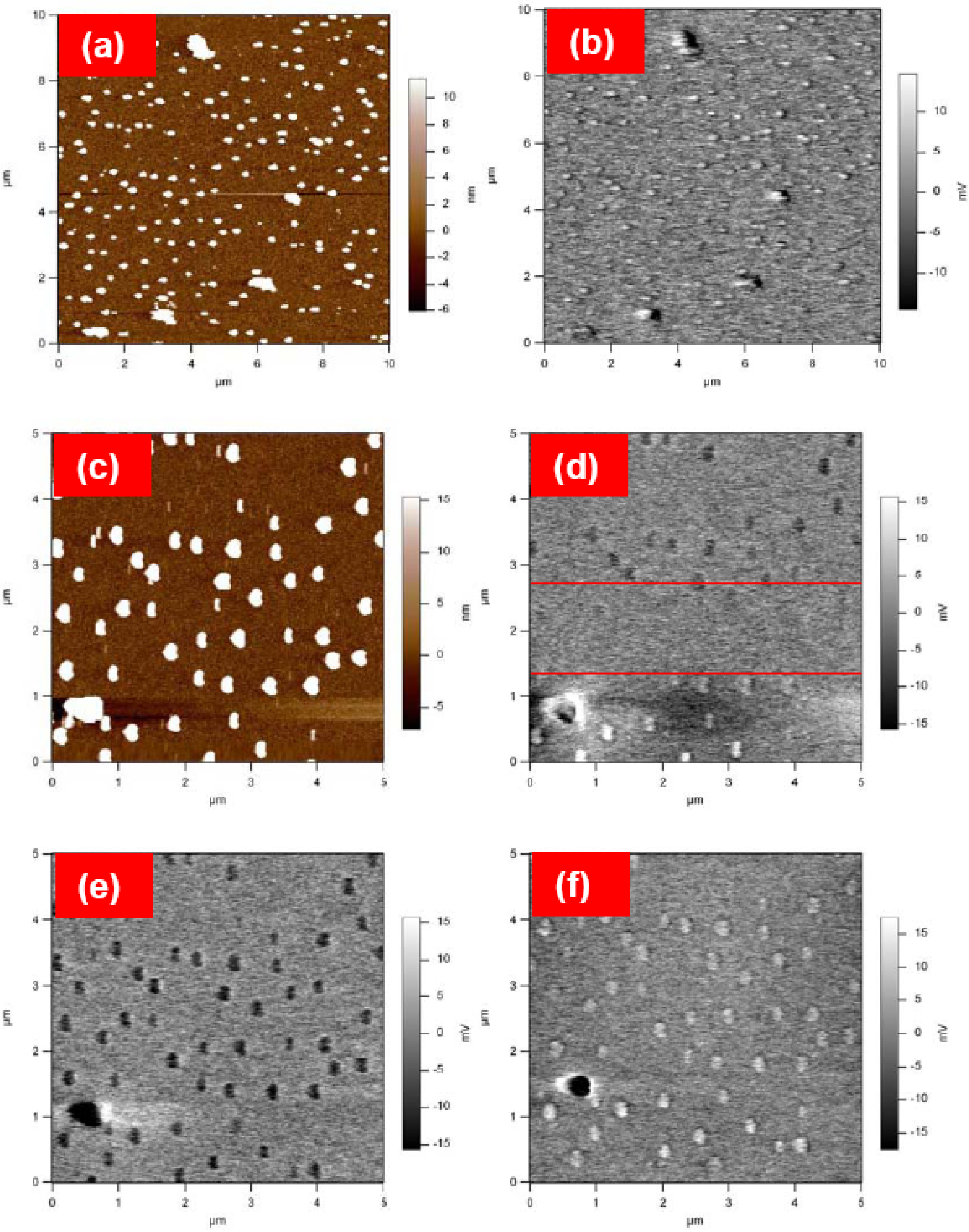

Figure 2.24 **Surface potential (SP) KPFM maps of BFO autoclave nanocrystals.** AFM topography (brown) and surface potential (SP) maps (gray). These maps are from continual scanning in the same area with 10 min required for each scan. (a, c) Topological AFM image of BFO autoclave particles with average height 80 nm. SP images for the same area (a) of BFO autoclave nanocrystals with (b) 0 V DC bias, and the same area (c) of BFO autoclave nanocrystals with (d, e) +1 V DC bias and (f) -1 V DC bias. Delta height ΔZ=50 nm.

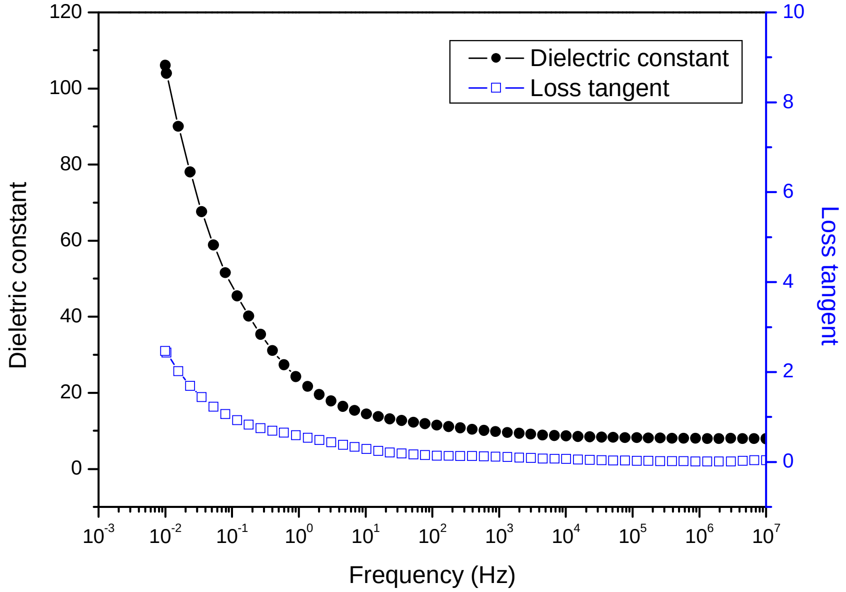

Figure 2.25 **Dielectric constant and loss tangent of $BiFeO_3$ autoclave nanocrystals at room temperature.**

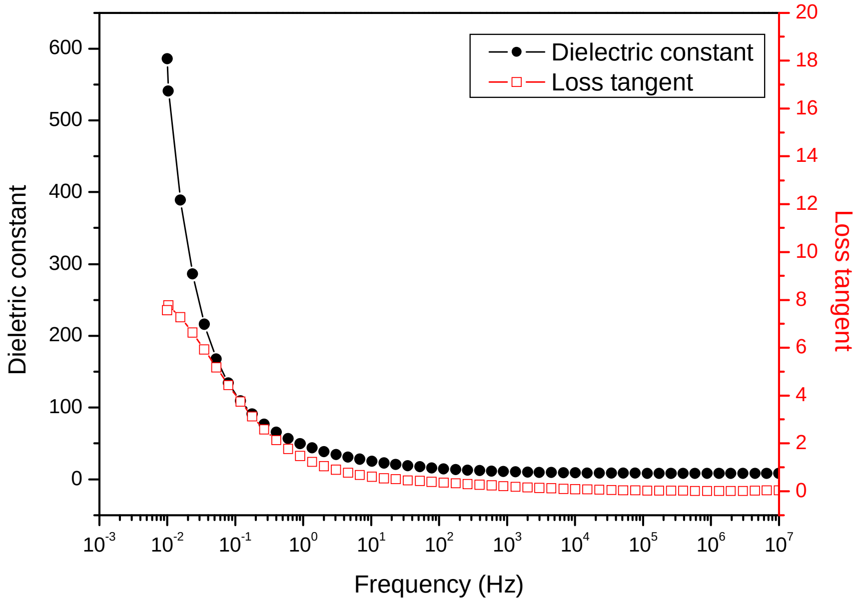

Figure 2.26 **Dielectric constant and loss tangent of $Bi_2Fe_4O_9$ autoclave nanocrystals at room temperature.**

2.3.3 Microemulsion synthesis

For microemulsion synthesis, the bismuth ferrite sample was also characterized using XRD, TEM, and dielectric spectrometer. XRD result indicates a non-crystalline bismuth ferrite. TEM image shows the average particles size of bismuth ferrite about 80 nm (Figure 2.27). For dielectric constant measurement, the result shows extremely high dielectric constant about 1,370,000 and loss tangent about 8 at 0.01 Hz. The loss tangent decreases at frequency below 176 Hz, and then reincreases to 2.66 at frequency 4510 Hz. After frequency larger than 4510 Hz, the loss tangent decreases again (Figure 2.28). The extremely high dielectric constant of 1,370,000 and the tangent loss peak at ~4.5 KHz requires further careful investigation.

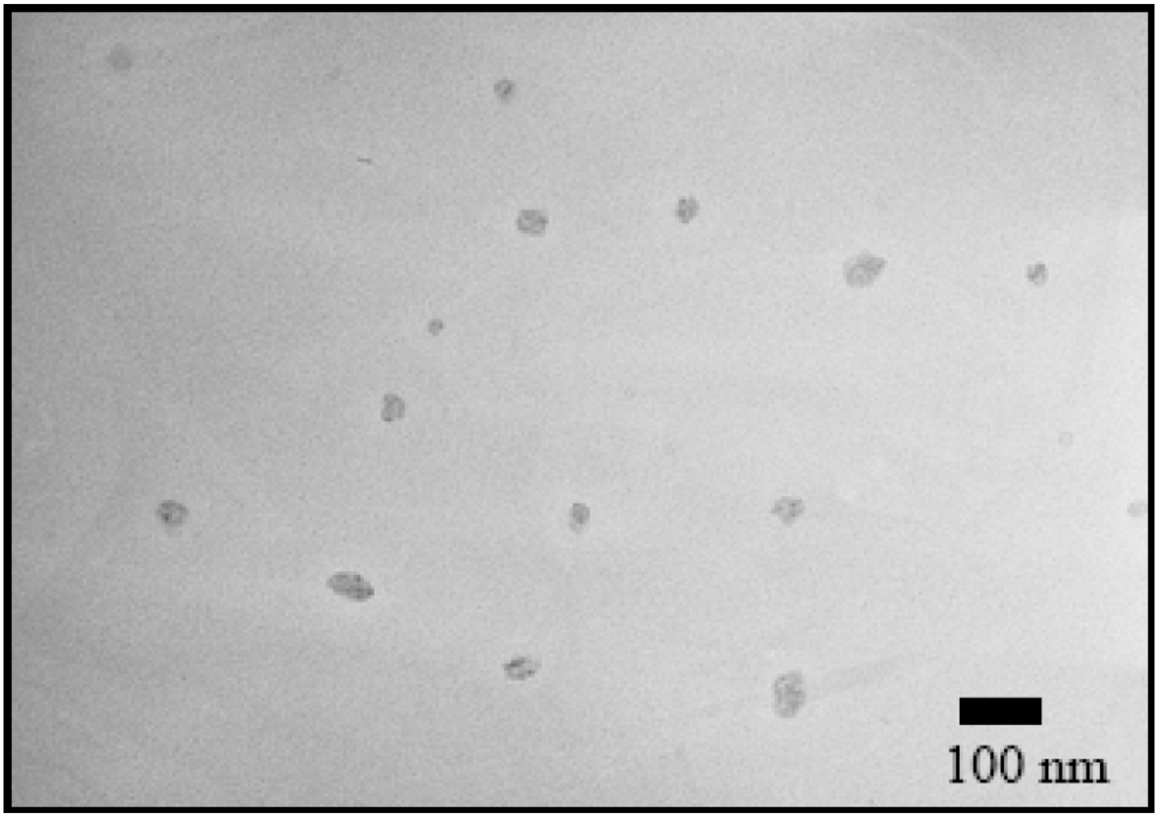

Figure 2.27 **TEM image of bismuth ferrite with average diameter of 80 nm made by microemulsion.**

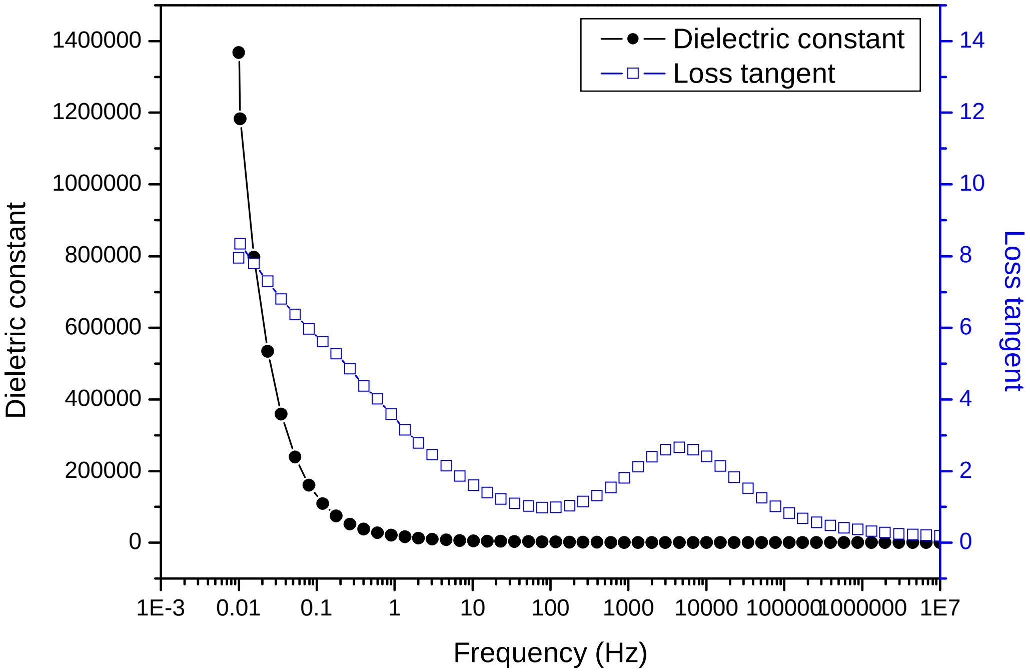

Figure 2.28 **Dielectric constant and loss tangent of BFO microemulsion particles at room temperature.**

2.4 Conclusion

Three approaches, spin-casting, autoclave, and microemulsion using one single precursor solution have been developed, giving bismuth ferrites of different morphologies and characteristics. Thin film of crystalline BFO (average diameter of 200 nm and thickness of 45 nm) of high quality was synthesized using a facile procedure of casting a precursor solution at a spinning rate 2000 rpm followed by heating 600 ºC. This finding represents a far more manageable process than the many existing methods. Nanocrystalline bismuth ferrite powders, $Bi_2Fe_4O_9$ (250 nm) and BFO (100 nm), were prepared by autoclave method at 165 ºC and 185 ºC respectively. Microemulsion synthesis gave non-crystalline bismuth ferrites powder in nanoscale (80 nm).

MFM images established magnetic ordering induced by magnetic field, electric field, and optical irradiation. Electric ordering was also shown to be induced by all three applied stimulus. Fast magnetic ordering response, within a minute, induced by electric field was observed. For electric ordering, SP images of BFO thin film show that electric ordering induced by electric field can be readily switched in the minute scale as demonstrated by applying -1V and +2V DC bias in successions. The response of electrical ordering to magnetic field (10,500 Oe) is much slower; 30 min was required to generate MFM image. Optically induced magnetic and electric orderings were also observed by MFM and KPFM. The light induced MFM images indicate that magnetic orderings could be efficiently generated by low energy level (26 mW/cm^2) radiation at wavelength longer than 450 nm. Light induced electrical ordering is much less effective than for magnetization under our current experimental arrangement. The finding concerning optic field is important. Experimental arrangement is being established to allow light with wavelength longer than 450 nm and irradiating directly on the sample surface from above as in near-field arrangement.

Compared with spin casting method, BFO from autoclave method shows much weaker magnetic ordering. The switching of BFO powder electrical ordering was observed in KPFM with ±1 V bias, at a similar level for BFO from spin casting. $Bi_2Fe_4O_9$ crystal powder, a well-known ferromagnetic material showed a dielectric constant of 600, higher than 110 from BFO crystal powder. Bismuth ferrite powder from microemulsion has an extremely high dielectric constant of 1,370K.

In summary, well-defined nanocrystal BFO thin film with uniform particles was successfully prepared by new facile method, spin-casting. Its magnetoelectric coupling and optical induced magnetic and electric orderings were observed at room temperature on the **same** BFO thin film thus prepared. This is the *first* time “magnetic-electric-optic” coupling at room temperature were observed in BFO nanocrystal thin film. The autoclave and microemulsion approaches for bismuth ferrites syntheses are not as versatile.

Chapter 3: Core-shell Nanomaterials from Conducting Polymer - Controlled Delivery and High-*k* Nanoparticle in Conductive Matrix

3.1 Core-shell nanostructure for controlled delivery

3.1.1 Introduction

In recent years, hollow submicron spheres have attracted intense research attention because of their wide variety of applications, including drug, dyes, or inks delivery, protection shield for proteins, catalysis applications, and gene therapy.[1-6] Conducting polymers are of considerable interest for a variety of applications due to their responsiveness to electric field to generate a change in conductivity, color, and volume.[6, 7] Nano and microscale conducting polymeric systems are already of widespread use for applications such as electronic devices, mechanical actuators, and chemical sensors.[8, 9] Their substantial volume change accompanying the doping/dedoping processes[10], serves as the base for many actuator applications.[10-12] Recently, new applications of conducting polymer have attracted increasing interest in the areas of controlled release because conducting polymers also offer the possibility of controllable drug administration through electrical stimulation and pH changing.[2, 6, 7, 13] Even though the development of polymeric controlled release system is still in the developing phase[5, 14, 15], the advance of nanotechnology continues to provide new techniques for the fabrication of hollow nanostructures.[6, 16-20] On the other hand, the use of conductive polymers in delivery systems has not been fully developed due to the limitations in choice of dopant for the polymer and the molecular weight of the delivered drug.

The establishment of the biocompatibility of PEDOT[10, 14, 21, 22] and polypyrrole (PPY)[13, 15, 21] expended the application areas of conducting polymers. In this dissertation, poly(3, 4-ethylenedioxythiophene) (PEDOT) was chosen as the polymer shell for nanospheres. Recently, biocompatibility PEDOT was used for important neural prosthesis and drug delivery applications.[6, 14, 22]

For the hollow sphere nanostructure syntheses, both template[23-29] and template-free[30, 31] processes have been broadly investigated for inorganic nanostructures with interior space. However, fabrication of PEDOT nanostructures is very challenging. To obtain hollow nanostructures, template-mediated polymerization processes were usually used. One-dimensional hollow nanostructures were first fabricated by using *hard-templates*, including track-etched membranes[32, 33], porous membranes[34-36], and biodegradable polymer fibers[6]. Figure 3.1 shows schematic for the preparation of 1-D hollow nanotubes performed inside the Al_2O_3 membrane pore.[35]

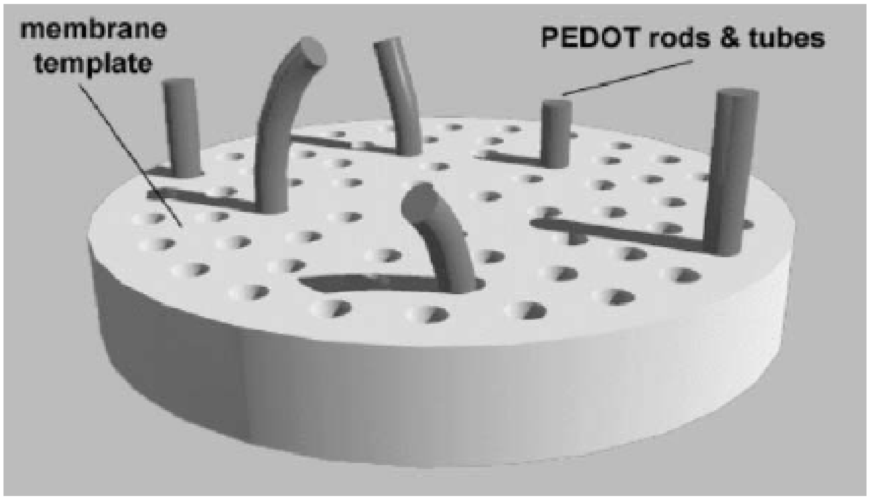

Figure 3.1 **Schematic illustration of the use of an Al_2O_3 membrane as a template in the synthesis of 1-D PEDOT structures.** (From Ref. 35)

Although the hard-template methods are effective for well-defined 1-demensional hollow nanostructures, the processes are relatively complicated and difficult to scale up. On the other hand, *soft-template* methods have also been developed. Soft-templates refer to self-assembled or liquid crystalline structures in which 1-dimensional conducting polymer nanostructures can be grown by chemical or electrochemical processes.[37, 38] Figure 3.2 illustrates the 1-D PEDOT hollow nanofibers prepared from a soft-template of aqueous anionic surfactant solution. TEM images confirm that nanofibers are hollow structures.[38]

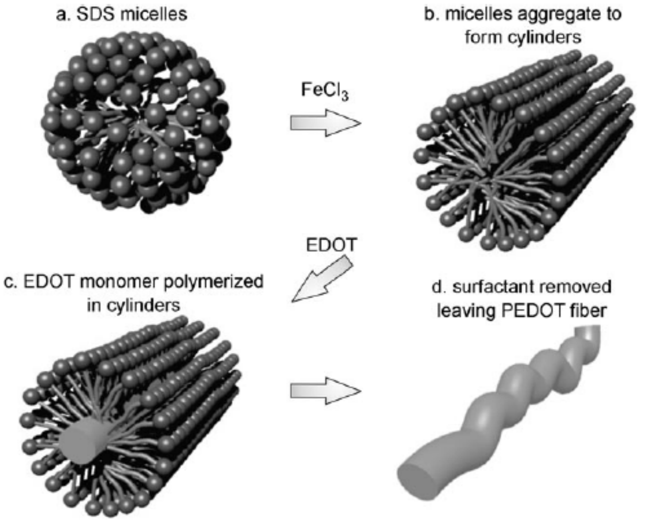

Figure 3.2 **Schematic illustration of the procedure for the synthesis of PEDOT nanofibers in cylindrical surfactant micelles.** (From Ref. 38) (Hollow nanofibers structure showed by TEM)

More intricate cases are the fabrication of nano-capsules or -vesicles. The hard-templates for the fabrication of nano-vesicles are not easy to remove compared with the cases for 1-dimensional nanostructures.[39-41] Recently, PEDOT nanosphere with cyclohexane core was prepared.[16] In this dissertation, an efficient methodology of interfacial polymerization was demonstrated for the fabrication of the core-shell nanospheres. PEDOT serves as the shell for a core of room-temperature ionic liquid (RTIL) in a micelle system established in water mediated by a nonionic surfactant, triton X-100 (TX-100). There are advantages of using RTIL micelles as the *soft-templates compared with cyclohexane system*[16]. With their nonvolatile, thermally stable and tunable solvation properties, Biocompatible RTILs are considered as promising candidates for both chemical and biological applications.[42-45] With the formation of the PEDOT shell, chemical or biological substances can be encapsulated in the core. Also, due to the nonvolatile nature of RTILs, loading loss through evaporation in preparation is likely to be very low.

The current study provides a novel platform for controlled release triggered through stimulation by pH tuning. Scheme 3.1 illustrates the mechanism for volume change in conducting polymers by doping/dedoping processes. Two volume change mechanisms can be considered.[10] There are positive charges on the backbone of conducting polymer as synthesized by oxidation polymerization (doped state). To maintain charge balance, the equivalent counter ions (anions) need to be present in the matrix of conducting polymer (Scheme 3.1 Doped state). After electric or pH value tuning, the volume of conducting polymer changes to “dedoped state I or II” depending on the size of counter ion. If the size of counter ion is large, the volume expands after stimulation as Scheme 3.1 “Dedoped state I”. Because the backbone of conducting polymer becomes less positive and counter ions cannot move out of matrix of conducting polymer, the cations migrate into the polymer matrix for charge compensation, causing expansion. On the other hand, if the size of counter ions is small, the volume of conducting polymer shrinks because small counter ions with solvent are expelled (Scheme 3.1 “Dedoped state II”).

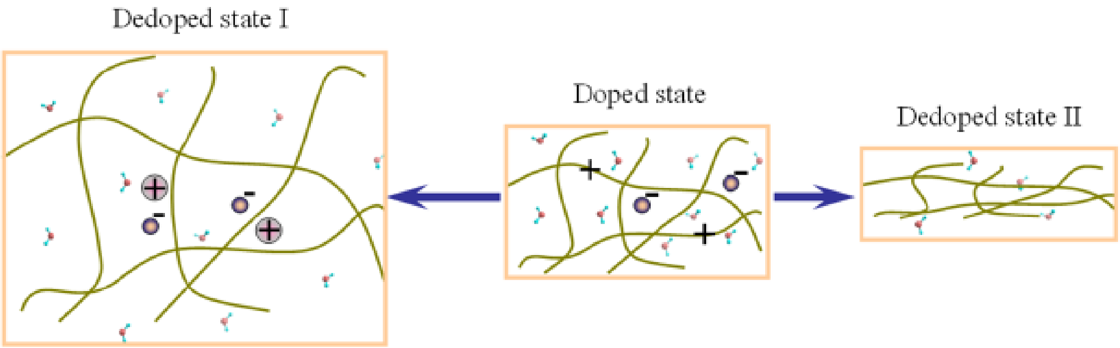

Scheme 3.1 Proposed mechanism for volume change in conducting polymers. ◉ represents a dopant.

On the basis of the substantial volume changes in conducting polymers, two controlled release strategies through the size shrinkage and expansion of polymer nano-shells were demonstrated in this dissertation with the synthesis of a series of core-shell PEDOT nanospheres for controlled release. By TEM and SEM observation, the optimum reaction conditions for single-chamber nanospheres were established. Different sizes of PEDOT spheres were prepared by changing the ratio of RTIL-to-surfactant ratio, *R*. The volume changes of PEDOT nanospheres for controlled release were observed by SEM. The controlled release behavior of PEDOT nanospheres was monitored by photometric measurement.

In addition in a novel nanosystem, the interaction of electronic polarization with atomic polarization was studied for core-shell nanosphere of polyaniline (PANI) matrix with high-*k* strontium titanate (STO) nanoparticles embedded. The synergistic polarization effect in core-shell of PANI/STO nanoparticles was established by KPFM.

3.1.2 Experimentals

3.1.2.a Hollow sphere synthesis

All reagents were purchased from Aldrich Chemical Co. and used without further purification. In a typical synthesis, 3, 4-ethylenedioxythiophene (EDOT) in 1-butyl-3-methyimidazolium hexafluorophosphate (bmimPF$_6$, i.e. ionic liquid, IL) with different concentrations (0.414, 0.207, 0.083 and 0.0414 mg/mL) serves as the dispersed phase, and ammonium peroxydisulfate (APS) oxidizer (8.36 mg/mL) in deionized water as the continuous phase. The micelle system was established by a surfactant "TX-100". The details of reaction compositions of *IL-A* to *IL-D* were listed in Table 3.1. The process of formation of polymer shell is depicted in Scheme 3.2. The APS and EDOT diffuse to the RTIL/water interface from opposite directions of the shell. The polymerization occurred at the interfacial surface of the RTIL micelles, forming core-shell polymer nanospheres (PEDOT as a shell and RTIL as a core). The interfacial polymerization was conducted at room temperature in a 20-mL vial with oil-in-water (O/W) microemulsion for 72 and 144 hours. For the study of a series of size of micelles, the micelles was tuned by variation of the RTIL-to-surfactant ratio, *R*, of 0.17, 0.24, 0.32, and 0.41, resulting in diameter of PEDOT nanospheres ranging from 75 to 400 nm. The detailed reaction compositions of *IL-E* to *IL-G* are listed in Table 3.2. To study volume change of PEDOT sphere, the transparent green suspensions were collected after reaction of 72 hours and the pH value was tuned from 4 to 12 by a step of 1 unit by adding small increments of concentrated ammonia solution. For controlled release behavior studies, model drugs, dipyridamole (28 mg, uncharged) and carboxylated curcumin (4 mg, anionic), were used as cargos. Before polymerization, the dipyridamole and EDOT monomer was dissolved in RTIL, and APS, in water. Polymerization occurred at interface, and the dipyridamoles were encapsulated in PEDOT nanospheres. The PEDOT sphere loaded with drug was collected after 72 hours. For the anionic carboxylatd curcumin, 0.56 g of tetrahydrofuran was added to the aqueous phase to improve solubility. Portion of the carboxylate curcumin was accumulated on the shell of PEDOT nanospheres. After 72 hours, the solution was collected for dialysis for 2 day to remove free carboxylate curcumin in the aqueous phase.

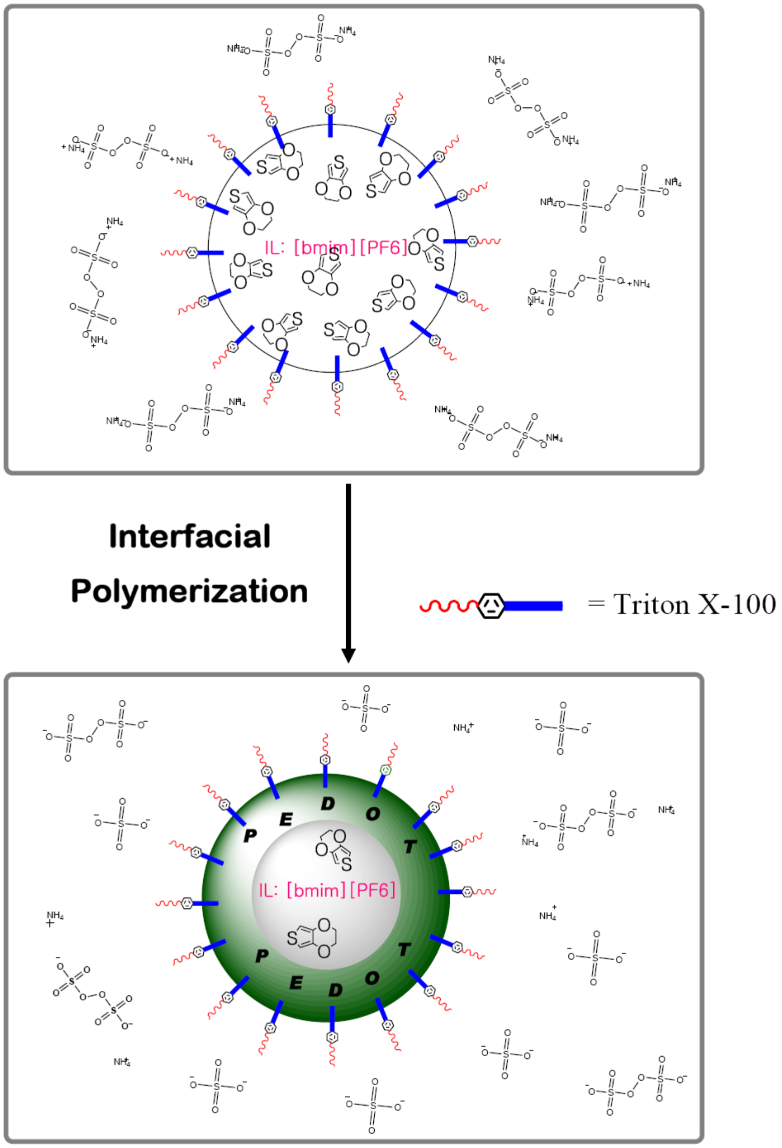

Scheme 3.2 Schematic presentation of formation of PEDOT nano-encapsulation by interfacial polymerization in a microemulsion system.

Table 3.1 Reaction compositions for preparing samples *IL-A* through *IL-D* with variations in EDOT concentrations

Sample ID	Water (g)	APS (mg)	TX-100 (g)	bmimPF$_6$ (g)	EDOT (mg)	$R = \frac{(bmimPF_6)}{TX-100}$
IL-A	8.37	70.0	1.50	0.10	30.0	0.17
IL-B	8.37	70.0	1.50	0.10	15.0	0.17
IL-C	8.37	70.0	1.50	0.10	6.0	0.17
IL-D	8.37	70.0	1.50	0.10	3.0	0.17

Table 3.2 Reaction compositions with different *R*'s for the preparation of samples *IL-B, and IL-E* through *IL-G* of varying sphere sizes

Sample ID	Water (g)	APS (mg)	TX-100 (g)	bmimPF$_6$ (g)	EDOT (mg)	$R = \frac{(bmimPF_6)}{TX-100}$
IL-B	8.37	70.0	1.50	0.10	15.0	0.17
IL-E	8.37	70.0	1.50	0.15	22.5	0.24
IL-F	8.37	70.0	1.50	0.19	28.2	0.32
IL-G	8.37	70.0	1.50	0.27	40.5	0.41

3.1.2.b Characterizations by TEM, SEM, HRTEM/Electron diffraction, Conductive-AFM, KPFM, UV/Vis and UV-Vis-IR absorbance

Morphology studies were conducted using scanning electron microscopy (SEM, LEO 982) and transmission electron microscopic (TEM) (JEOL 1200 EX microscope) at an acceleration voltage of 80 kV. For TEM samples, a drop of the reaction mixtures was dried on carbon-coated copper grids at room temperature. Samples for SEM were prepared on clean silicon wafers by spin-coating the reaction mixtures at 3000 rpm (photo-resist spinner, EC101DT-R485, Headway Research Inc.). The wafer was washed with pure methanol several times before use. HRTEM and electron diffraction were conducted on a Tecnai G2F20 cryoelectron microscope. UV/Vis spectrum was obtained at wavelength range of 300 to 600 nm (Thermo Electron Corporation, Helios Alpha, Beta) to follow PEDOT polymerization and cargo release. UV-Vis-IR spectra were collected from 400 to 1400 nm using a Cary 500 UV-Vis-IR Spectrophotometer. Conductive-AFM (CAFM) and Kelvin Probe Force Microscopy (KPFM) studies were conducted on a MFP-3D microscope (Asylum Research). For studying CAFM and KPFM, tapping-mode silicon cantilevers having a spring constant ~2 N/m and resonance frequency ~70 kHz (AC240TM-10 from Olympus) were used with Pt coated tips. DC bias was applied on the gold substrate to induce polarization during mapping surface potential.

3.1.3 Results and Discussions

In this synthetic system, the use of RTIL micelles in water can be classified as *soft-template* methods. The core-shell nanospheres of conducting polymer, poly(3,4-ethylenedioxythiophene) (PEDOT), were synthesized by "*interfacial polymerization*", Scheme 3.2. The progress of the polymerization was monitored by the visible absorbance change of the micelle system (Figure 3.3). Although reactions can be quenched by methanol at any stage of the reaction, the products were usually collected after 72 and 144 hours of reaction time. The collections showed a transparent appearance with green color, indicating the formation of PEDOT (Figure 3.3).

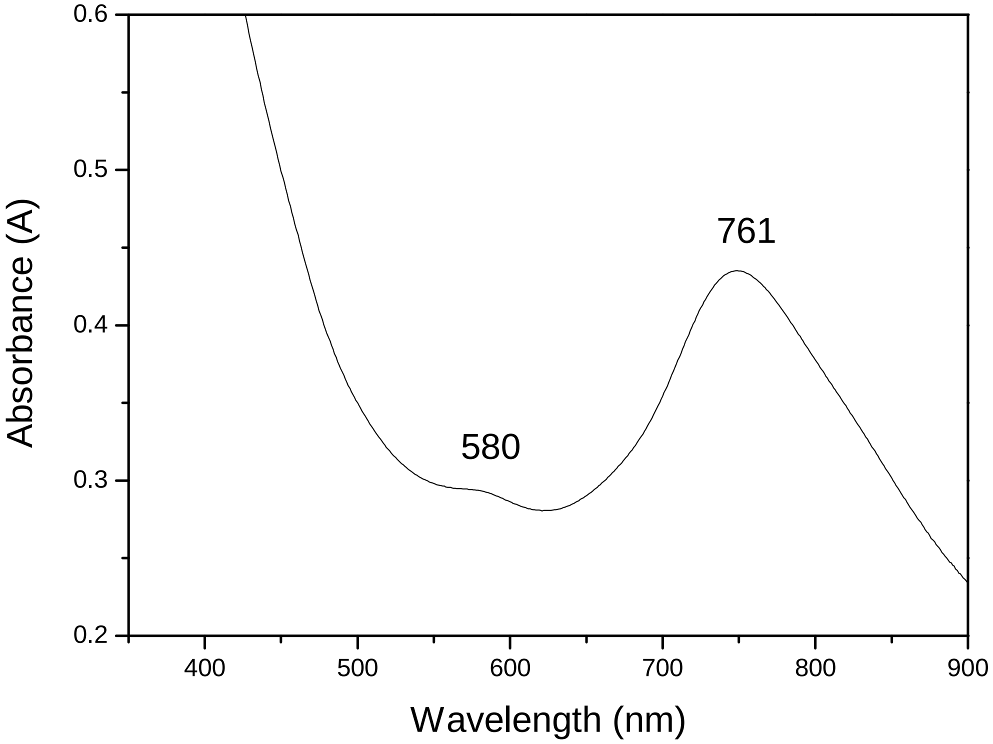

Figure 3.3 **A representative visible spectrum of the PEDOT samples** (*IL-B*, after 3 days). Path length: 1cm.

To study the influence of EDOT concentration on morphology of the final nanospheres, the mass of EDOT in RTIL was varied from 30.0 mg to 3.0 mg for four samples (Table 3.1). Scanning electron microscopic (SEM) and transmission electron microscopic (TEM) studies were performed to observe the morphology on the four samples. In the SEM and TEM images, it was observed that the morphologies of the final nanospheres depend strongly on the EDOT concentration in RTIL. For sample *IL-A* with the highest EDOT concentration in the series, the size and morphology before and after washing with methanol were obtained (Figure 3.4a~f). The methanol quenching process consists of adding 1 ml of methanol to the reaction mixture (~10 ml), and a drop of the solution was withdrawn for spin coating, followed by morphology observation. The SEM images of *IL-A* (Figure 3.4a, b) show a bimodal size distribution, 15-20nm and 40-50nm. With methanol washing, the RTIL and its contents were washed out from the core of nanospheres and the PEDOT shell crashed in to form a nano-disk (Figure 3.4c, d). In addition, the diameter of the nanodisks formed after washing ranges from 80-150 nm, much larger, as expected, than diameter of original core-shell nanospheres. The TEM image (Figure 3.4e) confirms the bimodal size distribution of the nanospheres. The high-magnification TEM image (Figure 3.4f) clearly shows that the spheres contain more than one interior chamber. The "multi-chamber" nature of the nanospheres in sample *IL-A* resulted from the high EDOT concentrations in RTIL. The influence of the concentration of EDOT in RTIL on the morphology of final nanospheres was investigated; a variation of distribution in chamber was observed. Similar to *IL-A*, multi-chamber core morphologies were also observed in TEM images of *IL-C* (Figure 3.5e, f) and *IL-D* (Figure 3.6c, d) samples. The distribution of chamber in the core varied for different spheres, as shown in the high magnification scale TEM image for *IL-D* (Figure 3.6d). Figure 3.5a~d indicates that the size and morphology resulting from reaction for 6 days is similar to those from 72 hours. Figure 3.6a, b show the morphologies of *IL-D* before and after methanol washing. Nano-disks were observed after washing (Figure 3.6b). Sample *IL-B* was prepared using the same conditions as for *IL-D* except the EDOT concentration is higher (15 mg vs. 3 mg in 100 mg) (Table 3.1). Before the methanol washing process, narrow dispersed spheres with an average diameter at around 75 nm were observed for *IL-B* (SEM image, Figure 3.7a). Single-chamber core-shell nanospheres were obtained as indicated by TEM image (Figure 3.7c). This morphology is desirable for the controlled release applications. The SEM evidence of the formation of the PEDOT nanospheres is also provided by the transformation to nano-disks on methanol quenching of the suspension (Figure 3.7b). The PEDOT shell is permeable to methanol, allowing methanol to remove the core content. Thus, the core-shell nanospheres collapsed and formed nano-disks. The observed morphological difference due to the variation of EDOT concentration in RTIL indicates the importance of EDOT concentration for the core morphology. In a multi-chamber nanosphere, PEDOT not only formed the shell, but penetrated into the RTIL core, and separated the core into several smaller chambers filled with RTIL. Even though the multi-chamber spheres can also be utilized for a nano-encapsulation, single-chamber sphere with a thin PEDOT layer is preferred for the efficient cargo capacity. Too high or too low concentration of EDOT monomer is not preferred for the preparation of single-chamber nanosphere with a suitable thickness of the particle shell. From SEM and TEM results, the optimum reaction conditions of single-chamber PEDOT nanospheres are those for *IL-B*, Table 3.1. It is noteworthy that with stirring in preparation of sample *IL-B*, low population of PEDOT nanospheres with abundance of needles with average length of 150 nm were produced (Figure 3.7d).

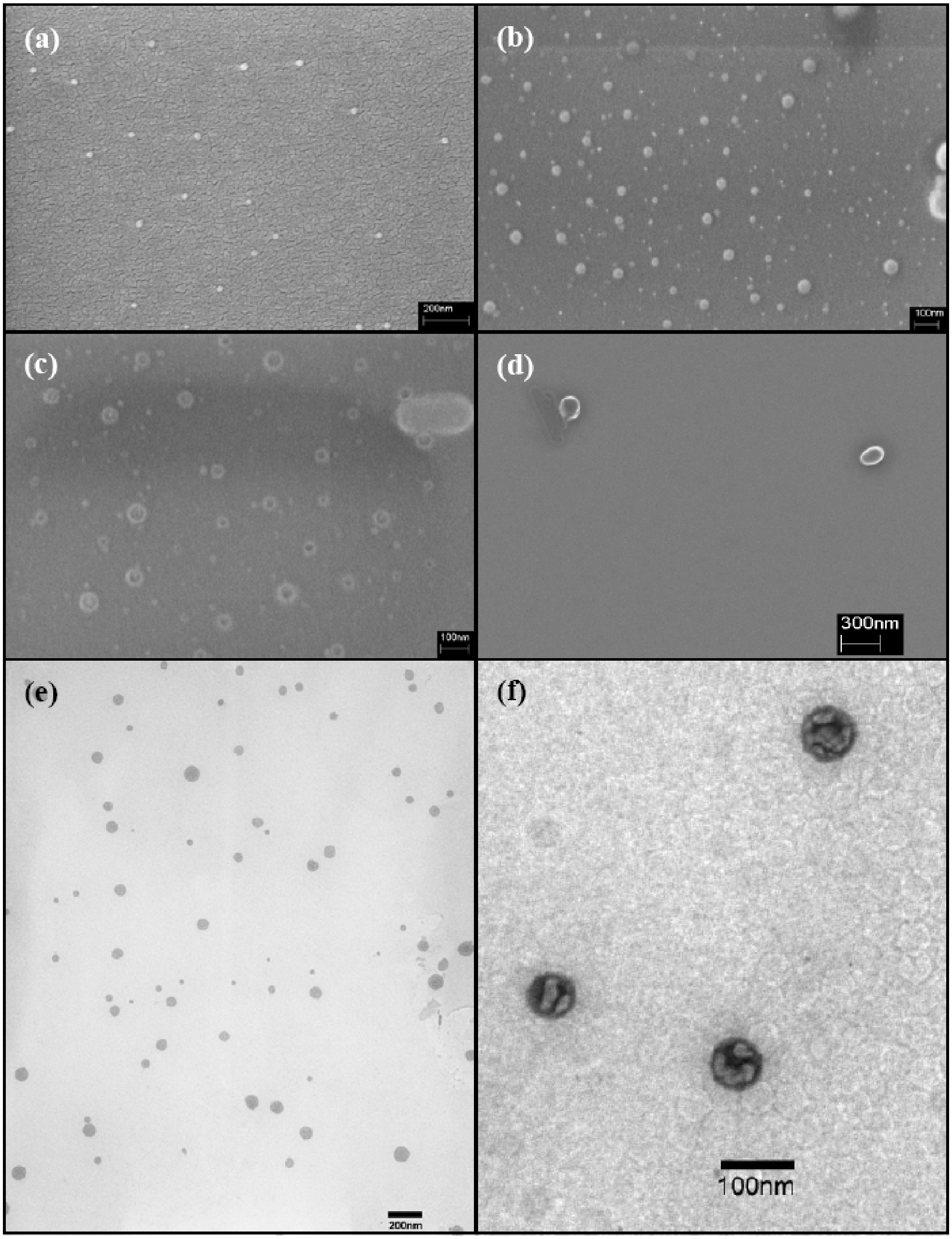

Figure 3.4 **Morphology of sample *IL-A*.** SEM images of *IL-A* 72 hours reaction time. (a, b) SEM images of *IL-A* without methanol wash. (c, d) SEM image of *IL-A* with methanol quench. (e) TEM image of *IL-A*. (f) TEM image in high-magnification.

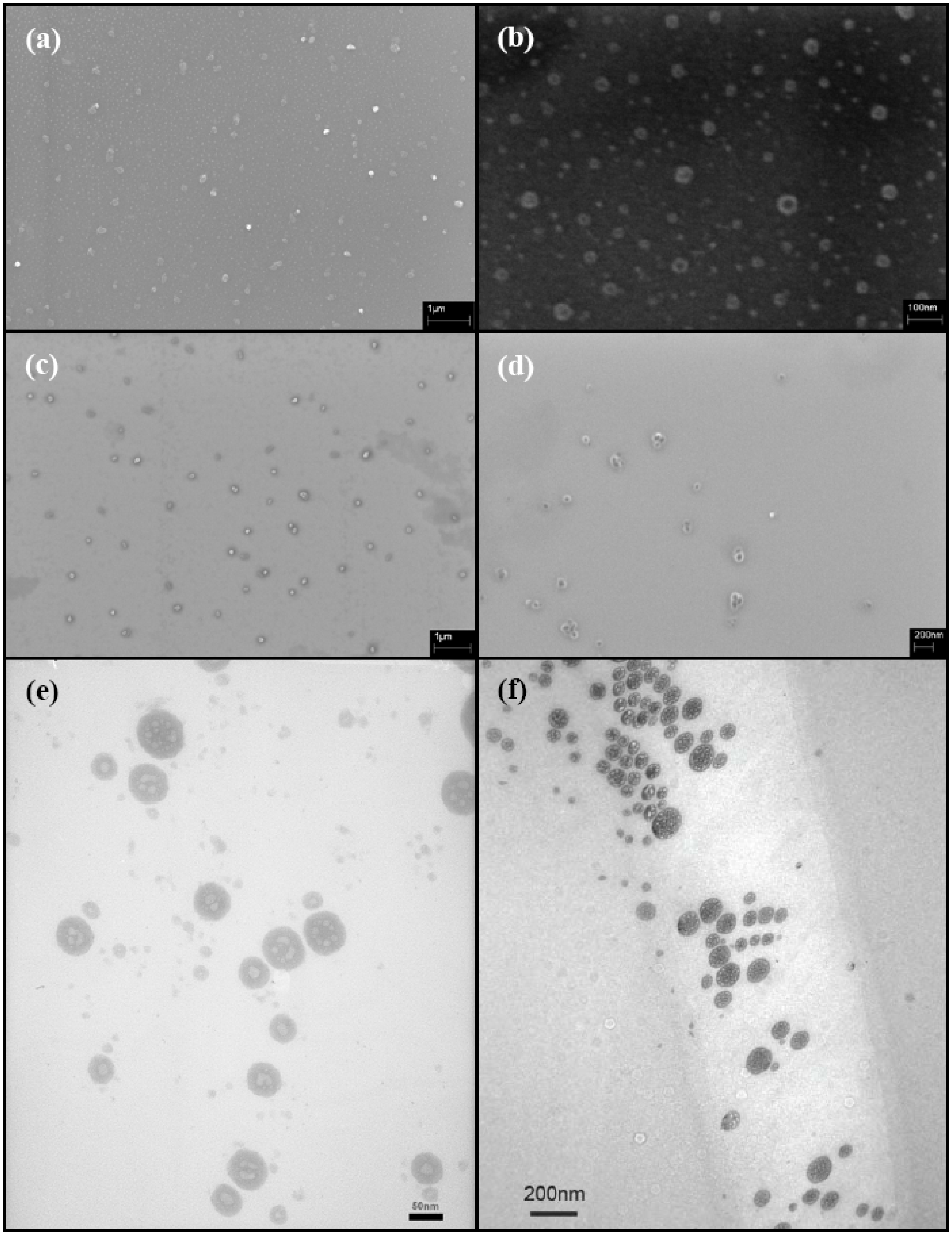

Figure 3.5 **Morphology of sample *IL-C*.** SEM images of *IL-C* 72 hours reaction time (a) without and (b) with methanol quench. SEM images of *IL-C* collected after 6 days (c) without and (d) with methanol quench. TEM images of *IL-C* collected after (e) 72 hours and (f) 6 days.

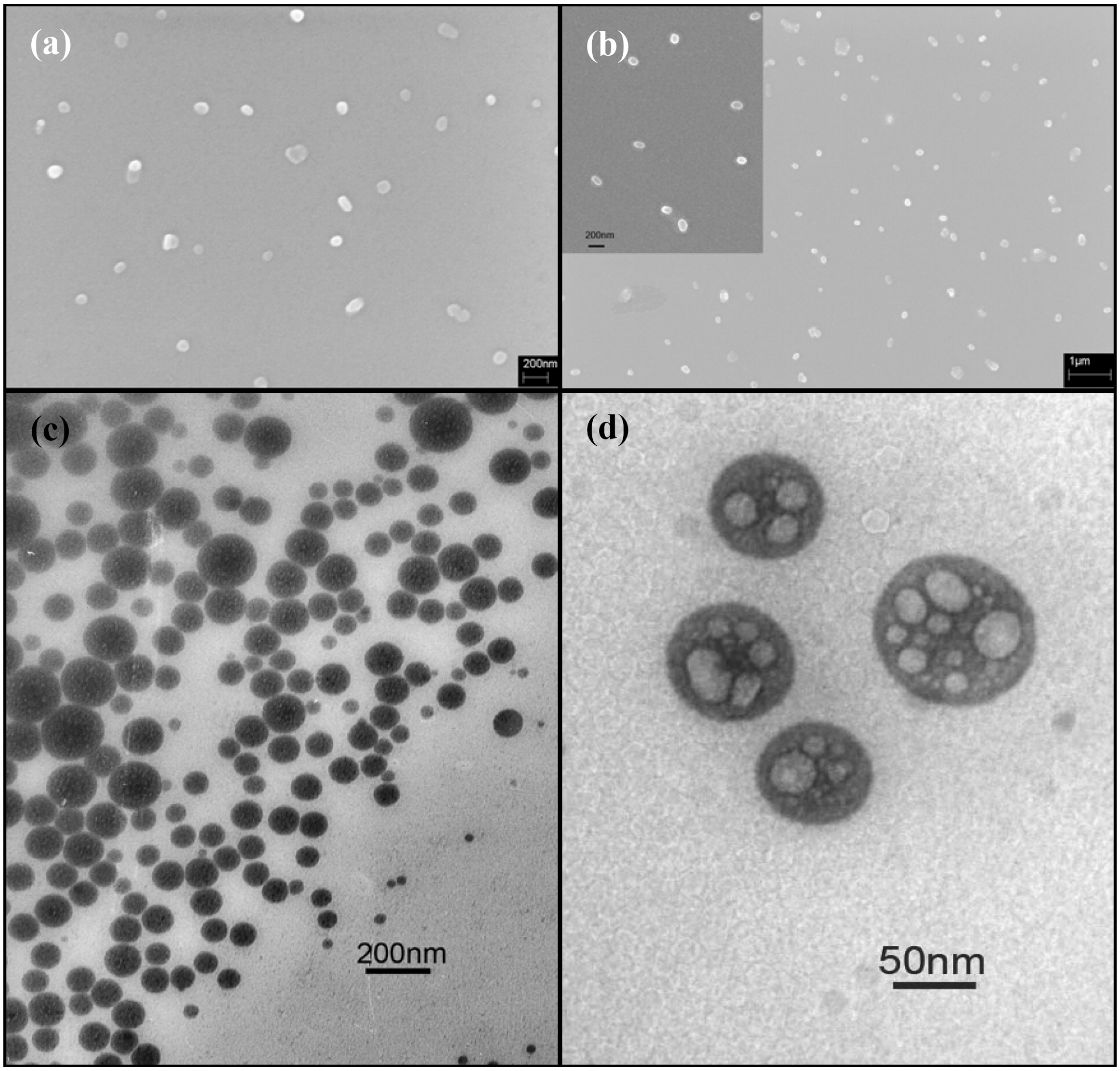

Figure 3.6 **Morphology of sample *IL-D*.** SEM images of *IL-D* 72 hours reaction time (a) without and (b) with methanol quench. TEM images of *IL-D* collected after 72 hours in (c) low-magnification and (d) high-magnification.

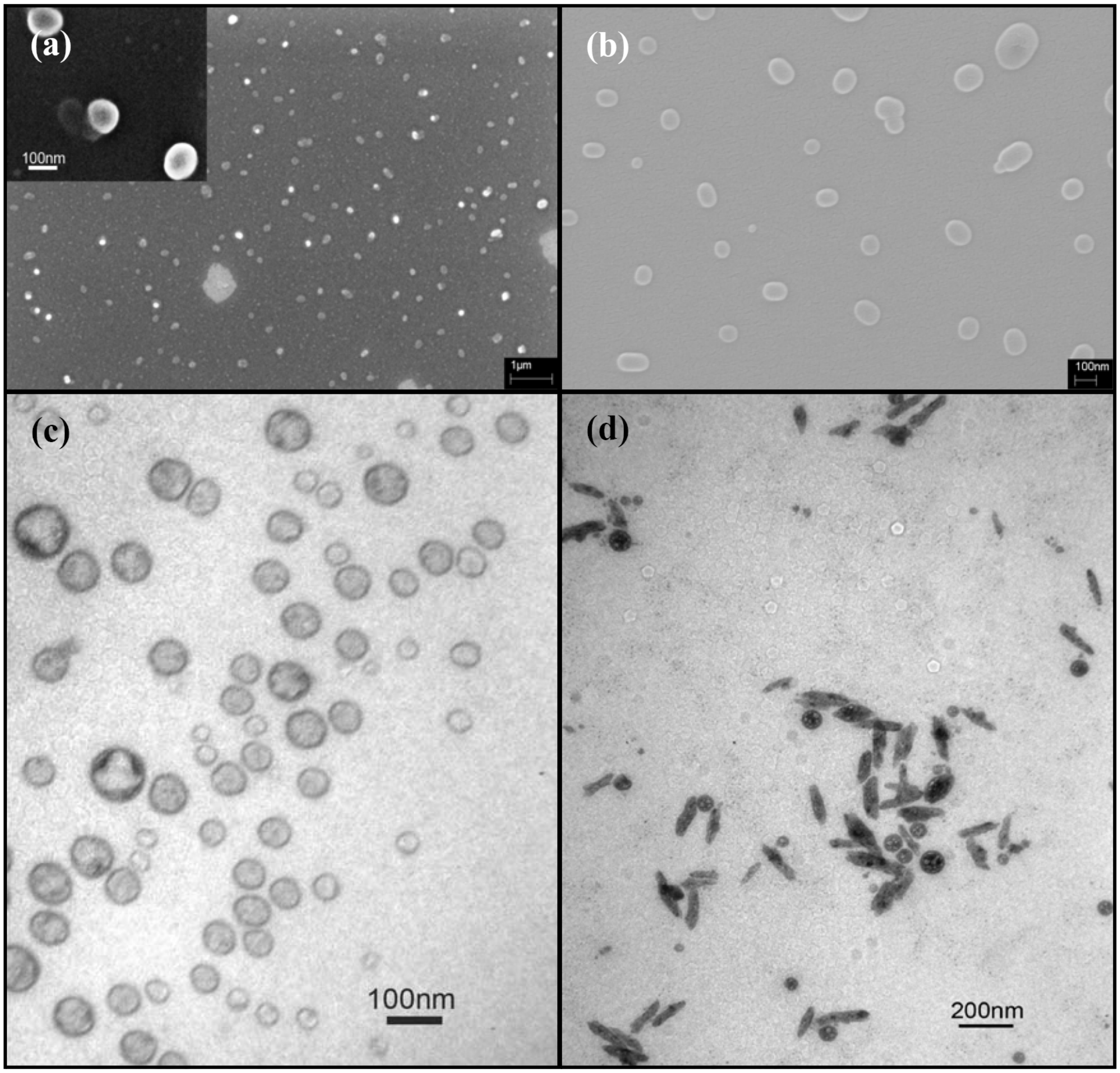

Figure 3.7 **Morphology of sample *IL-B*.** SEM images of *IL-B* at two reaction times (a) 72 hours and (b) 6 days with methanol quench. TEM images of *IL-B* collected after 6 days (c) without stirring and (d) with continuous stirring during the reaction.

Our preliminary studies indicate that the EDOT concentration played an important role in the formation of the core. The result shows the reaction condition of *IL-B* is suitable for the production of single-chamber PEDOT nanospheres of an average diameter at 75 nm with narrow size distribution. The size for PEDOT nanospheres can be tuned through changing the bmimPF$_6$-to-“TX-100” molar ratio, *R*. Reaction conditions of *IL-B* were used to synthesize PEDOT core-shell nanospheres with different diameter through changing *R* ratios. A series of experiment was carried out for PEDOT nanospheres with *R* ratios, 0.17 (Sample *IL-B*), 0.24 (*IL-E*), 0.32 (*IL-F*) and 0.41 (*IL-G*) in Table 3.2. The size and morphology of PEDOT were established by SEM observation. As *R* increased, the average diameter of single-chamber PEDOT nanospheres increases from 75 to 400 nm in this series (Figure 3.8). For *IL-G*, the conductivity of a single sphere was measured by conductive-AFM. I-V curve indicates that the conductivity of PEDOT core-shell nanospheres at 3.2V was at least 2 mA (Figure 3.9).

A distinctive characteristic of conducting polymers is the substantial volume changes accompanied the change of doped states processes either electrochemically or chemically as shown in scheme 2.1.[6] A review summarizing the mechanism and application of this unique property of conducting polymers is available.[10] In this study, substantial volume changes were also observed in the PEDOT nanospheres which hold significant potentials for controlled release. The volume or size changes were accomplished via a doped-dedoped process conducted by tuning the pH value of a prepared sample by adding small amount of an ammonia solution. Sample *IL-G* was selected for the volume change study. After 72 hours, *IL-G* was collected and its pH value was determined to be 4. The average diameter of the *IL-G* nanospheres is 400 nm (Figure 3.8d). Through addition of ammonia solution, the pH value of *IL-G* was adjusted from 4 to 12 with steps of 1 pH unit. Samples in different pH environment were collected for the morphology study by SEM. Figure 3.10 shows SEM images for the samples with a pH value from 5 to 12. Interesting size and morphology changes were readily observed. With pH value changing from 4 to 6, the diameter of the nanospheres reduced drastically

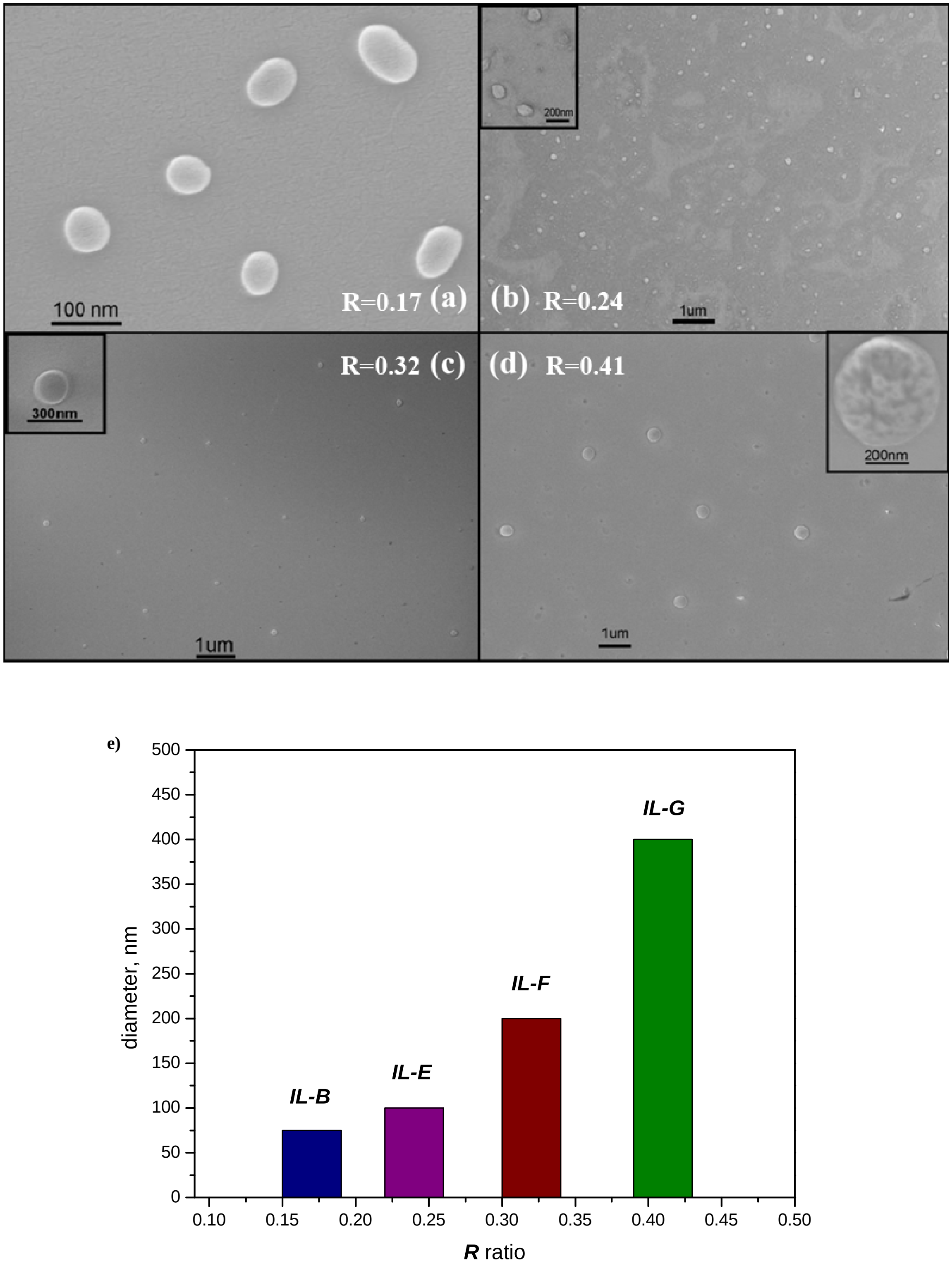

Figure 3.8 **SEM images of samples in different *R* ratio.** (a) *IL-B* (*R*=0.17), (b) *IL-E* (*R*=0.24), (c) *IL-F* (*R*=0.32) and (d) *IL-G* (*R*=0.41). (e) Size tunability base on (bmimPF_6)/TX-100 ratio.

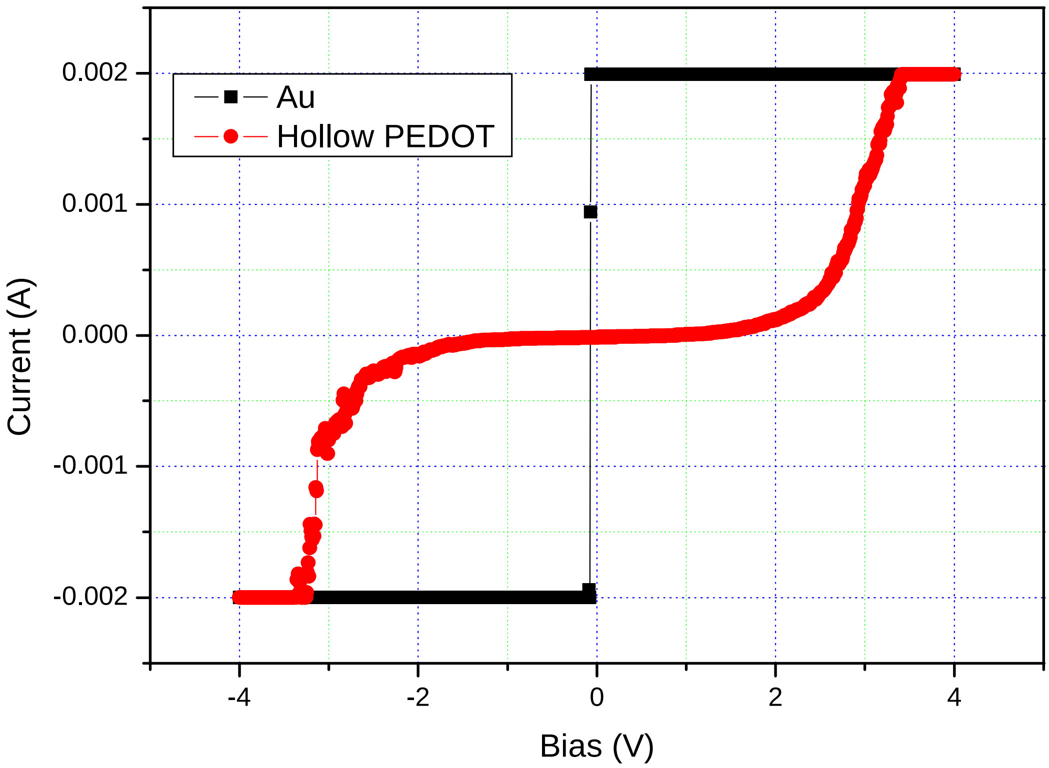

***Figure 3.9* Current vs. bias voltage for Au surface and PEDOT core-shell nanospheres of *IL-G*.**

from 400 to 100 nm (Figure 3.8d and Figure 3.10a, b). Small diameter difference was observed for samples from pH=6 and 7 (Figure 3.10b, c). From pH=7 to pH=9, the diameter of nanospheres increased from 100 to 350 nm (Figure 3.10c~e). The diameter changes are due to the removal of H^+ from the polymer chain by ammonia. From pH=10 to pH=12, a transition from sphere to rod was also observed (Figure 3.10f~h). The length and width of the nanorods are 350x250, 400x200 and 450x100 nm for pH=10, 11 and 12 respectively (Figure 3.10). Figure 3.11 represents the high-magnification SEM images of the nanoparticles, showing the evolution of size and aspect ratio due to pH changes.

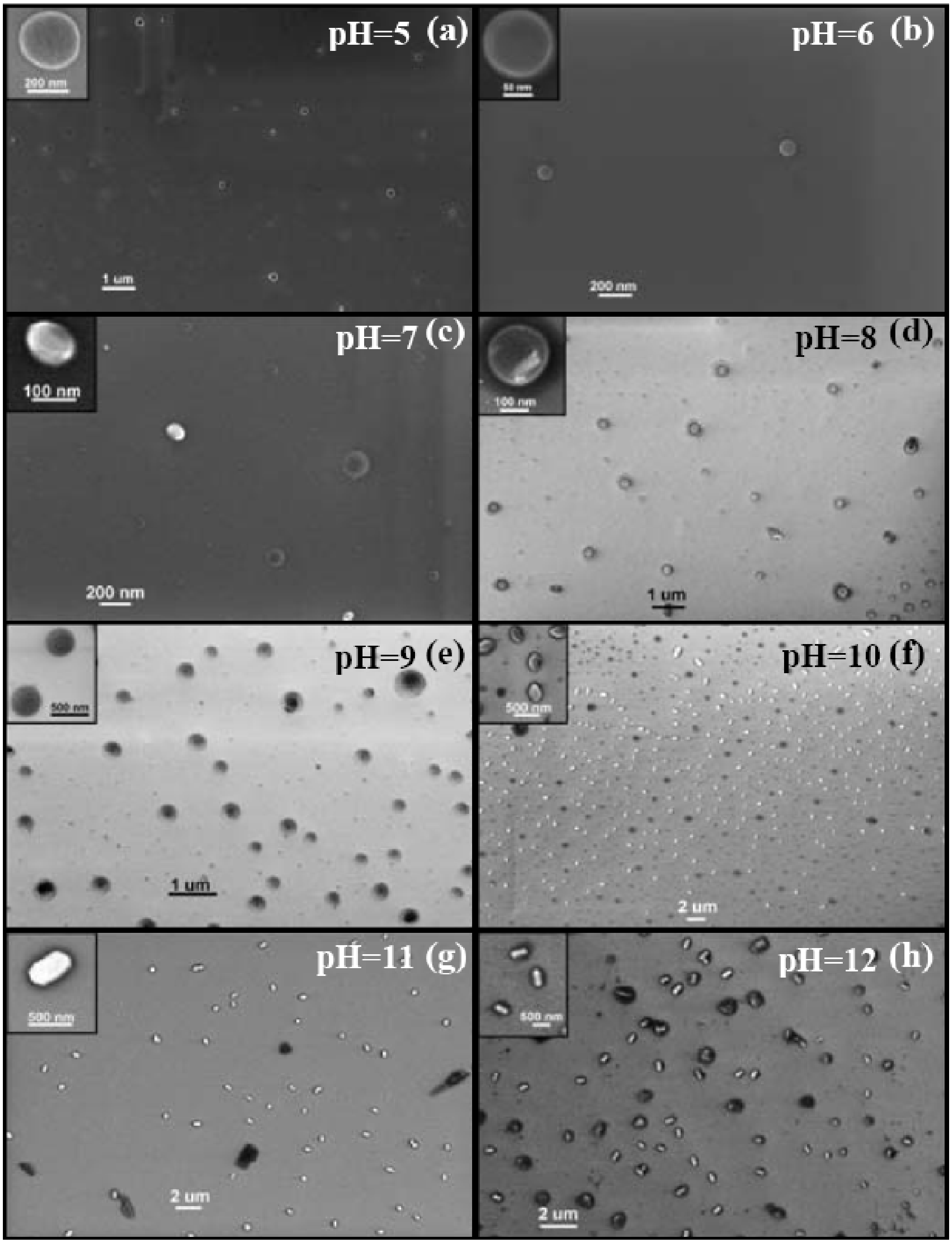

***Figure 3.10* SEM images of sample *IL-G* (*R*=0.41)**. pH= (a) 5, (b) 6, (c) 7, (d) 8, (e) 9, (f) 10, (g) 11 and (h) 12.

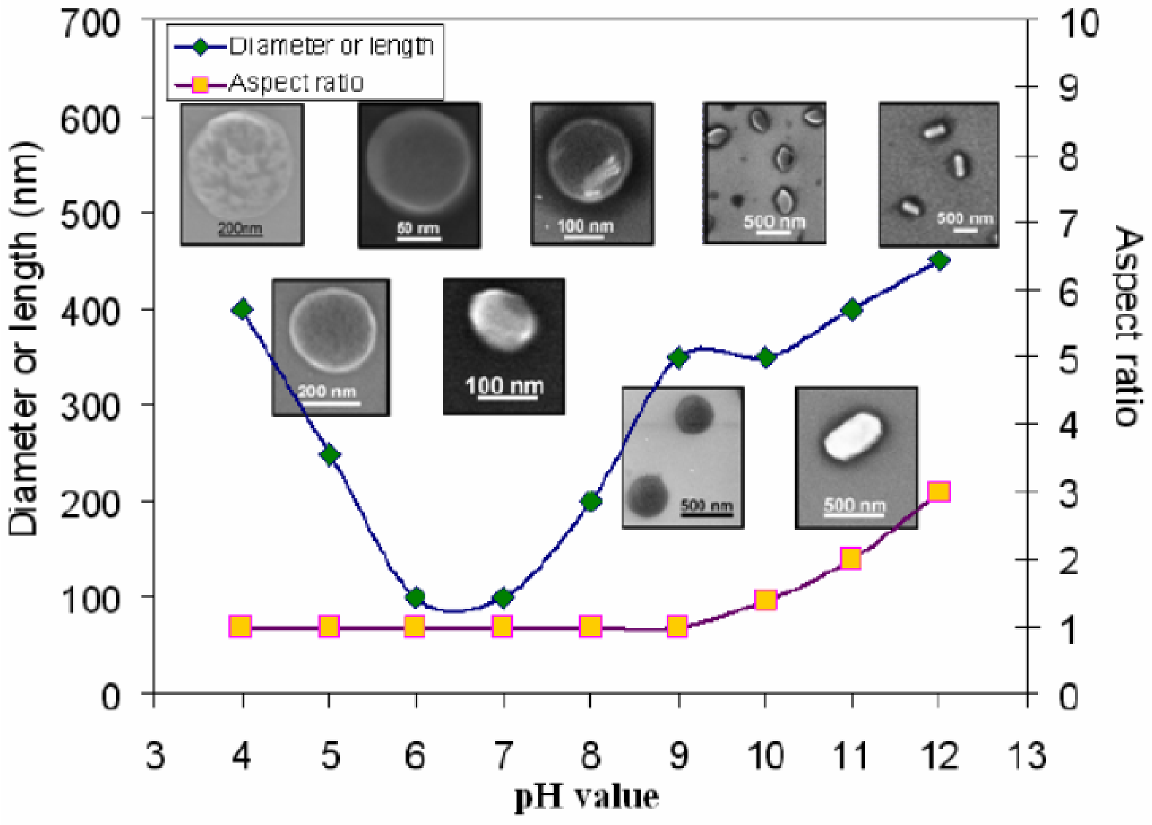

Figure 3.11 **Volume and morphology change of sample *IL-G* with the pH tuning.** The SEM image above each pH value shows the size and morphology of the nano-encapsulates respectively. A clear aspect ratio change with the pH value is also observed from pH=4 to pH=12.

Two processes of volume change (shrink and expansion) in *IL-G* were also observed. In this study, a more complicated trend in size changes occurred during the dedoping process, because both the sulfate (smaller in size) and hexafluorophosphate (large in size) anions serve as the counter ions to PEDOT (Scheme 3.3). In the doped state (PEDOT as synthesized), equivalent counter ions (small sulfate and large hexafluorophosphate anions) are present in the matrix of PEDOT nanospheres to maintain charge balance of the system. After stimulation by tuning pH value to 7, the backbone of PEDOT becomes less positively charged and small sulfate ions migrate out of matrix of PEDOT, causing the volume shrinking (Scheme 3.3, “dedoped state I”). When pH above 7, PEDOT changes to neutral, but large hexafluorophosphate ions cannot move out. Thus, the cations in solution diffused into the sphere of PEDOT, inducing the volume expanding (Scheme 3.3, “dedoped state II”). In the dedoping process (pH=10 to pH=12), the backbone of PEDOT became mostly neutral. The PEDOT packed together with lower curvature because of its chain rigidity at low doping. The nanostructures transformed from nanospheres to nanorods with different aspect ratios (Figure 3.10 and Figure 3.11).

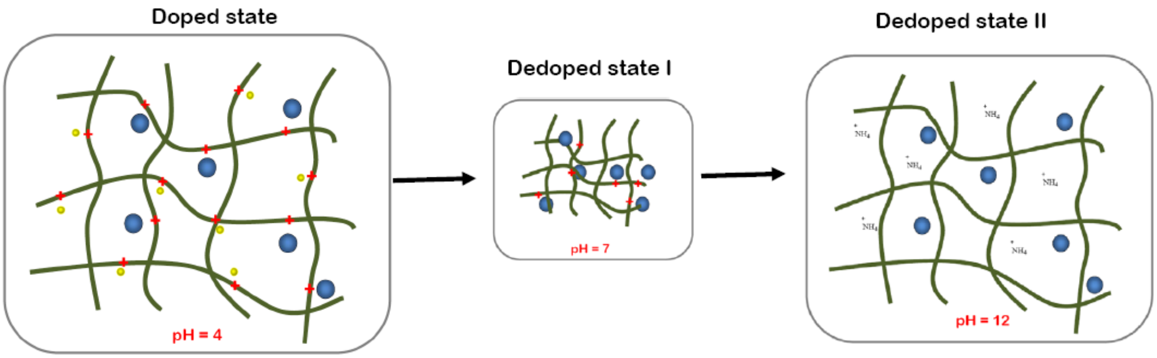

Scheme 3.3 Mechanism of volume change in conducting polymer through dedoping process from pH change. 🔵 : PF_6 anions 🟡 : sulfate anions

From visible and near IR absorption (Figure 3.12), the dedoping process of PEDOT nanospheres (*IL-G*) in different pH value was observed. The highly doped PEDOT formation peak of 761 nm was absorbed in pH of 4 (PEDOT as synthesized). As pH value increases, the PEDOT absorbance peak of 761 nm decreases. At pH above 9, the PEDOT peak of 761 nm disappears, likely due to the effect of removing proton from the conjugate system. At pH above 10, new peaks of 1039 nm and 1227 nm appear, indicating new morphology formation. Similar absorption peaks were reported in literatures. However, the nature of new peaks remains unclear.[46]

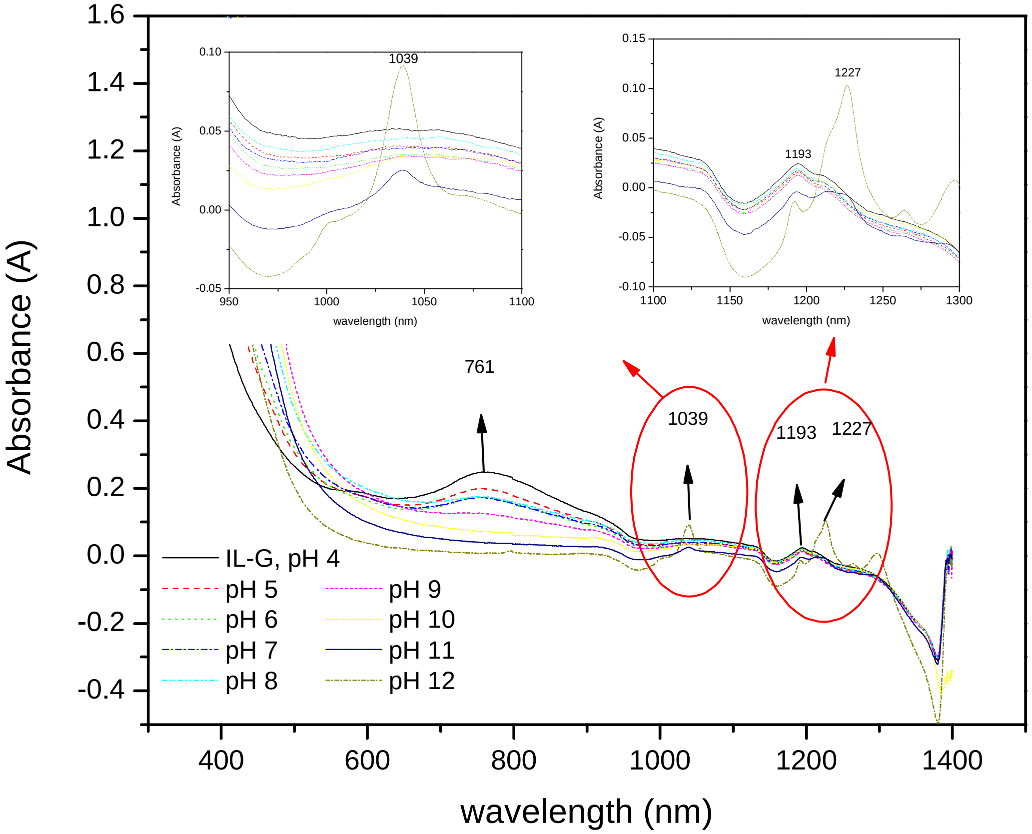

Figure 3.12 **Visible and near IR spectrum of IL-G in different pH values of 4 to 12.**

The morphology change of the nanostructures to an anisotropic form with the dedoping process indicated that a more ordered molecular arrangement was developed during the dedoping process (as shown in Figure 3.10f~h and Figure 3.11). The electron diffraction study was conducted on individual nanostructures of the sample in pH=7, 10 and 12, respectively. Figure 3.13 shows electron diffraction of the sample of pH=7 does not have any ordered pattern. A different pattern with diffraction arches was clearly observed in the electron diffraction image of the sample of pH=10, Figure 3.13b, suggesting a highly ordered structure, developing during the dedoping process by ammonia. Diffraction spots were also observed in the pattern of the sample of pH=12, Figure 3.13d. Due to dedoping process, backbone of PEDOT carried increasingly less positive charge. Therefore, the better packing and rigid structure of PEDOT cause elongation and highly order molecular arrangement; the details of the lattice structure of the highly ordered structure remains unclear. Figure 3.13c shows the high resolution transmission electron microscopic, HRTEM, image of part of an individual nano-rod (pH=12).

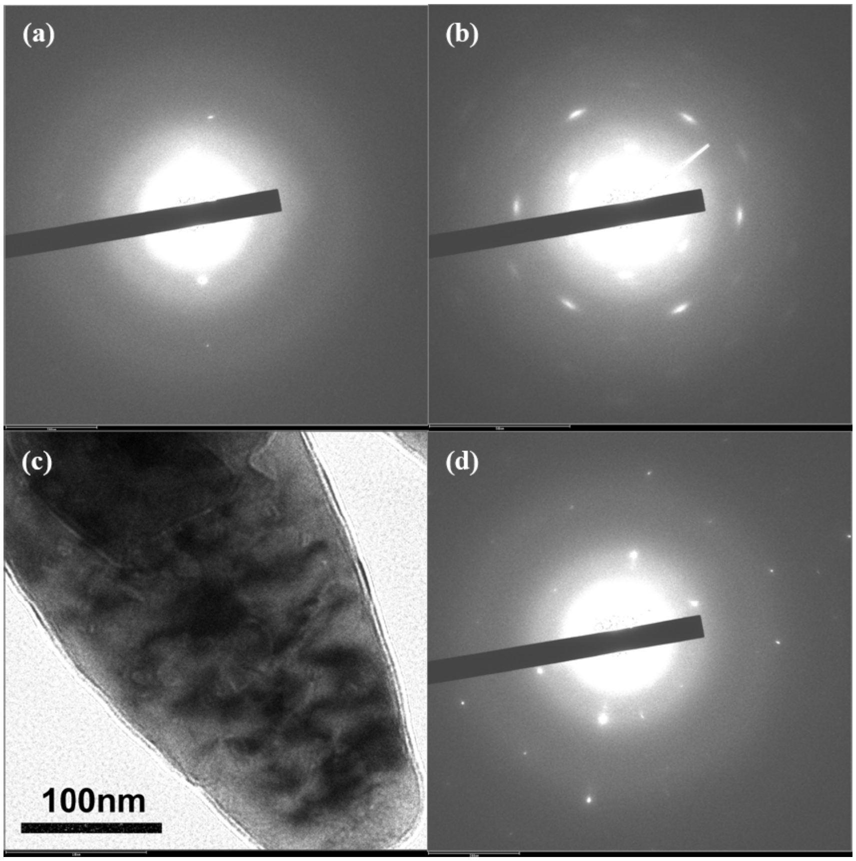

Figure 3.13 **Electron diffraction images of samples of different pH values**. (a) pH=7, (b) pH=10 and (d) pH=12. (c) High resolution TEM image of the sample of pH=12.

To establish the controlled release capability of the system described in scheme 3.4, two model compounds, dipyridamole and carboxylated curcumin were selected as the cargos. As depicted in scheme 3.4a, the uncharged dipyridamole was first dissolved in bmimPF$_6$ in the initial preparation step. The controlled release from the core was through the volume change triggered by the pH tuning. For release from nanosphere surface, anionic carboxylated curcumin dissolved in the aqueous phase (scheme 3.4b) migrated to the surface of the sphere. The controlled releases for both were monitored by UV/Vis absorption analysis. Dipyridamole has a strong ultraviolet absorbance band at around 420 nm. This peak was used to follow its release from the nanospheres. The experimental conditions of *IL-G* were chosen except 28 mg of dipyridamole was dissolved in bmimPF$_6$. Due to the hydrophobic nature of the drug, most dipyridamole molecules remained inside the RTIL micelles during the polymerization process. Product was collected after 3 days. UV/Vis spectrum of the as synthesized sample did not show the drug absorbance peak at 420nm, blue line in Figure 3.14a. The absence of this peak is due to the shielding of the UV irradiation by the highly absorbing PEDOT shell. After tuning the pH value of the sample to 7, a drug absorbance peak was clearly observed in the UV/Vis spectrum, red line in Figure 3.14a, indicating the controlled release. For carboxylated curcumin, the reaction condition was kept as in sample *IL-G,* except 4 mg of curcumin and 0.56 g of tetrahydrofuran, for better solubility of curcumin, were added into the aqueous phase. After 3 days, the product sample was collected and dialyzed in deionized water for 2 days to remove the free curcumin compounds in the aqueous phase. The pH value of the dialyzed sample stayed unchanged. Curcumin compounds conjugated with the PEDOT shell still remained on the shell. An absorbance peak at ~420 nm, blue line in Figure

3.14b, indicated the incorporation of curcumin into the nano-shell of PEDOT. After the first UV/Vis analysis, pH value of the solution was tuned to 7 by ammonium solution. Another dialysis was conducted for 2 days followed by a second UV-Vis absorbance study. The lack of a characteristic peak, red line in Figure 3.14b, suggested that most of the curcumin compounds had been released by pH tuning. In order to determine the percentage of dipyridamole molecules released from inside of nanospheres after the shrinkage of the hollow sphere at pH of 7, five different standard concentrations of dipyridamole were made in DI water for calibration. Calibration curve (absorbance at 420 nm vs. concentration of dipyridamole) was plotted in Figure 3.15, and a calibration equation was obtained. The concentration of released dipyridamole was found to be 2.10 mg/mL. Comparing concentration of loaded (beginning, 3.44 mg/mL) and released (calculated, 2.10 mg/mL) dipyridamole, about 61% of dipyridamole was released from the core of nano-sphere.

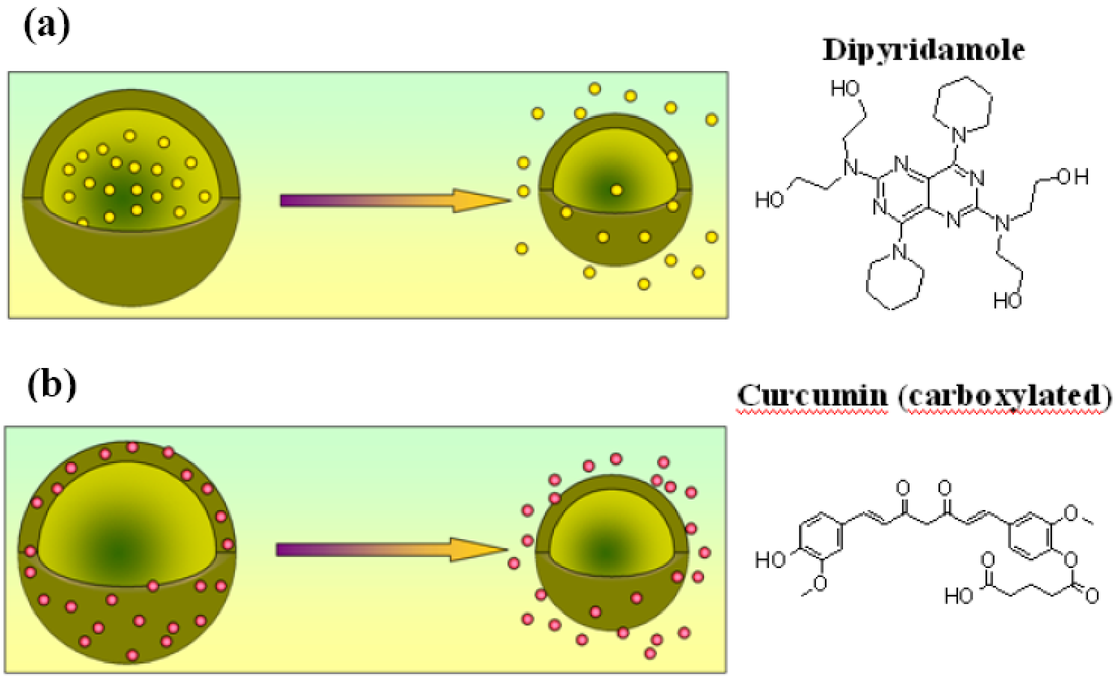

Scheme 3.4 Schematic for controlled release from polymeric hollow nanospheres. (a) The green hollow nanosphere represents a polymeric encapsulated synthesized through Micro-interfacial polymerization. ● is a hydrophobic active species, dipyridamole in this study, dissolved in room-temperature ionic liquid (RTIL). The controlled release was through the polymer volume change triggered by pH tuning. (b) ● is a hydrophilic active species, carboxylated curcumin in this study, also functions as the dopant of the polymer shell. The active species is released through t pH tuning. Chemical structures of dipyridamole and carboxylated curcumin are shown in the scheme.

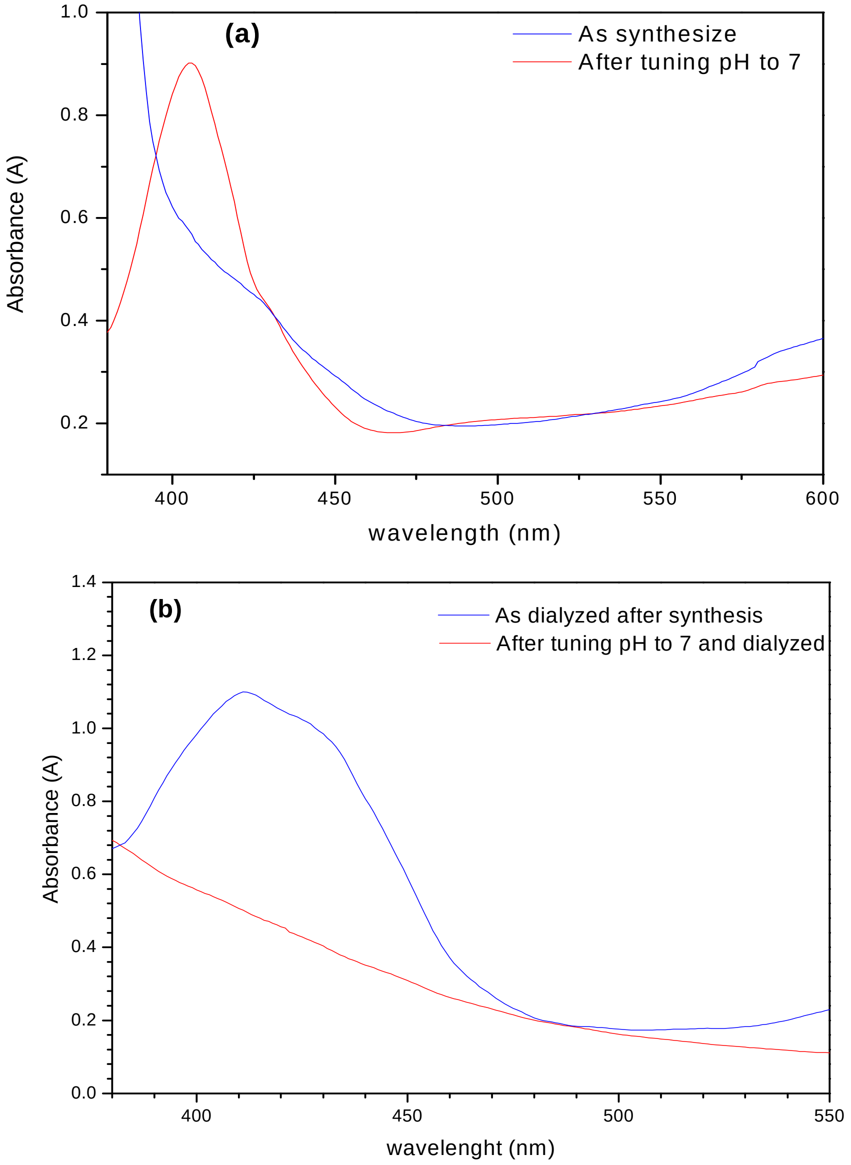

Figure 3.14 **UV/Vis absorbance spectra for the controlled release study.** The two systems as described in scheme 2.3. Path length: 1cm. Blue line reference: IL-G. Red line reference: IL-G at pH of 7. (a) Dipyridamole as cargo. Blue line without cargo peak indicates cargos were encapsulated in PEDOT nanospheres. After tuning pH to 7, absorbance peak (Red line) indicates the cargos released from PEDOT nanospheres. (b) Using carboxylated curcumin as cargo on the surface of PEDOT shell. Absorbance peak (Blue line) of curcumin molecules on the PEDOT nano-shell was observed in the dialyzed system. After pH tuning to 7 and another dialysis, the disappearance of the absorbance peak (Red line) indicates that most of cargos, curcumin, have been released during the dedoping process.

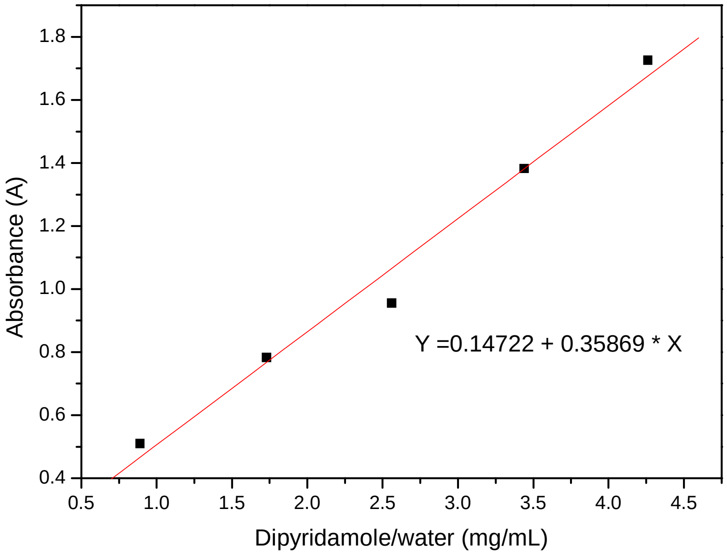

Figure 3.15 **Calibration Curve: absorbance vs. concentration of dipyridamole in water**

3.1.4 Conclusion

In summary, a promising conducting polymer nanosphere controlled release system was readily prepared via an "*interfacial Polymerization*" process by using room temperature ionic liquid in water micelles as a soft template. Multi-chamber and single-chamber core-shell nanospheres were obtained by adjusting the monomer, EDOT, concentration in RTIL. The interior RTIL molecules can be readily removed by washing with methanol and nano-disk morphology was obtained. By tuning the RTIL-to-surfactant molar ratio, *R*, the size of micelles can be adjusted in the range of 75 to 400 nm. The diameter of the nanospheres was further adjusted by a volume change of conducting polymer with pH tuning. Two controlled release strategies were established by using dipyridamole and carboxylated curcumin as the cargo. UV/Vis study confirmed the controlled release based the size change of the nanospheres. Nanorod morphology and a highly ordered molecular arrangement were developed when the pH value was tuned to higher than 10. The findings in this study can contribute to the understanding to a broad range of research areas, including conducting polymer, nanoscience and controlled release.

3.2 Polarization behavior of core-shell nanosphere of conducting polymer, polyanline, matrix with high-*k* nanoparticals embedded – (in collaboration with Dr. Kai Su, Ref. 47)[47]

3.2.1 Polarization behavior

A new core-shell nanostructure with high-*k* nanoparticals embedded in the core was discovered. Procedures for the preparation of nanopheres with cores of polyaniline (PANI) / strontium titanate (STO) composite have been documented in details (Ref. 47). Procedures of samples preparation for KPFM investigation as follows: A drop of PANI as synthesized was spin-casted on an Au surface (3000 rpm). Then, the sample was rinsed two times by deionized water. The doped core-shell composite powders with STO to PANI weight ratio of 8/1 were dispersed in deionized water (0.1 mg/mL) by using ultrasonic for 10 min. A drop suspension was directly deposited on an Au surface. The Au surfaces were prepared by sputtering on silicon wafers.

Scheme 3.5 shows structure of the stuffed sphere morphology of nano-composite with STO nanocrystals in PANI matrix (dark gray), an embedded structure of STO/PANI nanocomposites. The morphology of STO/PANI nanocomposites with weight ratio of 2/1 was observed by TEM (Figure 3.16). The nanocomposites were in spherical form smaller than 100 nm with a few large ones at the level of 180 nm. This spherical form is composed of 5 nm STO nanocrystals embedded in PANI matrix. The enlarged TEM image (inset of Figure 3.16) shows STO nanocrystals embedded in PANI matrix. The electric polarization of STO/PANI composites was observed in KPFM measurement with a delta height ΔZ=50 nm (the distance between the tip and the sample surface). The PANI and STO weigh ratio in the composite is 1 to 8. Figure 3.17 shows in (a, f) topography images of PANI and composite having an average height of 80 and 130 nm respectively. The topographic imaging was followed by applying various DC bias (+1V and -1V) on the same scanned areas to induce electric polarization and map the resulting potential profile corresponding to particles with induced dipole. In order to remove the already existing surface charge and to observe only the induced polarization, an AFM scan with zero bias was performed first on the same region using a contact mode with a grounded tip. We, then, applied positive and negative DC bias at different levels from the gold substrate to induce polarization. The surface potential image (Figure 3.17b) at 0 V DC bias shows clearly that there is no significant polarization on the PANI sample, but Figure 3.17g shows average positive (~ 20 mV) polarization at 0 V DC bias on the surface of the STO/PANI composites. One possibility of this positive polarization of the composite at no bias voltage is due to the influence of PANI matrix of highly positive charge. STO nanoparticles can be polarized under the strong positive field of the matrix. After applying DC bias to +1 V on the surface, the positive polarization of both PANI (Figure 3.17c) and composites (Figure 3.17h) increased, to average of ~20 mV and ~100 mV respectively, indicating a synergistic polarization effect. When a negative bias of -1 V DC was applied, a nearly inverted image of PANI was observed (Figure 3.17d vs. Figure 3.17c), indicating clearly that the polarization direction of PANI was reversed by the external electrical field. However, the SP image of the composite (Figure 3.17i) retained some positive polarization but at a much lower level than the case without bias (Figure 3.17g). Thus, a -1 V bias was not sufficiently high to completely reverse the direction of SP (20 mV) originally existed in the composite.

With the coercive bias of STO (~3 V), the negative bias (-1 V) is not sufficient to invert the polarization of STO. PANI as a good electronic conductor was readily polarized at -1 V. Figure 3.18 shows the comparison of PANI at 1 V (a) and STO/PANI composites at 0 V (b) and 1 V (c). Polarization of the composites at 1 V bias is 100 mV, a much higher value than that for PANI of 20 mV at the same bias. Thus, at a bias much lower than the STO coercive voltage of 3 V, the composite show large polarization. It is concluded that this novel core-shell structure combines atomic and electronic polarizations in one element of nanometer scale and exhibits synergistic electronic polarization properties.

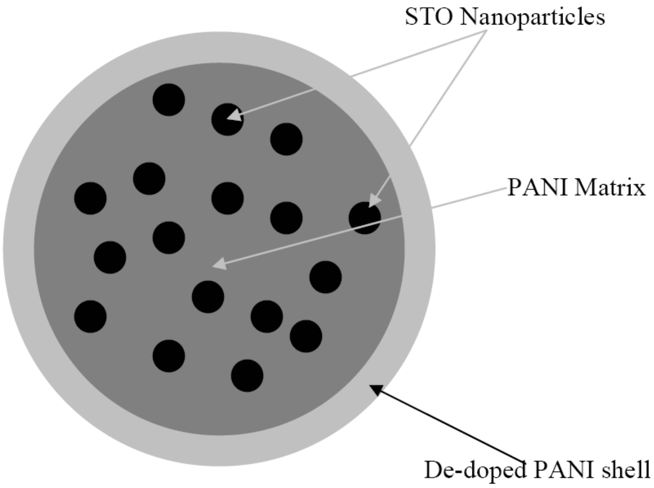

Scheme 3.5 Schematic structure of the nano-composite of high-*k* STO nanoparticles in conductive polymer PANI matrix.

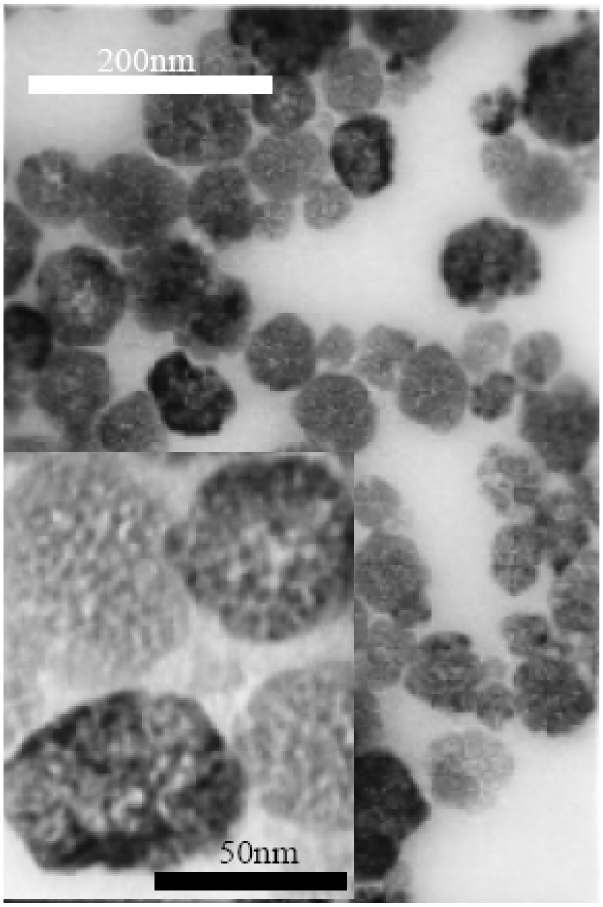

Figure 3.16 **TEM images of STO/PANI nanocomposites with weight ratio of 2/1.**

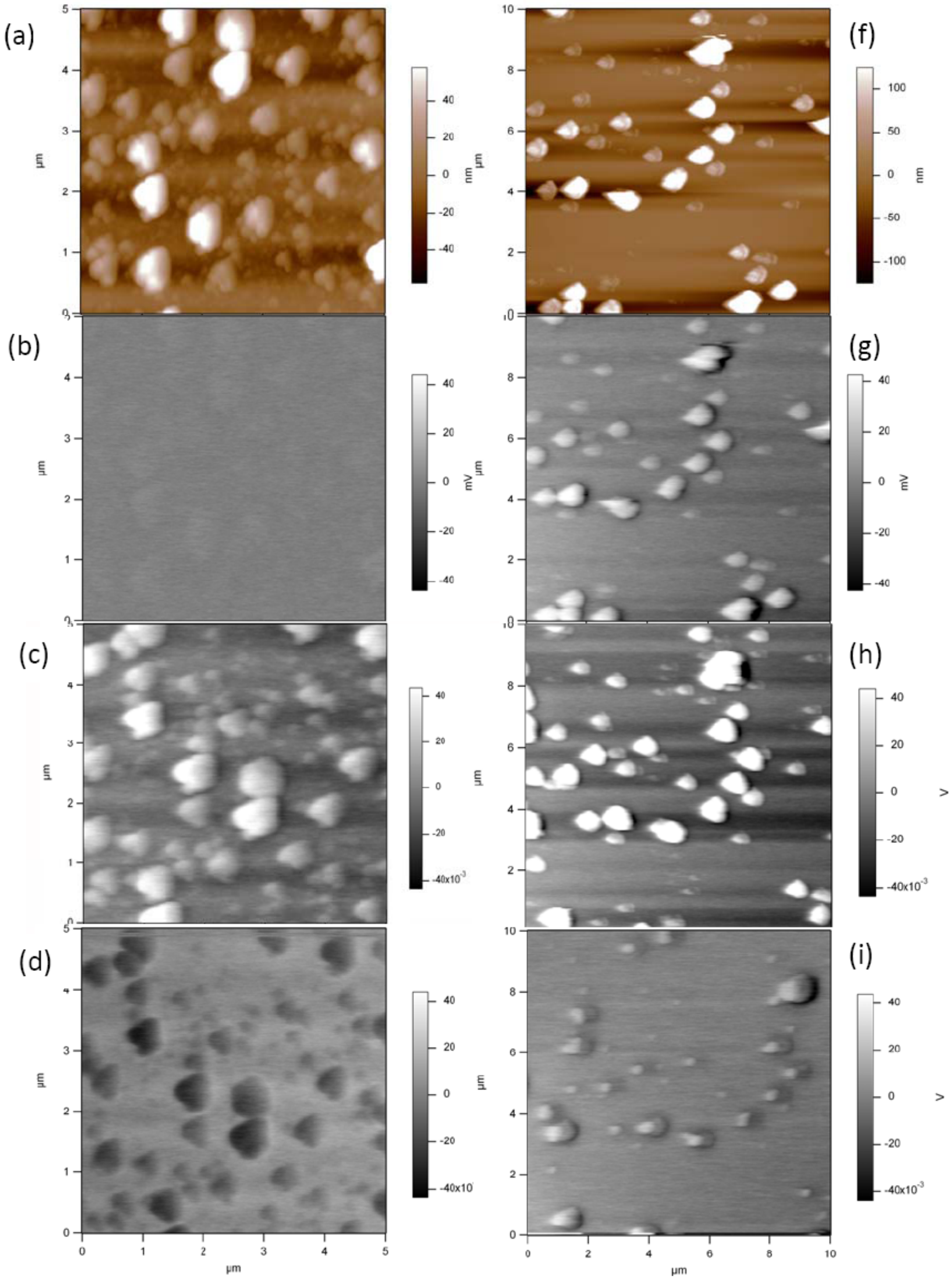

Figure 3.17 **Surface potential (SP) KPFM maps of PANI and core-shell nanoparticles, STO/PANI composites.** AFM topography (brown) and surface potential (SP) maps (gray). Scan area: 5 × 5 (PANI) and 10 × 10 μm (STO/PANI composites). These maps are from continual scanning in the same area with 10 min required for each scan. (a, f) Topological AFM image of PANI particles and STO/PANI composites with average height 80 and 130 nm, respectively. (b~d, g~i) SP images for the same area of PANI particles (a) and STO/PANI composites (f) with (b, g) 0 V DC bias, (c, h) +1 V DC bias and (d, i) -1 V DC bias. Delta height ΔZ=50 nm.

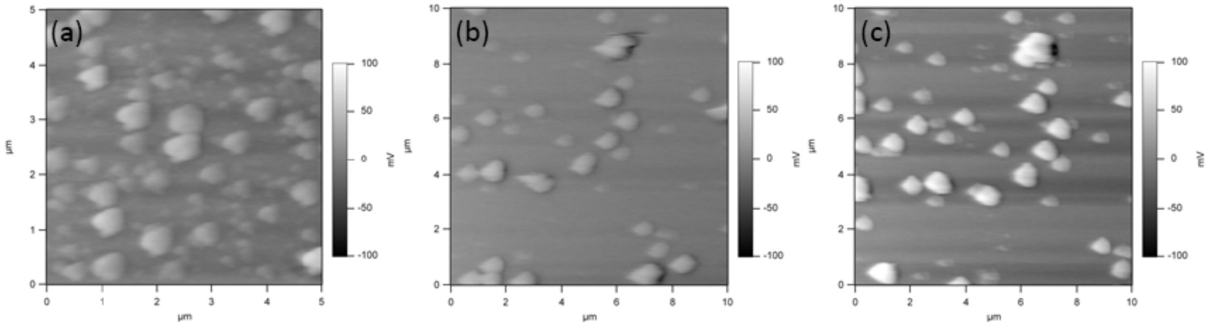

Figure 3.18 **Comparison of surface potential (SP) KPFM maps of PANI and composites.** PANI at 1 V (a) and core-shell nanoparticles, STO/PANI composites, at 0 V (b) and 1 V (c).

Chapter 4 Conclusion and Perspectives

Nanoscience represents an extraordinarily broad and important area, allowing the convergence of diverse fields to explore potential applications involving the manifestations of processes in nanometer scale. This dissertation reports significant findings on two recently very active nanoscience investigations: multiferroic nanomaterials and core-shell conducting polymer nanospheres. The systems investigated range from pure inorganic crystal, organic polymer to organic/inorganic hybrid. A new efficient methodology for preparation of multiferroic by spin-casting drops of precursor solution on substrates, followed by heating at 600 ºC, was discovered. The electric and magnetic orderings of BFO were also observed to be induced by the application of electric, magnetic, and optic stimulus.

An interfacial polymerization was used to prepare the core-shell nanospheres for controlled release with poly(3, 4-ethylenedioxythiophene), PEDOT, as shell. The room temperature ionic liquid (RTIL) as core is a promising material as carrier for chemical and biology applications. The significant volume change of PEDOT shell having RTIL core triggered by pH stimulation may lead to new applications, such as in biomedical technology**.** The size of nascent PEDOT nanospheres can be controlled in the range from 75 nm to 400 nm for various purposes. Cargos can be either loaded on core or shell of the nanosphere, depending on their hydrophilic or hydrophobic nature. In addition, an unusual synergistic electric property was observed for nanospheres with high-*k* STO crystals embedded in conductive polyaniline matrix**.**

Our new synthetic methodologies based on a single precursor solution have great advantages over the existing methods for the preparation of uniform multiferroic nanocrystal BFO thin film. Our findings of “electric-magnetic-optic” room temperature couplings in BFO are expected to have potentially a broad impact on extending the development of multiferroics in nanotechnology applications. For example, the efficient electric-field control of magnetism could yield entirely new devices, such as multiphase data storage, spintronics and high-frequency magnetic elements; the electric control is far more precise than direct magnetic control.[1, 2] Further effort on investigating the interaction among light, electric, and magnetic polarization will advance multiferroic to the level of a rich source for exploring fundamental EM phenomenon in nanoscale. A biocompatible soft template synthesis based on, “RTIL with conducting polymer”, was successful in providing core-shell nanospheres with good control release behavior. This nanosphere system can be extended to serve as a model for targeted control delivery with functionalized shell, e.g. using PEDOT copolymerization with comonomer having specific affinity for intended sites.[3]

The electric polarization behaviors in nanospheres with high-*k* nanocrystals embedded in conductive medium requires further systematic studies including size and dielectric constant of the particles, properties of the conductive matrix and the nature of the interface. This unique assembly can also serve as a model to study the basic physics of Lorentz field.[4, 5]

Bibliography

Chapter 1

1. Konstantatos, G.; Sargent, E. H., Nanostructured materials for photon detection. *Nat. Nanotechnol.* **2010**, 5 (6), 391-400.

2. Baek, S. H.; Jang, H. W.; Folkman, C. M.; Li, Y. L.; Winchester, B.; Zhang, J. X.; He, Q.; Chu, Y. H.; Nelson, C. T.; Rzchowski, M. S.; Pan, X. Q.; Ramesh, R.; Chen, L. Q.; Eom, C. B., Ferroelastic switching for nanoscale non-volatile magnetoelectric devices. *Nat. Mater.* **2010**, 9 (4), 309-314.

3. Ramesh, R.; Spaldin, N. A., Multiferroics: progress and prospects in thin films. *Nat. Mater.* **2007**, 6 (1), 21-29.

4. Hill, N. A., Why are there so few magnetic ferroelectrics? *J. Phy. Chem. B* **2000**, 104 (29), 6694-6709.

5. Spaldin, N. A.; Fiebig, M., Materials Science: The renaissance of magnetoelectric Multiferroics. *Science* **2005**, 309 (5733), 391-392.

6. Scott, J. F., Data storage: Multiferroic memories. *Nat. Mater.* **2007**, 6 (4), 256-257.

7. Mazumder, R.; Devi, P. S.; Bhattacharya, D.; Choudhury, P.; Sen, A.; Raja, M., Ferromagnetism in nanoscale $BiFeO_3$. *Appl. Phys. Lett.* **2007**, 91 (6), 062510.

8. Selbach, S. M.; Tybell, T.; Einarsrud, M.-A.; Grande, T., Size-dependent properties of multiferroic $BiFeO_3$ nanoparticles. *Chem. Mater.* **2007**.

9. Park, T. J.; Papaefthymiou, G. C.; Viescas, A. J.; Moodenbaugh, A. R.; Wong, S. S., Size-dependent magnetic properties of single-crystalline multiferroic $BiFeO_3$ nanoparticles. *Nano Lett.* **2007**, 7 (3), 766-772.

10. Shirakawa, H.; Louis, E. J.; MacDiarmid, A. G.; Chiang, C. K.; Heeger, A. J., Synthesis of electrically conducting organic polymers: halogen derivatives of polyacetylene, $(CH)_x$. *Chem. Commun.* **1977**, 578.

11. MacDiarmid, A. G., Synthetic metals: a novel role for organic polymers (Nobel Lecture). *Angew. Chem. Int. Ed.* **2001**, 40, 2581-2590.

12. van Schooneveld, Matti M.; Gloter, A.; Stephan, O.; Zagonel, L. F.; Koole, R.; Meijerink, A.; Mulder, Willem, J. M.; de Groot, Frank, M. F., Imaging and quantifying the morphology of an organic-inorganic nanoparticle at the sub-nanometre level. *Nat. Nanotechnol.* **2010**, 5 (7), 538-544.

13. Jang, J., Conducting polymer nanomaterials and their applications. *Adv. Polym Sci.* **2006**, 199, 189-259.

Chapter 2

1. Mostovoy, M., Multiferroics: A whirlwind of opportunities. *Nat. Mater.* **2010**, 9 (3), 188-190.

2. Choi, T.; Horibe, Y.; Yi, H. T.; Choi, Y. J.; Wu, W.; Cheong, S. W., Insulating interlocked ferroelectric and structural antiphase domain walls in multiferroic $YMnO_3$. *Nat. Mater.* **2010**, 9 (3), 253-258.

3. Martin, L. W.; Chu, Y. H.; Ramesh, R., Advances in the growth and characterization of magnetic, ferroelectric, and multiferroic oxide thin films. *Mat. Sci. and Eng. R* **2010**, 68 (4-6), 89-133.

4. Eerenstein, W.; Mathur, N. D.; Scott, J. F., Multiferroic and magnetoelectric materials. *Nature* **2006**, 442 (7104), 759-765.

5. Ramesh, R.; Spaldin, N. A., Multiferroics: progress and prospects in thin films. *Nat. Mater.* **2007**, 6 (1), 21-29.

6. Cheong, S.-W.; Mostovoy, M., Multiferroics: a magnetic twist for ferroelectricity. *Nat. Mater.* **2007**, 6 (1), 13-20.

7. Spaldin, N. A.; Fiebig, M., Materials science: the renaissance of magnetoelectric multiferroics. *Science* **2005**, 309 (5733), 391-392.

8. de Sousa, R.; Moore, J. E., Optical coupling to spin waves in the cycloidal multiferroic $BiFeO_3$. *Phys. Rev. B: Condens. Matter* **2008**, 77 (1), 012406.

9. Pyatakov, A. P.; Zhdanov, A. G.; Zvezdin, A. K. In second optical harmonic generation as a probe for magnetoelectric properties of multiferroic $BiFeO_3$, *Proc. SPIE:* **2007**; p 67292O.

10. Da, H. X.; Li, Z. Y., Optical magnetoelectric effect induced by a moving medium. *Phys. Rev. B: Condens. Matter* **2007**, 76 (1), 012409.

11. Sawada, K.; Nagaosa, N., Optical magnetoelectric effect in multiferroic materials: evidence for a lorentz force acting on a ray of light. *Phys. Rev. Lett.* **2005**, 95 (23), 237402.

12. Sharan, A.; Lettieri, J.; Jia, Y.; Tian, W.; Pan, X.; Schlom, D. G.; Gopalan, V., Bismuth manganite: a multiferroic with a large nonlinear optical response. *Phys. Rev. B* **2004**, 69 (21), 214109.

13. Wang, J.; Singh, M.; Tian, M.; Kumar, N.; Liu, B.; Shi, C.; Jain, J. K.; Samarth, N.; Mallouk, T. E.; Chan, M. H. W., Interplay between superconductivity and ferromagnetism in crystalline nanowires. *Nat. Phys.* **2010**, 6 (5), 389-394.

14. Takeuchi, I.; Famodu, O. O.; Read, J. C.; Aronova, M. A.; Chang, K. S.; Craciunescu, C.; Lofland, S. E.; Wuttig, M.; Wellstood, F. C.; Knauss, L.; Orozco, A., Identification of novel compositions of ferromagnetic shape-memory alloys using composition spreads. *Nat. Mater.* **2003**, 2 (3), 180-184.

15. Yamanouchi, M.; Chiba, D.; Matsukura, F.; Ohno, H., Current-induced domain-wall switching in a ferromagnetic semiconductor structure. *Nature* **2004**, 428 (6982), 539-542.

16. Das Sarma, S., Ferromagnetic semiconductors: a giant appears in spintronics. *Nat. Mater.* **2003**, 2 (5), 292-294.

17. Scott, J. F., Data storage: multiferroic memories. *Nat. Mater.* **2007**, 6 (4), 256-257.

18. Hatt, A. J.; Spaldin, N. A., Trilayer superlattices: a route to magnetoelectric multiferroics? *Appl. Phys. Lett.* **2007**, 90 (24), 242916.

19. Hur, N.; Park, S.; Sharma, P. A.; Ahn, J. S.; Guha, S.; Cheong, S. W., Electric polarization reversal and memory in a multiferroic material induced by magnetic fields. *Nature* **2004**, 429 (6990), 392-395.

20. Sousa, R. d.; Moore, J. E., Optical coupling to spin waves in the cycloidal multiferroic $BiFeO_3$. *Phys. Rev. B: Condens. Matter* **2008**, 77 (1), 012406.

21. Tilley, D. R.; Scott, J. F., Frequency dependence of magnetoelectric phenomena in $BaMnF_4$. *Phys. Rev. B* **1982**, 25 (5), 3251.

22. Maugin, G. A., Dynamic magnetoelectric couplings in ferroelectric ferromagnets. *Phys. Rev. B* **1981**, 23 (9), 4608.

23. Rikken, G. L. J. A.; Strohm, C.; Wyder, P., Observation of magnetoelectric directional anisotropy. *Phys. Rev. Lett.* **2002**, 89 (13), 133005.

24. Kida, N.; Yamada, T.; Konoto, M.; Okimoto, Y.; Arima, T.; Koike, K.; Akoh, H.; Tokura, Y., Optical magnetoelectric effect in a submicron patterned magnet. *Phys. Rev. Lett.* **2005**, 94 (7), 077205.

25. Kida, N.; Kaneko, Y.; He, J. P.; Matsubara, M.; Sato, H.; Arima, T.; Akoh, H.; Tokura, Y., Enhanced optical magnetoelectric effect in a patterned polar ferrimagnet. *Phys. Rev. Lett.* **2006**, 96 (16), 167202.

26. Jung, J. H.; Matsubara, M.; Arima, T.; He, J. P.; Kaneko, Y.; Tokura, Y., Optical Magnetoelectric effect in the polar $GaFeO_3$ ferrimagnet. *Phys. Rev. Lett.* **2004**, 93 (3), 037403.

27. Matteo, S. D.; Joly, Y., Parity and time-reversal breaking effects detected by resonant x-ray scattering. *Phys. Rev. B: Condens. Matter* **2006**, 74 (1), 014403.

28. Sawada, K.; Nagaosa, N., Gigantic enhancement of magnetochiral effect in photonic crystals. *Appl. Phys. Lett.* **2005**, 87 (4), 042503.

29. Choi, T.; Lee, S.; Choi, Y. J.; Kiryukhin, V.; Cheong, S.-W., Switchable ferroelectric diode and photovoltaic effect in $BiFeO_3$. *Science* **2009**, 324 (5923), 63-66.

30. Wei, J.; Xue, D.; Xu, Y., Photoabsorption characterization and magnetic property of multiferroic $BiFeO_3$ nanotubes synthesized by a facile sol-gel template process. *Scr. Mater.* **2008**, 58 (1), 45-48.

31. Choi, W. S.; Moon, S. J.; Seo, S. S. A.; Lee, D.; Lee, J. H.; Murugavel, P.; Noh, T. W.; Lee, Y. S., Optical spectroscopic investigation on the coupling of electronic and magnetic structure in multiferroic hexagonal $RMnO_3$ (R = Gd, Tb, Dy, and Ho) thin films. *Phys. Rev. B: Condens. Matter* **2008**, 78 (5), 054440.

32. Takahashi, K.; Tonouchi, M., Observation of photoassisted polarization switching in $BiFeO_3$ thin films probed by terahertz radiation. *Appl. Phys. Lett.* **2007**, 90 (5), 052908.

33. Popova, M. N.; Chukalina, E. P.; Stanislavchuk, T. N.; Malkin, B. Z.; Zakirov, A. R.; Antic-Fidancev, E.; Popova, E. A.; Bezmaternykh, L. N.; Temerov, V. L., Optical spectra, crystal-field parameters, and magnetic susceptibility of multiferroic $NdFe_3(BO_3)_4$. *Phys. Rev. B: Condens. Matter* **2007**, 75 (22), 224435.

34. Hill, N. A., Why are there so few magnetic ferroelectrics? *J. Phy. Chem. B* **2000**, 104 (29), 6694-6709.

35. Prokhnenko, O.; Feyerherm, R.; Dudzik, E.; Landsgesell, S.; Aliouane, N.; Chapon, L. C.; Argyriou, D. N., Enhanced ferroelectric polarization by induced Dy spin order in multiferroic $DyMnO_3$. *Phys. Rev. Lett.* **2007**, 98 (5), 057206.

36. Chaudhury, R. P.; Yen, F.; dela Cruz, C. R.; Lorenz, B.; Wang, Y. Q.; Sun, Y. Y.; Chu, C. W., Pressure-temperature phase diagram of multiferroic $Ni_3V_2O_8$. *Phys. Rev. B: Condens. Matter* **2007**, 75 (1), 012407.

37. Argyriou, D. N.; Aliouane, N.; Strempfer, J.; Zegkinoglou, I.; Bohnenbuck, B.; Habicht, K.; Zimmermann, M. v., Melting of incommensurate-ferroelectric phase with magnetic field in multiferroic $TbMnO_3$. *Phys. Rev. B: Condens. Matter* **2007**, 75 (2), 020101.

38. Singh, A. K.; Kaushik, S. D.; Kumar, B.; Mishra, P. K.; Venimadhav, A.; Siruguri, V.; Patnaik, S., Substantial magnetoelectric coupling near room temperature in $Bi_2Fe_4O_9$. *Appl. Phys. Lett.* **2008**, 92 (13), 132910-3.

39. Chu, Y. H.; Martin, L. W.; Zhan, Q.; Yang, P. L.; Cruz, M. P.; Lee, K.; Barry, M.; Yang, S. Y.; Ramesh, R., Epitaxial multiferroic $BiFeO_3$ thin films: progress and future directions. *Ferroelectrics* **2007**, 354 (1), 167-177.

40. Zhao, T.; Scholl, A.; Zavaliche, F.; Lee, K.; Barry, M.; Doran, A.; Cruz, M. P.; Chu, Y. H.; Ederer, C.; Spaldin, N. A.; Das, R. R.; Kim, D. M.; Baek, S. H.; Eom, C. B.; Ramesh, R., Electrical control of antiferromagnetic domains in multiferroic BiFeO3 films at room temperature. *Nat. Mater.* **2006**, 5 (10), 823-829.

41. Mazumder, R.; Devi, P. S.; Bhattacharya, D.; Choudhury, P.; Sen, A.; Raja, M., Ferromagnetism in nanoscale $BiFeO_3$. *Appl. Phys. Lett.* **2007**, 91 (6), 062510.

42. Ederer, C.; Spaldin, N. A., Weak ferromagnetism and magnetoelectric coupling in bismuth ferrite. *Phys. Rev. B* **2005**, 71 (6), 060401.

43. Wang, Y. P.; Zhou, L.; Zhang, M. F.; Chen, X. Y.; Liu, J. M.; Liu, Z. G., Room-temperature saturated ferroelectric polarization in $BiFeO_3$ ceramics synthesized by rapid liquid phase sintering. *Appl. Phys. Lett.* **2004**, 84 (10), 1731-1733.

44. Cheng, J.-R.; Li, N.; Cross, L. E., Structural and dielectric properties of Ga-modified $BiFeO_3$--$PbTiO_3$ crystalline solutions. *J. Appl. Phys.* **2003**, 94 (8), 5153-5157.

45. Kumar, M.; Yadav, K. L.; Varma, G. D., Large magnetization and weak polarization in sol-gel derived $BiFeO_3$ ceramics. *Mater. Lett.* **2008**, 62 (8-9), 1159-1161.

46. Selbach, S. M.; Tybell, T.; Einarsrud, M.-A.; Grande, T., Size-dependent properties of multiferroic $BiFeO_3$ nanoparticles. *Chem. Mater.* **2007**.

47. Schlom, D. G.; Haeni, J. H.; Lettieri, J.; Theis, C. D.; Tian, W.; Jiang, J. C.; Pan, X. Q., Oxide nano-engineering using MBE. *Mater. Sci. Eng. B* **2001**, 87 (3), 282-291.

48. Wang, J.; Neaton, J. B.; Zheng, H.; Nagarajan, V.; Ogale, S. B.; Liu, B.; Viehland, D.; Vaithyanathan, V.; Schlom, D. G.; Waghmare, U. V.; Spaldin, N. A.; Rabe, K. M.; Wuttig, M.; Ramesh, R., Epitaxial $BiFeO_3$ multiferroic thin film heterostructures. *Science* **2003**, 299 (5613), 1719-1722.

49. Chu, Y.-H.; Zhan, Q.; Martin, L. W.; Cruz, M. P.; Yang, P.-L.; Pabst, G. W.; Zavaliche, F.; Yang, S. Y.; Zhang, J. X.; Chen, L. Q.; Schlom, D. G.; Lin, I. N.; Wu, T. B.; Ramesh, R., Nanoscale domain control in multiferroic $BiFeO_3$ thin films. *Adv. Mater.* **2006**, 18 (17), 2307-2311.

50. Park, T. J.; Papaefthymiou, G. C.; Viescas, A. J.; Moodenbaugh, A. R.; Wong, S. S., Size-dependent magnetic properties of single-crystalline multiferroic $BiFeO_3$ nanoparticles. *Nano Lett.* **2007**, 7 (3), 766-772.

51. Singh, V. R.; Dixit, A.; Garg, A.; Agrawal, D. C., Effect of heat treatment on the structure and properties of chemical solution processed multiferroic $BiFeO_3$ thin films. *Appl. Phys. A: Mater. Sci. Process.* **2008**, 90 (1), 197-202.

52. Lee, S. U.; Kim, S. S.; Park, M. H.; Kim, J. W.; Jo, H. K.; Kim, W.-J., Effects of co-substitution on the electrical properties of $BiFeO_3$ thin films prepared by chemical solution deposition. *Appl. Surf. Sci.* **2007**, 254 (5), 1493-1497.

53. Shetty, S.; Palkar, V. R.; Pinto, R., Size effect study in magnetoelectric $BiFeO_3$ system. *Pramana* **2002**, 58, 1027-1030.

54. Mazumder, R.; Ghosh, S.; Mondal, P.; Bhattacharya, D.; Dasgupta, S.; Das, N.; Sen, A.; Tyagi, A. K.; Sivakumar, M.; Takami, T.; Ikuta, H., Particle size dependence of magnetization and phase transition near TN in multiferroic $BiFeO_3$. *J. Appl. Phys.* **2006**, 100 (3), 033908.

55. Zhong, Q.; Inniss, D.; Kjoller, K.; Elings, V. B., Fractured polymer/silica fiber surface studied by tapping mode atomic force microscopy. *Surf. Sci. Lett.* **1993**, 290 (1-2), L688-L692.

56. Binnig, G.; Quate, C. F.; Gerber, C., Atomic force microscope. *Phys. Rev. Lett.* **1986**, 56 (9), 930.

57. Ohnesorge, F.; Binnig, G., True atomic resolution by atomic force microscopy through repulsive and attractive forces. *Science* **1993**, 260 (5113), 1451-1456.

58. Martin, Y.; Wickramasinghe, H. K., Magnetic imaging by ``force microscopy" with 1000Å resolution. *Appl. Phys. Lett.* **1987**, 50 (20), 1455-1457.

59. Martin, Y.; Abraham, D. W.; Wickramasinghe, H. K., High-resolution capacitance measurement and potentiometry by force microscopy. *Appl. Phys. Lett.* **1988**, 52 (13), 1103-1105.

60. Jacobs, H. O.; Knapp, H. F.; Müller, S.; Stemmer, A., Surface potential mapping: a qualitative material contrast in SPM. *Ultramicroscopy* **1997**, 69 (1), 39-49.

61. Son, J. Y.; Kyhm, K.; Cho, J. H., Surface charge retention and enhanced polarization effect on ferroelectric thin films. *Appl. Phys. Lett.* **2006**, 89 (9), 092907.

62. Kim, J.; Kim, Y.; No, K.; Simon, B.; Hong, S.; Nam, Y.-W.; Kim, S.-H., Surface potential relaxation of ferroelectric domain investigated by Kelvin probe microscopy. *Integ. Ferroelectr.* **2006**, 85 (1), 25-30.

63. Avila, A.; Bhushan, B., Electrical measurement techniques in atomic force microscopy. *Crit. Rev. Solid State* **2010**, 35 (1), 38 - 51.

64. Son, J. Y.; Kim, B. G.; Kim, C. H.; Cho, J. H., Writing polarization bits on the multiferroic $BiMnO_3$ thin film using Kelvin probe force microscope. *Appl. Phys. Lett.* **2004**, 84 (24), 4971-4973.

Chapter 3

1. George, P.□M.; LaVan, D. A.; Burdick, J. A.; Chen, C.-Y.; Liang, E.; Langer, R., Electrically controlled drug delivery from biotin-doped conductive polypyrrole. *Adv. Mater.* **2006**, 18 (5), 577-581.

2. Geetha, S.; Rao, C. R. K.; Vijayan, M.; Trivedi, D. C., Biosensing and drug delivery by polypyrrole. *Anal. Chim. Acta* **2006**, 568 (1-2), 119-125.

3. Langer, R., Biomaterials in drug delivery and tissue engineering: one laboratory's experience. *Acc. Chem. Res.* **2000**, 33 (2), 94-101.

4. Pillai, O.; Panchagnula, R., Polymers in drug delivery. *Curr. Opin. Chem. Biol.* **2001**, 5 (4), 447-451.

5. Allen, T. M.; Cullis, P. R., Drug delivery systems: entering the mainstrmeam. *Science* **2004**, 303 (5665), 1818-1822.

6. Abidian, M. R.; Kim, D.-H.; Martin, D. C., Conducting-polymer nanotubes for controlled drug release. *Adv. Mater.* **2006**, 18 (4), 405-409.

7. Wei, Z.; Wan, M., Hollow microspheres of polyaniline synthesized with an aniline emulsion template. *Adv. Mater.* **2002**, 14 (18), 1314-1317.

8. Jang, J.; Chang, M.; Yoon, H., Chemical sensors based on highly conductive poly(3,4-ethylenedioxythiophene) nanorods. *Adv. Mater.* **2005**, 17 (13), 1616-1620.

9. Huang, J.; Virji, S.; Weiller, B. H.; Kaner, R. B., Nanostructured polyaniline sensors. *Chem. Eur. J.* **2004**, 10 (6), 1314-1319.

10. Smela, E., Conjugated polymer actuators for biomedical applications. *Adv. Mater.* **2003**, 15 (6), 481-494.

11. Smela, E.; Inganas, O.; Lundstrom, I., Controlled folding of micrometer-size structures. *Science* **1995**, 268 (5218), 1735-1738.

12. Jager, E. W. H.; Smela, E.; Inganas, O., Microfabricating conjugated polymer actuators. *Science* **2000**, 290 (5496), 1540-1545.

13. George, P. M.; LaVan, D. A.; Burdick, J. A.; Chen, C.-Y.; Liang, E.; Langer, R., Electrically controlled drug delivery from biotin-doped conductive polypyrrole. *Adv. Mater.* **2006**, 18 (5), 577-581.

14. Abidian, M. R.; Martin, D. C., Multifunctional nanobiomaterials for neural interfaces. *Adv. Funct. Mater.* **2009**, 19 (4), 573-585.

15. Svirskis, D.; Travas-Sejdic, J.; Rodgers, A.; Garg, S., Electrochemically controlled drug delivery based on intrinsically conducting polymers. *J. Controlled Release* **2010**, In Press, Corrected Proof.

16. Jang, J.; Bae, J.; Park, E., Selective fabrication of poly(3,4-ethylenedioxythiophene) nanocapsules and mesocellular foams using surfactant-mediated interfacial polymerization. *Adv. Mater.* **2006**, 18 (3), 354-358.

17. Sui, J.; Zhang, L.; Travas-Sejdic, J.; Kilmartin, P. A., Synthesis of poly(3,4-ethylenedioxythiophene) hollow spheres in CTAB/DBS - mixed surfactant solutions. *Macromol. Symp.* **2010**, 290 (1), 107-114.

18. Zhang, L.; Liu, P., Polyaniline micro/nano capsules via facile interfacial polymerization approach. *Soft Materials* **2010**, 8 (1), 29 - 38.

19. Peng, Z.; You, H.; Wu, J.; Yang, H., Electrochemical synthesis and catalytic property of sub-10 nm platinum cubic nanoboxes. *Nano Lett.* **2010**, 10 (4), 1492-1496.

20. Antony, M. J.; Jayakannan, M., Molecular template approach for evolution of conducting polymer nanostructures: tracing the role of morphology on conductivity and solid state ordering. *J. Phys. Chem. B* **2010**, 114 (3), 1314-1324.

21. Wadhwa, R.; Lagenaur, C. F.; Cui, X. T., Electrochemically controlled release of dexamethasone from conducting polymer polypyrrole coated electrode. *J. Controlled Release* **2006**, 110 (3), 531-541.

22. Richardson-Burns, S. M.; Hendricks, J. L.; Foster, B.; Povlich, L. K.; Kim, D.-H.; Martin, D. C., Polymerization of the conducting polymer poly(3,4-ethylenedioxythiophene) (PEDOT) around living neural cells. *Biomaterials* **2007**, 28 (8), 1539-1552.

23. Sun, Y.; Xia, Y., Shape-controlled synthesis of gold and silver nanoparticles. *Science* **2002**, 298 (5601), 2176-2179.

24. Goldberger, J.; He, R.; Zhang, Y.; Lee, S.; Yan, H.; Choi, H.-J.; Yang, P., Single-crystal gallium nitride nanotubes. *Nature* **2003**, 422 (6932), 599-602.

25. Sun, Y.; Mayers, B.; Xia, Y., Metal nanostructures with hollow interiors. *Adv. Mater.* **2003**, 15 (7-8), 641-646.

26. Yang, Z.; Niu, Z.; Lu, Y.; Hu, Z.; Han, C. C., Templated synthesis of inorganic hollow spheres with a tunable cavity size onto core-shell gel particles. *Angew. Chem. Int. Ed.* **2003**, 42 (17), 1943-1945.

27. Ding, S.-J.; Zhang, C.-L.; Yang, M.; Qu, X.-Z.; Lu, Y.-F.; Yang, Z.-Z., Template synthesis of composite hollow spheres using sulfonated polystyrene hollow spheres. *Polymer* **2006**, 47 (25), 8360-8366.

28. Xie, L.; Zheng, J.; Liu, Y.; Li, Y.; Li, X., Synthesis of Li_2NH hollow nanospheres with superior hydrogen storage kinetics by plasma metal reaction. *Chem. Mater.* **2008**, 20 (1), 282-286.

29. Kondo, Y.; Yoshikawa, H.; Awaga, K.; Murayama, M.; Mori, T.; Sunada, K.; Bandow, S.; Iijima, S., Preparation, photocatalytic activities, and dye-sensitized solar-cell performance of submicron-scale TiO_2 hollow spheres. *Langmuir* **2008**, 24 (2), 547-550.

30. Yin, Y.; Rioux, R. M.; Erdonmez, C. K.; Hughes, S.; Somorjai, G. A.; Alivisatos, A. P., Formation of hollow nanocrystals through the nanoscale kirkendall effect. *Science* **2004**, 304 (5671), 711-714.

31. Li, J.; Zeng, H. C., Hollowing Sn-doped TiO_2 nanospheres via ostwald ripening. *J. Am. Chem. Soc.* **2007**, 129 (51), 15839-15847.

32. Duvail, J. L.; Retho, P.; Garreau, S.; Louarn, G.; Godon, C.; Demoustier-Champagne, S., Transport and vibrational properties of poly(3,4-ethylenedioxythiophene) nanofibers. *Synth. Met.* **2002**, 131 (1-3), 123-128.

33. Kros, A.; Nolte, R. J. M.; Sommerdijk, N. A. J. M., Conducting polymers with confined dimensions: track-etch membranes for amperometric biosensor applications. *Adv. Mater.* **2002**, 14 (23), 1779-1782.

34. Joo, J.; Park, K. T.; Kim, B. H.; Kim, M. S.; Lee, S. Y.; Jeong, C. K.; Lee, J. K.; Park, D. H.; Yi, W. K.; Lee, S. H.; Ryu, K. S., Conducting polymer nanotube and nanowire synthesized by using nanoporous template: synthesis, characteristics, and applications. *Synth. Met.* **2003**, 135-136, 7-9.

35. Han, M. G.; Foulger, S. H., 1-Dimensional structures of poly(3,4-ethylenedioxythiophene) (PEDOT): a chemical route to tubes, rods, thimbles, and belts. *Chem. Commun.* **2005**, (24), 3092-3094.

36. Kim, B. H.; Park, D. H.; Joo, J.; Yu, S. G.; Lee, S. H., Synthesis, characteristics, and field emission of doped and de-doped polypyrrole, polyaniline, poly(3,4-ethylenedioxythiophene) nanotubes and nanowires. *Synth. Met.* **2005**, 150 (3), 279-284.

37. Hulvat, J. F.; Stupp, S. I., Anisotropic properties of conducting polymers prepared by liquid crystalt. *Adv. Mater.* **2004**, 16 (7), 589-592.

38. Han, M. G.; Foulger, S. H., Facile synthesis of poly(3,4-ethylenedioxythiophene) nanofibers from an aqueous surfactant solution. *Small* **2006**, 2 (10), 1164-1169.

39. Han, M. G.; Foulger, S. H., Preparation of poly(3,4-ethylenedioxythiophene) (PEDOT) coated silica core-shell particles and PEDOT hollow particles. *Chem. Commun.* **2004**, (19), 2154-2155.

40. Han, M. G.; Foulger, S. H., Crystalline colloidal arrays composed of poly(3,4-ethylenedioxythiophene)-coated polystyrene particles with a stop band in the visible regime. *Adv. Mater.* **2004**, 16 (3), 231-234.

41. Muller, K.; Klapper, M.; Mullen, K., Synthesis of conjugated polymer nanoparticles in non-aqueous emulsions. *Macromol. Rapid Commun.* **2006**, 27 (8), 586-593.

42. Dupont, J.; Fonseca, G. S.; Umpierre, A. P.; Fichtner, P. F. P.; Teixeira, S. R., Transition-metal nanoparticles in imidazolium ionic liquids: recycable catalysts for biphasic hydrogenation reactions. *J. Am. Chem. Soc.* **2002**, 124 (16), 4228-4229.

43. Park, S.; Kazlauskas, R. J., Biocatalysis in ionic liquids - advantages beyond green technology. *Curr. Opin. Biotechnol.* **2003**, 14 (4), 432-437.

44. van Rantwijk, F.; Madeira Lau, R.; Sheldon, R. A., Biocatalytic transformations in ionic liquids. *Trends Biotechnol.* **2003**, 21 (3), 131-138.

45. Liu, Y.; Wang, M.; Li, J.; Li, Z.; He, P.; Liu, H.; Li, J., Highly active horseradish peroxidase immobilized in 1-butyl-3-methylimidazolium tetrafluoroborate room-temperature ionic liquid based sol-gel host materials. *Chem. Comm.* **2005**, (13), 1778-1780.

46. Pozo-Gonzalo, C.; Mecerreyes, D.; Pomposo, J. A.; Salsamendi, M.; Marcilla, R.; Grande, H.; Vergaz, R.; Barrios, D.; Sanchez-Pena, J. M., All-plastic electrochromic devices based on PEDOT as switchable optical attenuator in the near IR. *Sol. Energy Mater. Sol. Cells* **2008**, 92, 101-106.

47. Su, K.; Chu, I.-W.; Yang, N.-L., One-pot synthesis of core-shell nanocomposites spheres of strontium titanante embedded in polyaniline and their electric polarization properties. *In Preparation.*

Chapter 4

1. Chu, Y.-H.; Martin, L. W.; Holcomb, M. B.; Gajek, M.; Han, S.-J.; He, Q.; Balke, N.; Yang, C.-H.; Lee, D.; Hu, W.; Zhan, Q.; Yang, P.-L.; Fraile-rodriguez, A.; Scholl, A.; Wang, S. X.; Ramesh, R., Electric-field control of local ferromagnetism using a magnetoelectric multiferroic. *Nat. Mater.* **2008**, 7 (8), 678-678.

2. Ramesh, R., Ferroelectrics: a new spin on spintronics. *Nat. Mater.* 2010, 9 (5), 380-381.

3. Lee, Y.-H.; Chang, C.-J.; Kao, C.-J.; Dai, C.-A., In-situ template synthesis of a polymer/semiconductor nanohybrid using amphiphilic conducting block copolymers. *Langmuir* **2010**, 26 (6), 4196-4206.

4. Li, Y.; Shimizu, H., Toward a stretchable, elastic, and electrically conductive nanocomposite: morphology and properties of poly[styrene-b-(ethylene-co-butylene)-b-styrene]/multiwalled carbon nanotube composites fabricated by high-shear processing. *Macromolecules* **2009**, 42 (7), 2587-2593.

5. Srivastava, Y. N.; Widom, A.; Larsen, L., A primer for electro-weak induced low energy nuclear reactions. In low-energy nuclear reactions and new energy technologies. *Sourcebook Volume 2, American Chemical Society:* **2009**; Vol. 1029, pp 253-270.